Titre: Title:	MRI-Based Communication with Untethered Intelligent Medical Microrobots
Auteur: Author:	Azadeh Sharafi Tafreshi Moghaddam
Date:	2015
Type:	Mémoire ou thèse / Dissertation or Thesis
Référence: Citation:	Sharafi Tafreshi Moghaddam, A. (2015). MRI-Based Communication with Untethered Intelligent Medical Microrobots [Ph.D. thesis, École Polytechnique de Montréal]. PolyPublie. https://publications.polymtl.ca/1930/

UNIVERSITÉ DE MONTRÉAL

MRI-BASED COMMUNICATION WITH UNTETHERED INTELLIGENT MEDICAL MICROROBOTS

AZADEH SHARAFI TAFRESHI MOGHADDAM

INSTITUT DE GÉNIE BIOMÉDICAL

ÉCOLE POLYTECHNIQUE DE MONTRÉAL

THÈSE PRÉSENTÉE EN VUE DE L'OBTENTION

DU DIPLÔME DE PHILOSOPHIAE DOCTOR

(GÉNIE BIOMÉDICAL)

NOVEMBRE 2015

UNIVERSITÉ DE MONTRÉAL

ÉCOLE POLYTECHNIQUE DE MONTRÉAL

Cette thèse intitulée :

MRI-BASED COMMUNICATION WITH UNTETHERED INTELLIGENT MEDICAL MICROROBOTS

présentée par : SHARAFI TAFRESHI MOGHADDAM Azadeh

en vue de l'obtention du diplôme de : Philosophiae Doctor

a été dûment acceptée par le jury d'examen constitué de :

Mme CHERIET Farida, Ph. D., présidente

M. MARTEL Sylvain, Ph. D., membre et directeur de recherche

M. DESCHÊNES Sylvain, Ph. D., membre

M. FERREIRA Antoine, Ph. D., membre externe

DEDICATION

To my parents

ACKNOWLEDGEMENTS

This thesis would not have been possible without the help, support and patience of my supervisor, Dr. Sylvain Martel whose advice, encouragement and unsurpassed knowledge contributes to my graduate work and experience. I would have been lost without him

I would like to thank my fellow labmates Samira Taherkhani and Charles Trembley for the stimulating discussions and for their encouragement and empathy. I would like to thank Dr. Alexandre Bigot who was always willing to help and share his findings and experiences. Special thanks to Dr. Nina Olamaei, my best friend and colleague, for her friendship, her insightful comments and her support. I am also grateful to other members of the Nanorobotics laboratory who each in one way or another helped me to complete this journey.

I would like to thank my twin sister, Dr. Zohreh Sharafi, who has been my biggest supporter in this journey. It was her constant help, encouragement and love that finally made it possible for me to see this project through to the end.

Last, but certainly not least, I must acknowledge with tremendous and deep gratitude my late mother, Dr. Mahnaz Jafaripour, greatly missed, and my father, Dr. Aliakbar Sharafi for always believing in me. Without them, I would not have made it this far.

RESUME

Les champs magnétiques présent dans un système clinique d'Imagerie par Résonance Magnétique (IRM) peuvent être exploités non seulement, afin d'induire une force de déplacement sur des microrobots magnétiques tout en permettant l'asservissement de leur position - une technique connue sous le nom de Navigation par Résonance Magnétique (NRM), mais aussi pour mettre en œuvre un procédé de communication. Pour des microrobots autonomes équipés de senseurs ayant un certain niveau d'intelligence et opérant à l'intérieur du corps humain, la puissance de transmission nécessaire pour communiquer des informations à un ordinateur externe par des méthodes présentement connues est insuffisante. Dans ce travail, une technique est décrite où une telle perte de puissance d'émission en raison de la mise à l'échelle de ces microrobots peut être compensée par le scanner IRM agissant aussi comme un récepteur très sensible. La technique de communication prend la forme d'une modification de la fréquence du courant électrique circulant le long d'une bobine miniature incorporé dans un microrobot. La fréquence du courant électrique peut être réglée à partir d'une entrée de seuil prédéterminée du senseur mis en place sur le microrobot. La fréquence devient alors corrélée à l'information de l'état du senseur recueilli par le microrobot et elle est déterminée en utilisant l'IRM. La méthode proposée est indépendante de la position et l'orientation du microrobot et peut être étendue à un grand nombre de microrobots pour surveiller et cartographier les conditions physiologiques spécifiques dans une région plus vaste à n'importe quelle profondeur à l'intérieur du corps.

ABSTRACT

The magnetic environment provided by a clinical Magnetic Resonance Imaging (MRI) scanner can be exploited to not only induce a displacement force on magnetic microrobots while allowing MR-tracking for serving control purpose or positional assessment - a technique known as Magnetic Resonance Navigation (MRN), but also for implementing a method of communication with intelligent microrobots. For untethered sensory microrobots having some level of intelligence and operating inside the body, the transmission power necessary to communicate information to an external computer via known methods is insufficient. In this work, a technique is described where such loss of transmission power due to the scaling of these microrobots can be compensated by the same MRI scanner acting as a more sensitive receiver. A communication scheme is implemented in the form of a frequency alteration in the electrical current circulating along a miniature coil embedded in a microrobot. The frequency of the electrical current could be regulated from a predetermined sensory threshold input implemented on the microrobot. Such a frequency provides information on the level of sensory information gathered by the microrobot, and it is determined using MR imaging. The proposed method is independent of the microrobot's position and orientation and can be extended to a larger number of microrobots for monitoring and mapping specific physiological conditions inside a larger region at any depths within the body.

TABLE OF CONTENTS

LIST OF TABLES

LIST OF FIGURES

LIST OF SYMBOLS AND ABBREVIATIONS

2D	Two Dimensional
3D	Three Dimensional
BW	Bandwidth
AlN	Aluminum Nitride
CAD	Computer-Aided Design
CMOS	Complementary Metal Oxide Semiconductor
EPI	Echo planar imaging
FDA	U.S. Food and Drug Administration
FOV	Field Of View
FSK	Frequency-Shift Keying
FT	Fourier Transform
GRAPPA	Generalized Autocalibrating Partially Parallel Acquisitions
GRE	Gradient Recalled Echo
HWHM	Half Width at Half Maximum
ISFET	Ion-Sensitive Field-Effect Transistor
PZT	Lead Zirconate Titanate
MICS	Medical Implant Communication Service
MR	Magnetic Resonance
MRI	Magnetic Resonance Imaging
MSK	Minimum-Shift Keying
MTB	Magnetotactic Bacteria
PCB	Printed Circuit Board

PILS	Parallel Imaging with Localized Sensitivities
PNS	Peripheral Nerve Stimulation
PSD	Phase-Sensitive Detection
rBW	Receiver Bandwidth
RF	Radio Frequency
ROI	Region Of Interest
SE	Spin Echo
SENSE	Sensitivity Encoding
SMASH	Simultaneous Acquisition of Spatial Harmonics
SNR	Signal to Noise Ratio
TE	Echo Time
TR	Repetition Time
ZnO	Zinc Oxide

CHAPTER 1 INTRODUCTION

1.1 Research context and problem statement

Recent developments in the design and fabrication of integrated circuits allow us to build advanced microrobots for different medical applications such as telemetry and minimally invasive surgery [1, 2]. Different tasks that cannot be performed using traditional technologies, such as targeted drug delivery and the clearing of clogged blood vessels, may be accomplished by navigating microrobots through complex structures (e.g., blood vessels) [3, 4].

However, the great majority of the studies on microrobots for interventions in the human body focus on the actuation and control of the microrobots [5-14]. Potential applications of the microrobots can be considerably expanded by embedding an integrated circuit capable of sensing, processing, and communicating environmental variables (e.g., pH, O_2). There are three major requirements for implementing such a microrobot as shown in Figure 1-1.

1. A power supply to provide energy for the functioning of all the components of the microrobot. The miniaturization of microrobots prevents the implementation of an embedded power source; hence, the electrical power must be provided from an external source using wireless approaches such as radio-frequency (RF), induction [15, 16], or photovoltaic cells [17].
2. An integrated circuit to measure the environmental variable, process the data and provide an input to the communication circuit.
3. A communication method to transfer data from the microrobot inside the human body to the external control system.

In this dissertation, we focus on providing communication method that will fulfill this last requirement. In our proposed microrobot, we use a photovoltaic cell as a power supply as presented in [18] while an ion-sensitive field-effect transistor (ISFET) could be exploited as a sensor and a miniature coil acts as a transmitter.

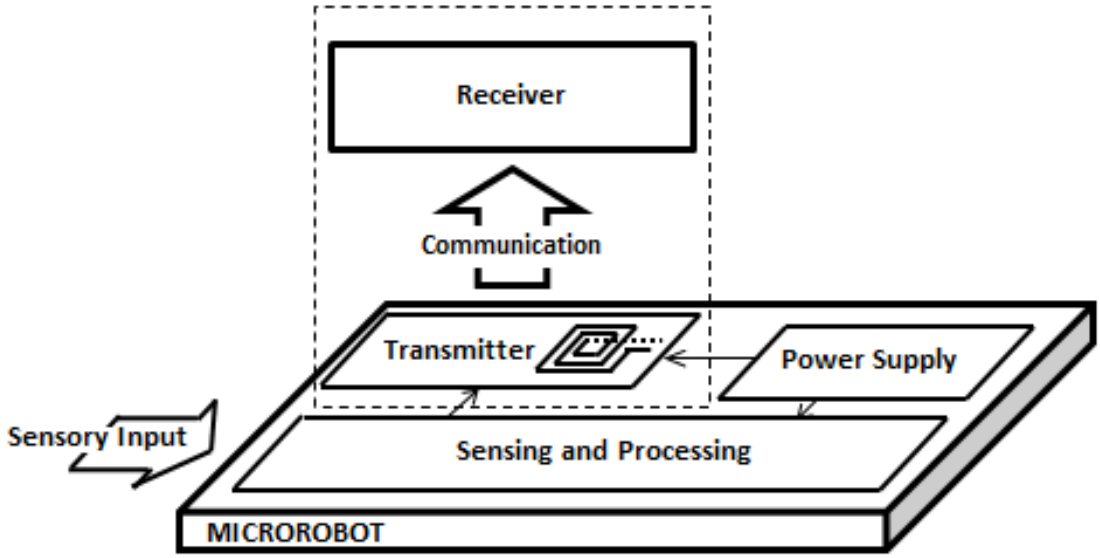

Figure 1-1: Simplified schematic diagram showing the three major parts of the microrobot.

The communication methods for in-vivo application are mainly investigated in the literature for medical implants [19-24] such as implantable pacemakers and defibrillators [20, 25, 26], insulin pumps [21], hearing aids [22] or robotic endoscopy [27-30]. For instance, Ghovanloo et al. [19] developed a high-rate phase-coherent FSK modulation protocol, a wideband inductive link, and three FSK demodulator circuits which are used in wireless implantable neural micro stimulation. Bradley et al. [20] proposed a 402-405 MHz, MICS band transceiver for implantable medical devices which features a low power consumption and a high data transmission rate. However, none of the aforementioned methods are applicable to communicate with a sub-milimetric microrobot due to the lack of power supply and the large size of the receiver antenna. Due to the high degree of system miniaturization, a geometrically small antenna must be embedded on the microrobot. This pushes the communication range to the high frequency domain since the antenna efficiency is directly proportional to its electrical size [31]. However, the electrical permittivity (ε) and conductivity (σ) of the human body as a propagation medium are frequency dependent [32], and the attenuation of human body tissue increases with frequency. This leads to a tradeoff between the size of the microrobot and the amount of attenuation to achieve an efficient wireless link [33].

Hence; there is a need for new approaches to communicate with sub-milimetric microrobots inside human body.

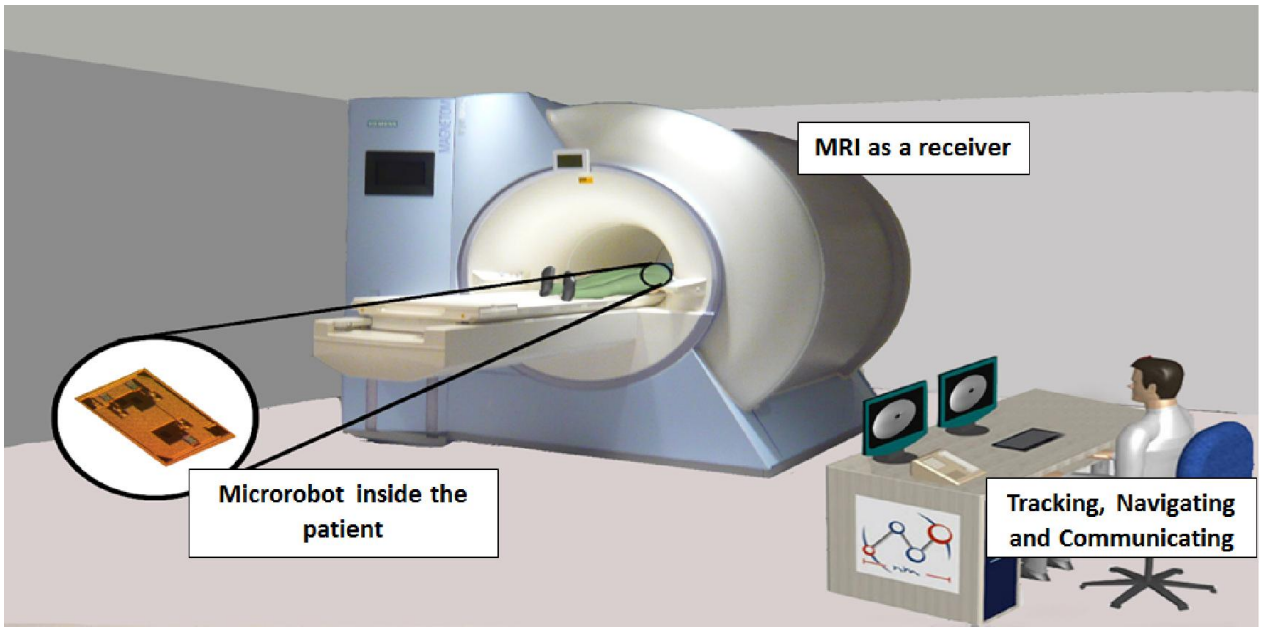

Figure 1-2: Overview of the system.

1.2 Contributions

As shown in Figure 1-2, we propose using a Magnetic Resonance Imaging (MRI) system as a communication mean to overcome the size and power constrains mentioned in Section 1.1. An electrical current passing through the transmitting coil that is embedded in the microrobot generates a magnetic field that interferes with the homogeneous static magnetic field of MRI (B_0) and appears in the MR images as a susceptibility artifact.

First, we proposed a binary communication method in a simplest form in which the direction of the current passing through microrobot's transmitting coil is changed based on the predetermined sensory threshold input. We conducted a set of empirical experiments and showed that the shape of the artifact in MR images is affected by the form of the magnetic field, and as a result, by the direction of the current in the transmitting coil.

However, further investigation showed that the shape of the artifact is also dependent on the orientation of the microrobots. Therefore, prior knowledge of the microrobot's orientation relative to its initial orientation is needed to interpret the MR images.

We overcame the aforementioned limit by proposing a new method in which the frequency of electrical current will change based on the sensory input instead of its direction. We utilize single-shot EPI imaging to detect the frequency of the current. Our simulation and experimental results confirmed the possibility of using this method as a means of communication for microrobots.

Finally, we discussed the possibility of using T1ρ imaging technique as an alternative method of communication to detect higher range of frequencies.

Our study has resulted in the following publications:

- Azadeh Sharafi, Nina Olamaei and Sylvain Martel, ”MRI-based Communication for Untethered Intelligent Medical Microrobots”, *Journal of Micro-Bio Robotics*, 2015
- Azadeh Sharafi , Nina Olamaei and Sylvain Martel, "A new communication method for untethered intelligent microrobots," 2013 IEEE/ ASME conference on Advanced Intelligent Mechatronics (AIM), pp.559,564, 9-12 July 2013
- Azadeh Sharafi and Sylvain Martel, "Magnetic resonance tracking of catheters and mechatronic devices operating in the vascular network with an embedded photovoltaic-based microelectronic circuit, “35th Annual International Conference of the IEEE Engineering in Medicine and Biology (EMBC), 2013 vol., no., pp.2952,2955, 3-7 July 2013

1.3 Organization of the dissertation

The reminder of this dissertation is organized as follows:

Chapter 2 –Literature review: This chapter discusses related work relevant to this dissertation such as a general overview of microrobots in medicine; a survey of micro-power generation, actuation, and control; and communication for microrobots.

Chapter 3 – Binary communication method: This chapter presents a new communication scheme based on binary encoding method.

Chapter 4 – Frequency Based Communication with EPI imaging: This chapter presents our proposed method that utilizes the MRI system to communicate with the microrobot through its frequency.

Chapter 5 – Frequency Based Communication with T1ρ imaging: This chapter presents an alternative method based on T1ρ imaging technique to communicate with the microrobot through its frequency. This chapter covers a brief overview of spin-lock and T1ρ relaxation and how the microrobot magnetic field interacts with the spin-lock field.

Chapter 6 – Conclusion and Recommendation: This chapter concludes the dissertation by summarizing the contributions of our work and presenting possible future works.

CHAPTER 2 LITERATURE REVIEW

Microrobots are untethered devices that are remotely controlled and powered. Being wireless enables the microrobots to work in narrow, complex environment for a long time and maintain high safety. Nelson et al. [1] presents a comprehensive survey of microrobots along with their current and possibly future medical applications. In this chapter, we complement this work by adding previous works related to the medical microrobot function and application.

The rest of this chapter is organized as follows: Section 2.1 focuses on microrobot function, whereas Section 2.2 explores how to provide power for microrobots. Section 2.3 dedicates to the actuation and the control of microrobots followed by the communication techniques presented in Section 2.4.

2.1 Microrobots in medicine

Microrobots can be used to perform several tasks that have been impossible or difficult using traditional methods. Current microrobots allow navigating or transmitting information through complex, narrow structures, e.g., blood vessels [1, 3, 4].

Lu et al., [34] proposed a minimally invasive vascular interventional robotic system consists of propulsion, image navigation and a virtual surgery training system for vascular intervention. The proposed VIS system allows remotely performing angiography and omits the operators exposure to X-ray radiation as they operate the robot far away from the patient.

It is also possible to perform a biopsy using microrobots. The sample analysis is typically performed in an ex-vivo condition. However, if the microrobot is equipped with a type of remote sensing technology, the sample analysis could be performed in situ [1]. The feasibility of in-vivo biopsy with thermally-responsive untethered micro grippers is reported in [35].

Several studies have also reported using a microrobot for endoscopy [27, 28, 36, 37]. For instance, Iddan et al. [27] reported a study presenting a new painless endoscopic imaging of the small bowel. They developed a swallowable capsule of the size of 11×30mm. It passes through gut well and takes photos that are stored on a portable recorder which is capable of recording for more than 5 hours. Their study on ten human subjects confirms the applicability of the capsule [27].

Yan et al. [30] proposed a microrobot for endoscopy which uses a wireless module for communication and power transfer. However, its overall dimension of 12.1mm in diameter and 120.5mm long is the major limitation for using this microrobot for other applications inside human body.

A micro pressure system is proposed in [36] to monitor gastrointestinal (GI) pressure. The system includes a sensor capsule which measures the pressure using a sensitive micro-capacitive sensor in series with an induction coil to form a LC tank. The induction coil is magnetically coupled with a detection coil outside of the subject which is connected to a network analyzer. The change in the pressure leads to a change in the resonant frequency of the LC tank which is quantified by impedance change in the detection coil. The system works without batteries and electrical components for energy transfer. The functionality of the system is confirmed by in-vivo and in-vitro experiments [36].

Ergeneman et al. [38] introduced a microrobotic luminescence oxygen sensor for wireless monitoring of retinal hypoxia. A custom setup for wireless excitation and readout includes a UV LED and a short pass filter for excitation, and a Si photodetector (PD) with a long pass filter for the readout. Magnetic field was exploited to precisely control the sensor in the ocular cavity

A multi-parametric micro-sensor that was proposed by Otto et al. [39] can detect online micro-physiological changes of living cells growing on its glass surface. Changes in pH and pO_2 reflects the metabolic activity and changes the impedance, which is related to morphological properties of the tumor. The overall size of this chip is more than $30mm^2$; therefore, it is only useful for in-vitro experiments.

Another biosensor prototype was proposed by Wang et al. [40]. It has a pH sensor and a temperature sensor on chip as well as a wireless communication system. Again, the dimension (4.1mm × 4.1mm) is the main limitation for using this sensor inside human body.

Microrobots are also promising for targeted drug delivery which can deliver and simultaneously change the dosage of drugs in a specific area of interest [1]. Dogangil et al. [41] proposed a proof of concept of a magnetic microrobot to perform targeted retinal drug delivery. More advanced works complement this method by adding microscope cameras to provide motion-scaling behavior [42] or to map and localize retinal vessels [43] to reduce collateral damage.

In addition, heat (local hyperthermia) or radioactive energy (Brachytherapy) can also be locally delivered to specific regions. These methods are promising approaches to kill the cells of malignant tumors [1]. Sendoh et al. [44] fabricated a microrobot for delivering local delivery of heat energy. They used a high frequency magnetic field to wirelessly produce the heat energy locally. In Brachytherapy, radioactive seeds are placed close to the unwanted cells and the radiated energy kills the cells [45].

2.2 Method of micro-power generation

Different methods can be used to store, harvest, and transmit power for the microrobots. Providing enough power for the circuit is one of the issues that limits the miniaturization of the microrobots. To be used in medical applications, several approaches exist in the literature for power generation which are discussed as follows.

2.2.1 Photovoltaic generation

Photovoltaic power generation is one of the most well-known techniques for scavenging energy in both large and small scale applications. The photovoltaic effect generates voltage by radiating light which transfers electrons between different bands. In order to have an efficient photovoltaic cell, the light direction must be direct and perpendicular to the surface of the cell. Without a direct and high intensity light, the generating capacity of the cell can decrease drastically from 15mW/cm^2 in direct sunlight to 10μW/cm^2 in normal office lighting [46].

The material for fabricating the photovoltaic cell must be selected carefully because the output power can vary over three order of magnitude at low illumination level [47]. For using in medical application, a new structure of a photovoltaic cell is proposed by André and Martel [17]. The experimental results using the cascaded cells of an area of 200μm × 200μm photocell, show a short circuit of 70μA and an open voltage of 0.48V [17].

2.2.2 Thermoelectric generation

Direct thermoelectric generators use the Seebeck effect to directly convert temperature differences into an electrical potential between two material pair junctions [48, 49]. For maximizing the power generation, a large thermal contact area is required. Since waste heat is an abundant source of energy, energy conversion can be continued without interruption. The

efficiency of the conversion is limited by the Carnot efficiency of the generating situation. Large thermal gradients are needed for having efficient production.

It is shown in [50] that it is possible to use human body as a heat source. Because of different kinds of tissues and fluids inside body, human body has non-uniform temperature distribution. A micro-generator is fabricated using an array of polysilicon-germanium (poly-SiGe) thermocouples by Leonov et al. [50] which is mounted to wrist to allow heat absorption directly from the radial artery. Its package size is $3\times3\times1cm^3$ and it is able to generate $4.5\mu W/cm^2$ of power on the radial artery.

In addition to direct conversion, there are works that first convert heat to mechanical actuation and then to electricity using a secondary mechanism [51]. This approach is mainly interested in MEMS device where the mechanical actuation is the final desired energy form. For generating electricity, this approach can be used to actuate electrostatic, electromagnetic, and piezoelectric based generation scheme [52].

2.2.3 Micro-Fuel cells

Micro fuel cells generate electricity from controlled electrochemical reactions [52]. They categorized into two classes of regenerative and non-regenerative generation techniques. Since the non-regenerative cells use toxic materials, they are not suitable for biomedical application. Thus, we discuss only the regenerative cells.

One of the more interesting types of regenerative fuel cells are biological fuel cells (Biofuel). Biofuel cells transform chemical to electrical energy via electrochemical reactions [1]. Utilizing glucose and oxygen that are abundant inside human body (e.g., blood) can power an in-vivo microrobot [1]. These biofuel cells are able to generate $50\mu W/cm^2$ to $430\mu W/cm^2$ for long-term constant generation [53]. Deterre et al. [54] presented the preliminary result of a biocell of a size around $500mm^3$ that can generate $100\mu W$ power. This cell can be potentially used in a pacemaker or other heart implants to provide the required energy. A complete review of the current state of the art biofuel cells is presented in [55] and [56].

2.2.4 Electromagnetic generation

Inductive coupling is often used for wireless power transmission. This approach has been used in different implantable devices [16, 57, 58]. Commonly, the inductive link consists of two coils namely primary and secondary coils. The efficiency of the system is highly related to the quality factor and the coupling between the coils. Hence, it depends on the size, the structure, the distance between the coils, and the properties of the environment surrounding the coils. The coupling decreases drastically when the distance between the coils increases which leads to a decrease in the efficiency [59, 60].

Kumar et al. [61] presented a resonant based wireless power delivery system which uses four coils instead of the common two coils. The efficiency of this system with 22mm diameter implantable coil for a power-link frequency of 700 kHz and a coil distance range of 10 to 20mm is more than 80% [61]. However, the size of the implemented secondary coil on the microrobot with the required electronics still is a serious limitation on the level of miniaturization that can be achieved. Far field approaches such as radio and microwave-based power transmissions have the same disadvantages.

2.2.5 Electrostatic vibration-to-electricity conversion

These types of power supplies generate electricity by transferring charges through a vibration-driven capacitance variance [62-64]. To support power generation, the capacitors must have constant charge during the time; hence, a polarization source must be available to generate additional power [52].

Briefly, in this approach, the variable capacitor is charged when the capacitance is high. Then, using mechanical vibrations, the capacitance is reduced and finally discharged at a desired time. Different types of electrostatic generators are distinguished by their actuation direction [52].

2.2.6 Piezoelectric conversion

Piezoelectric generation is a method of producing power from mechanical vibrations based on the piezoelectric effect. By loading the crystal structure of the piezoelectric material, the micro-structure of the crystal is deformed. Piezoelectric generation is frequency dependent, and it is maximized when the frequency at which the system is driven is at resonance [65].

There are two piezoelectric effects: direct and converse. When we maintain electrical equilibrium within the crystal, the electrons become mobile and shift and a current is created. This phenomenon is referred to the direct piezoelectric effect, which is used to convert the vibration to electricity. Alternatively, the exact opposite phenomenon, which creates the vibration by applying an electric field is called the converse piezoelectric effect.

The direct piezoelectric effect is used for micro generation and it can be used as a force sensor. While, the converse piezoelectric effect is used mainly as actuators [52].

A piezoelectric film is required to convert the displacement and strain into electricity in piezoelectric micro-generator. Three materials that can be used for this application are lead zirconate titanate (PZT), zinc oxide (ZnO) and aluminum nitride (AlN). ZnO and AlN are more commonly used in actuation while PZT is mainly used for power generation purposes [52]. An example of this would be the PZT microfiber generator developed by Ishisaka et al. [66] that used the contractions of a heart muscle to actuate the piezoelectric microfiber generator. Zinc Oxide nanowires were also used to generate electricity on a microscale [67, 68].

2.3 Actuation and control

For locomotion, microrobot power must be transduced into motion [69]. The actuation method must be chosen based on the operational environment (e.g., blood vessels, soft tissues, cavities, and etc.) [1].

Several approaches have been used for the wireless actuation and propulsion of microrobots which are briefly discussed as follows:

2.3.1 Actuation with magnetic field gradient

The magnetic movements of objects within the body has been practiced for a long time [70]. The recent advancement in the related technologies such as superconductors, magnetic materials, and medical imaging makes the magnetic manipulation a promising approach in medical applications [70].

Gardi et al. [71] presented a set of in vivo experiments in which a permanent magnet was inserted and moved to the designated destination under the fluoroscopic guidance. Yesin et al. [72] studied an idea in which an untethered microrobot is steered inside body fluids while a pair of

coils developed a gradient field and superimposed a uniform field of another pair of electromagnetic coils. Meeker et al. [73] complement the work of Gardi and used several stationary coils instead of one to develop a force on the implanted magnet. In a recent work, Steager et al. [74] presented a magnetically actuated microrobot to automatically manipulate cells and microbeads. They also demonstrated how their proposed robot delivered microbeads to specific location on neuron.

Several previous works also used a clinical MRI system to guide and position ferromagnetic beads [75, 76]. Mathieu at al. [75] presented how to use a clinical MRI system to propel micro devices for the first time. The proposed mathematical model and the results of experiments show that a MRI system could provide enough magnetic force to move a ferromagnetic bead inside human cardiovascular system. In addition, Martel et al. demonstrated the feasibility of the aforementioned method [75] for in vivo navigation of untethered robots [76].

Instead of using permanent magnets, some previous works used soft-magnetic MEMS microrobots. These MEMS devices become magnetized easily compared to permanent magnets (e.g., ferromagnetic beads), therefore it is more feasible to control these devices wirelessly over long distances [1]. Moreover, additional MEMS functionalities can be added to these MEMS devices [77, 78]. Nagy et al. [78] focused on a soft-magnetic 3D MEMS devices and proposed a method of the fast computation of magnetic force and torque acting.

Some previous works have focused on the steering of nanoparticles instead of one microrobot. Compared to a single microrobot, a set of particles has a higher chance of avoiding obstacles and rapidly penetrating through narrow spaces [1, 79]. The nanoparticles are useful to be used in a wide variety of biomedical applications including targeted delivery and hyperthermic treatment of cancers [79]. Kalambur et al. [79] investigates the movement and the heating of three different types of magnetic nanoparticles in vitro.

Instead of designing and developing an actuation control system, several previous works utilize microorganisms that could swim as self-propelled natural microrobots [6-9, 80]. Martel et al. [8] used a swarm of magnetotactic bacteria (MTB) to move forward beads of the size of 3µm by the average velocity of 75µm/s. Moreover, They also demonstrated that how micrometer-scale objects can be controlled and transported by a set of MTBs to assemble micro-structure, a

miniature version of an ancient Egyptian pyramid [80] and proposed a new mathematic framework to navigate and deliver the drug using MTB [6, 7].

2.3.2 Helical Propulsion

Helical propulsion uses some form of helical propeller for locomotion. A controlled locomotion method for untethered microrobots using the Artificial Bacterial Flagella (ABF) is reported in [81]. The helical swimmer has a helical tail and a thin soft-magnetic head and is steered using three orthogonal electromagnetic coil pairs. The ABFs can manipulate with a full six degrees of freedom, therefore, they may potentially be used for medical and biological applications under 3D control for fluid environments [81].

2.3.3 Traveling-wave propulsion

Similar to eukaryotic flagella, several approaches use a travel wave for propulsion generation [1]. Kosa et al. [82] presented and experimentally verified a swimming method that works based on the creation of a traveling wave along a piezoelectric beam. They also proposed a hybrid approach that used both electrical power and a static magnetic field to generate propulsion force [83].

2.4 Communication

The communication methods for in-vivo application are mainly investigated in the literature for medical implants [19-24], such as implantable pacemakers and defibrillators [20, 25, 26], insulin pumps [21], or hearing aids [22] or robotic endoscopy [27-30].

Ghovanloo et al. [19] developed a high-rate phase-coherent FSK modulation protocol, a wideband inductive link, and three FSK demodulator circuits which is used in wireless implantable neural micro stimulation. One of the demodulator circuits, digital FSK, occupies 0.29mm^2 and consumes 0.38mW at 5V. This circuit was simulated up to 4 Mbps, and experimentally tested up to 2.5 Mbps, while receiving a 510-MHz FSK carrier signal.

Bradley et al. [20] proposed a 402-405 MHz MICS band transceiver for implantable medical device which features low power consumption and high data transmission rate.

It has a unique ultra-low power wakeup system that consumes an average sleep current of less than 250nA. The transceiver consumes less than 5mA current and operates with a supply voltage between 2.1-3.5 V.

Bohorquez et al. [23] present a 350μW FSK/MSK transmitter and a 400μW super-regenerative receiver architecture optimized for using in medical implants. The transmitter was implemented in CMOS 90nm technology. A frequency correction loop was presented to eliminate the frequency synthesizer in the implant which leads to reduction in power consumption, device size, and system cost. The transceiver antenna has a diameter of 2.3cm.

However, none of the aforementioned systems can be employed to communicate with a sub-milimetric microrobot due to the lack of power supply as well as their embedded antenna size.

CHAPTER 3 BINARY COMMUNICATION METHOD

In this chapter, we propose an on-off communication scheme based on the binary encoding method. Binary encoding is known to be reliable, tolerant to excessive noises, and simple, which is critical considering the technical constraints imposed by the miniaturization of microrobots. Our binary method works based on detecting the direction of the current-induced magnetic field of the microrobot in MR images. Based on the information sent from the sensory component, the microrobot would trigger its communication circuit to alter the direction of the current circulating through its transmitting coil.

If the magnetic field generated by microrobot is detectable in a MR image, this would form a basic communication scheme in which the MRI scanner acts as a receiver. To investigate the feasibility of our proposed communication method, we try to answer the following two fundamental research questions.

- (RQ3.1): Is the sensitivity of MRI sufficient to allow the microrobots to be miniaturized to an appropriate level?
- (RQ3.2): Is the MRI scanner able to detect the direction of the current from an image of the local magnetic field surrounding the microrobot; and hence, is such a communication scheme valid and workable?

To answer these questions, we performed the following steps:

1. To map the simulated magnetic field of the coil on an actual MR image to determine the minimum magnetic field detectable by this setup.
2. To simulate a planar coil and investigate the effect of physical parameters of the coil on magnetic field to show the possibility of shrinking the size of the coil to the appropriate level for microscale applications.
3. To perform an experiment to analyze the effect of magnetic field on MR images.

Our result confirmed that the effect of alteration in the current direction is visible in MR images. Therefore, our proposed communication method is applicable to future medical microrobots.

The rest of this chapter is organized as follows: Sections 3.1 and 3.2 provides the steps that we followed to answer RQ3.1 along with the results. The RQ3.2 is discussed in Section 3.3 followed by the conclusion in Section 3.4.

3.1 RQ3.1: Defining the magnetic field threshold

To answer RQ3.1, we design and perform an experiment to define the minimum detectable magnetic field from a DC-current in MR images. The MR image was acquired by conducting the following experiment. Then, the magnetic field of the coil with the same specification was simulated and mapped on the actual MR image.

3.1.1 Experiment setup

A three turn double layer planar coil as the microrobot's transmitting coil was designed in Eagle CAD (CadSoft Computer, USA) and converted to the LMD format using LPKF CircuitCAM software. The file of the design was then provided to the LPFK ProtoMat 95s/II milling machine (LPKF Laser & Electronics AG, Germany) as an input to build the coil from a copper PCB. The specifications of the coil were: outer diameter = 3mm, inner diameter = 1.4mm, track width = 200μm, gap size (space between adjacent conductors) = 200μm (Figure 3-1a). EPO-TEK® 301-2 epoxy resin (Epoxy Technology Inc., USA) [84] was then applied to both sides of the coil to make it water resistant.

A commercial power supply (Agilent E3631A, Agilent Technologies, USA) was used to generate electrical currents in the coil during the imaging sequence.

During imaging, the signal generator was placed inside MRI room in a safe distance from the MRI magnet bore and connected with wires to the coil inside the MRI bore. To acquire MR data, the coil was suspended inside a solution made of gelatin (Figure 3-1b).

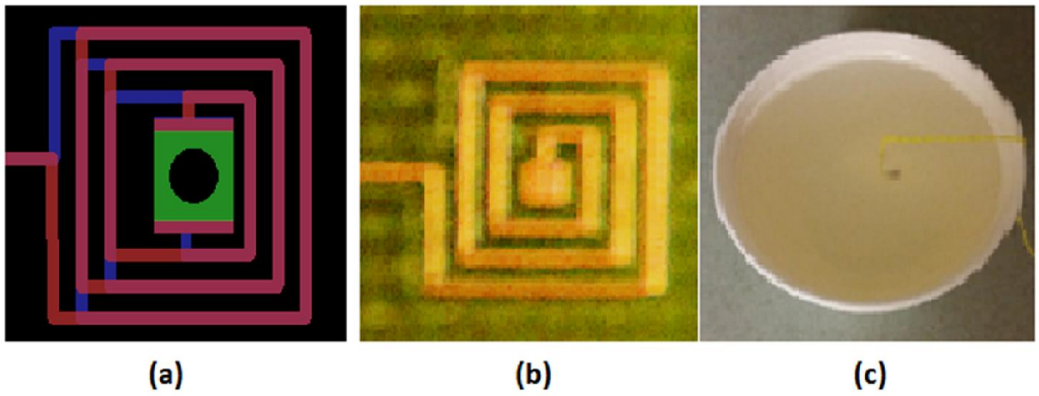

Figure 3-1: (a) The coil design in EagleCAD (b) Fabricated planar coil (c) Suspending the coil in gelatin for imaging purpose

Table 3-1: Imaging Parameters

System	Siemens Magnetom 1.5T
Sequence Name	GRE_Field_Mapping
Repetition Time (*TR*)	500ms
Echo Time (TE)	120ms
Image matrix	384×384
Pixel Size	0.3mm×0.3mm
Slice Thickness	5mm
Flip angle	90º

MR images were taken using Siemens Magnetom 1.5T Magnetic Resonance Imaging System. Afterward, the magnetic field of a coil with the same specification was calculated and mapped on the image to determine the minimum magnetic field detectable in the MR images. The imaging parameters are shown in Table 3-1. Clinical GRE_Field_Mapping sequence was selected to generate a phase image. The parameters were set to result largest artefact while maintaining SNR.

3.1.2 Simulation framework

The schematic of a planar coil is shown in Figure 3-4. It is assumed that the coil is parallel to the *x*-*y* plane.

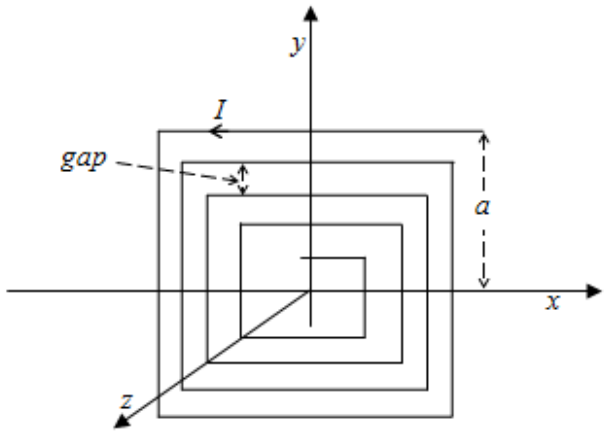

Figure 3-2: The schematic of planar coil

The magnetic field of a finite straight wire can be calculated using Biot-Savart law according to:

$$H = \frac{I}{4\pi}\oint \frac{d\vec{l}\times\vec{r}}{\left|\vec{r}^{3}\right|} \tag{3-1}$$

where $\vec{r}$ is the full displacement vector from the wire element to the point at which the field is being computed. Applying Eq.(3-1) for a wire carrying current *I*, parallel to the *x*-*z* plane as presented in [85], we obtain:

$$H_x = 0$$

$$H_y = -\frac{zI}{4\pi}\int_{x_1}^{x_2}\frac{dl}{\left[\sqrt{(x-l)^2+(y-a)^2+z^2}\right]^3}$$

$$= -\frac{zI}{4\pi\left[(a-y)^2+z^2\right]}\times\left[\frac{x_2-x}{\sqrt{(x_2-x)^2+(a-y)^2+z^2}}-\frac{x_1-x}{\sqrt{(x_1-x)^2+(a-y)^2+z^2}}\right]$$

$$H_z = \frac{(y-a)I}{4\pi}\int_{x_1}^{x_2}\frac{dl}{\left[\sqrt{(x-l)^2+(y-a)^2+z^2}\right]^3}$$

$$= -\frac{(a-y)I}{4\pi\left[(a-y)^2+z^2\right]}\times\left[\frac{x_2-x}{\sqrt{(x_2-x)^2+(a-y)^2+z^2}}-\frac{x_1-x}{\sqrt{(x_1-x)^2+(a-y)^2+z^2}}\right] \quad (3\text{-}2)$$

where x, y, z are the position at which the magnetic field is calculated. x_1 and x_2 are the x-coordinate at the end of the straight wire, I is the current passing through the coil, dl is the differential spatial element on the wire segment, and a is the distance between each wire and the center of the coil as shown in Figure 3-2. The magnetic field of the wire parallel to y-z plane can be calculated in a similar manner [85]:

$$H_x = -\frac{\mu z I}{4\pi\left[(a-x)^2+z^2\right]}\times\left[\frac{y_2-y}{\sqrt{(y_2-y)^2+(a-x)^2+z^2}}-\frac{y_1-y}{\sqrt{(y_1-y)^2+(a-x)^2+z^2}}\right]$$

$$H_y = 0$$

$$H_z = -\frac{(a-x)I}{4\pi\left[(a-x)^2+z^2\right]}\times\left[\frac{y_2-y}{\sqrt{(y_2-y)^2+(a-x)^2+z^2}}-\frac{y_1-y}{\sqrt{(y_1-y)^2+(a-x)^2+z^2}}\right] \quad (3\text{-}3)$$

where y_1 and y_2 are the y coordinate at the end of the straight wire.

The magnetic field of the coil in an arbitrary position (x, y, z) is calculated by superposition of the field vectors of all straight wires. Subsequently, the magnetic flux, ΔB_m is calculated as:

$$\Delta B_m = \mu_0 \mu_r H \quad (3\text{-}4)$$

where μ_r is the relative permeability of the material in which the field has been calculated and $\mu_0 = 4\pi\times10^{-7}$ is the free space permeability.

3.1.3 Results

The magnetic field of the coil with the same specification as the one used in the experiment was calculated in MATLAB from Eqs.(3-2), (3-3) and (3-4) and mapped on the acquired MR image from the experiment. Figure 3-3 shows the MR image of the planar coil along with its simulated

magnetic field. As illustrated in Figure 3-3, a magnetic field as small as 50nT is detectable in the MR image. We considered this amount as the threshold value for the magnetic field to be detected in MR images.

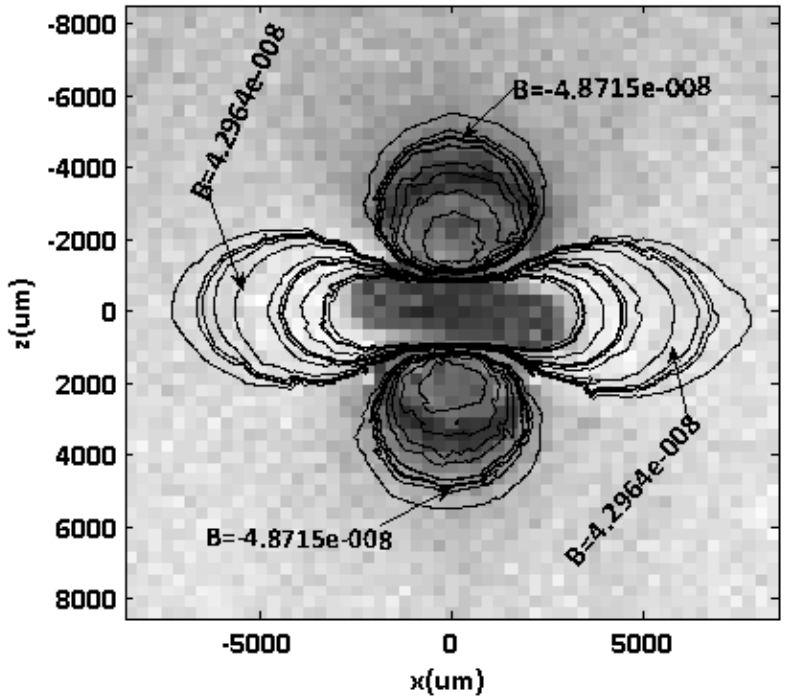

Figure 3-3 : Mapping simulated magnetic field to MR image of a coil with the same specification. It is possible to detect magnetic field as small as 50nT in MR images. Coil specification: Number of turns = 3, Number of layers = 1, Gap size = 200µm, Track width = 200µm, Outer diameter = 3000µm. Inner diameter = 1400 µm, *I*=5mA.

3.1.3.1 Effect of echo time

The measure signal at the echo time in the presence of current-induced magnetic field of the microrobot can be written as [86]:

$$s(\vec{r},TE)=\int_{v}\rho(\vec{r})e^{-i2\pi\gamma G_x\vec{r}TE-i2\pi\gamma\Delta B_m(\vec{r},t)TE}dv \tag{3-5}$$

while ρ is the proton density, G_x is the readout gradient and $\vec{r}$ is the position vector. The term $-2\pi\gamma\Delta B_m TE$ shows the additional phase dispersion at the the echo time (*TE*).

As shown in Eq.(3-5), the amount of phase change and consequently the measured MR signal are related to the amount of magnetic field inhomogeneity as well as *TE*. As shown in Figure 3-4, increasing *TE* leads to the larger artifact. Hence, the minimum detectable magnetic field also depends on *TE* and the threshold magnetic field must be defined based on the specific value of *TE* used in acquiring the MR image.

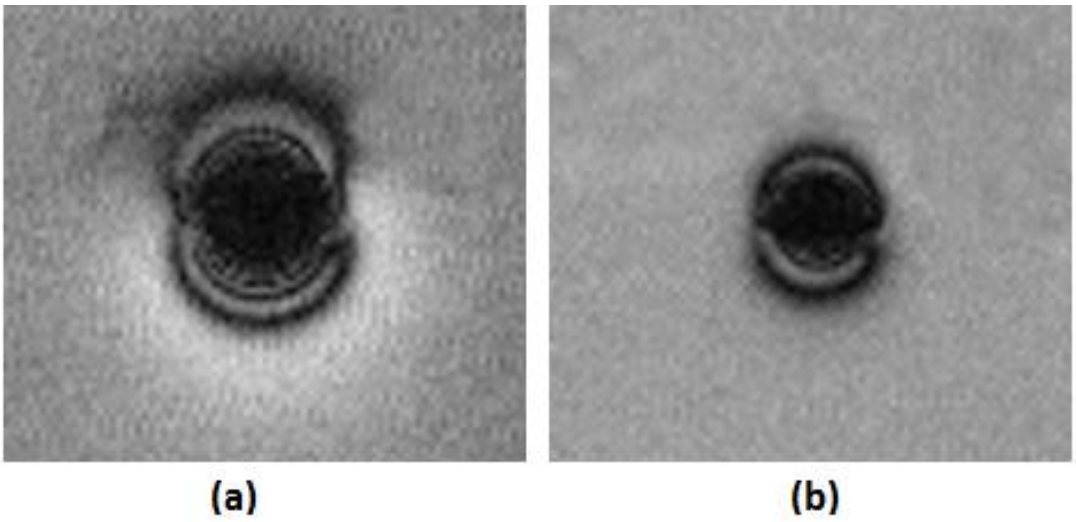

Figure 3-4: Effect of echo time on the susceptibility artifact. Axial image from the coil in coronal plane while applying 5*mA* electrical current. (a) TE=120ms (b) TE=30ms.

3.2 RQ3.1: Determining the coil size

The result of previous experiment confirms the possibility of detecting a magnetic field as small as 50nT. To show the possibility of generating this magnetic field with a microcoil, the effects of the physical parameters of the coil including gap size, number of turns, number of layers, and inner diameter on its magnetic field was investigated.

The magnetic flux is shown in Figure 3-5 for different gap sizes at x=0, y=0 and z=0. As expected, decreasing the gap size causes a significant increase in the magnetic flux. It also decreases the total size of the coil. The minimum gap size depends on the equipment used for the fabrication of the coil. For example, the minimum distance between two tracks using LPKF ProtoMat 95s/II milling machine is 100µm. Hence, the minimum gap size is 100µm. This distance can be decreased to 5µm when fabricating the coil in CMOS 0.13µm technology.

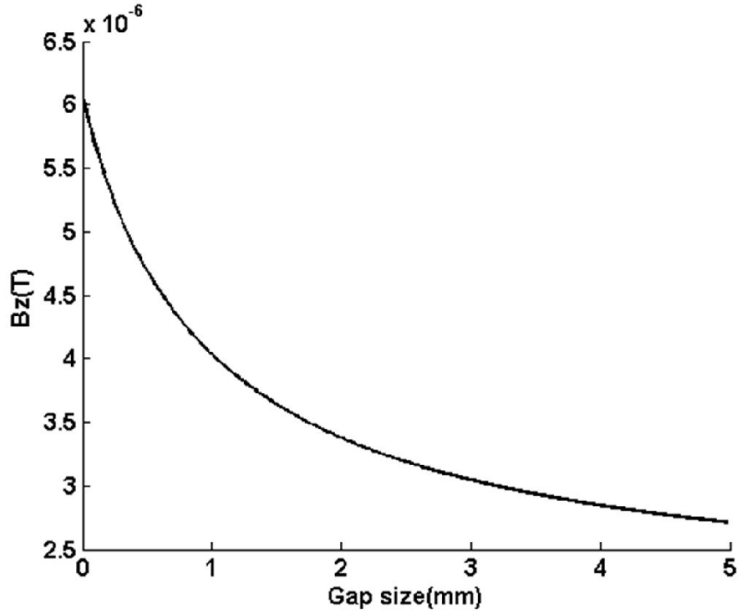

Figure 3-5: Effect of the gap size on the magnetic field (Number of turns = 3, Inner diameter = 1400μm, *I* = 5mA)

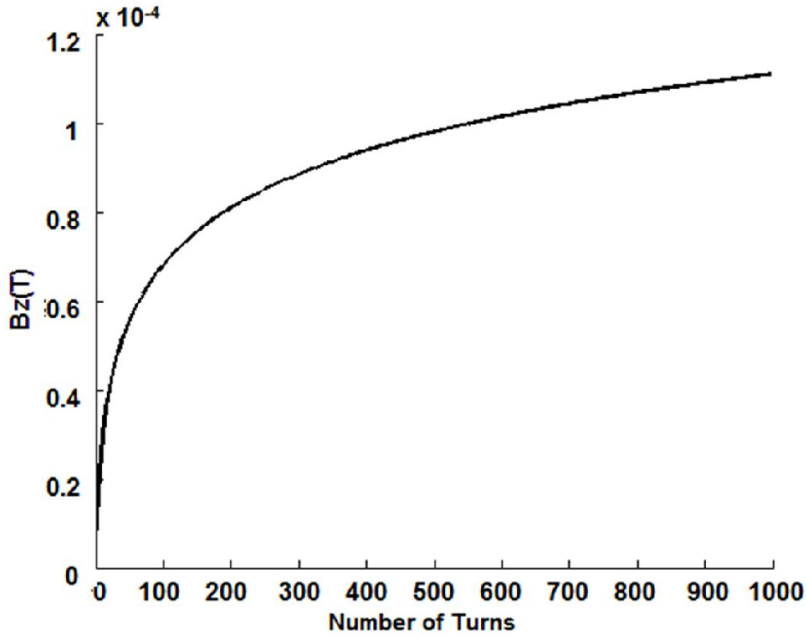

Figure 3-6: The effect of number of turns on magnetic field (Gap size = 200μm, Track Width = 200μm, Inner diameter=1400 μm, *I*=5mA).

The magnetic flux can be further increased at the cost of increasing the overall size of the coil with a larger number of turns as shown in Figure 3-6. Moreover, increasing the layers will increase the total magnetic field (Figure 3-7).

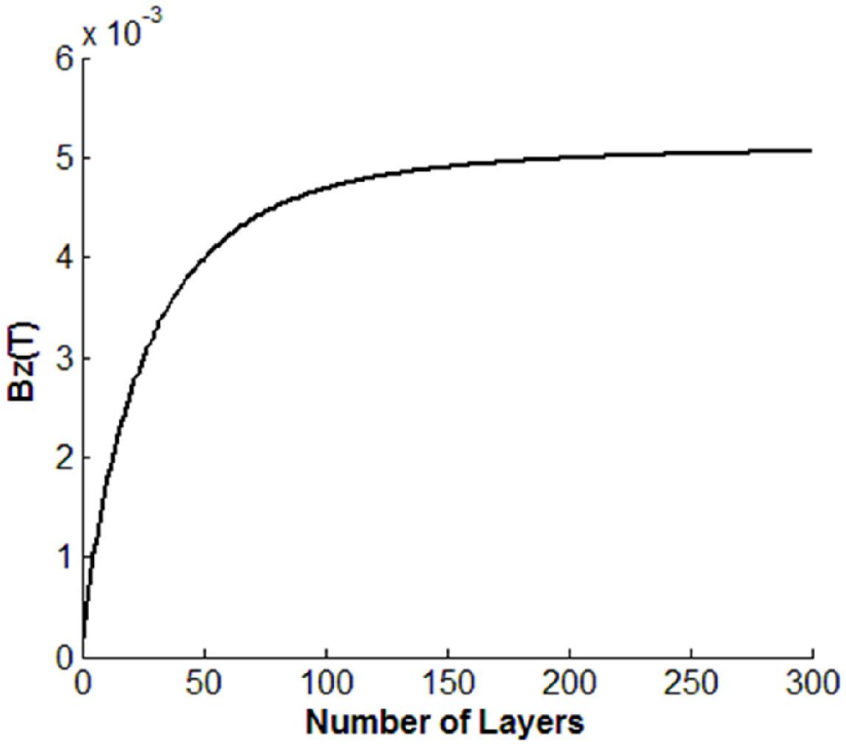

Figure 3-7: Increasing the magnetic field by increasing number of layers. Number of turns = 3, Gap size = 200µm, Track Width = 200µm, Inner diameter=1400µm, I = 5mA.

The magnetic flux, B, along the z-axis is shown in Figure 3-8 for different inner diameters of the coil at x=0 and y=0. As shown in Figure 3-8, decreasing the inner diameter increases the maximum magnetic field effect. We considered that the magnetic field produced by the coil should vary across a threshold distance of at least three pixels to be detectable in MR images. Considering the pixel size of 300µm, the amount of the magnetic field should be higher than its threshold at z=900µm. For example, in Figure 3-8, the amount of magnetic field at z=1 mm for an inner diameter of 100µm is 39nT, which is below the threshold, while it is 148nT for a coil with an inner diameter of 200µm.

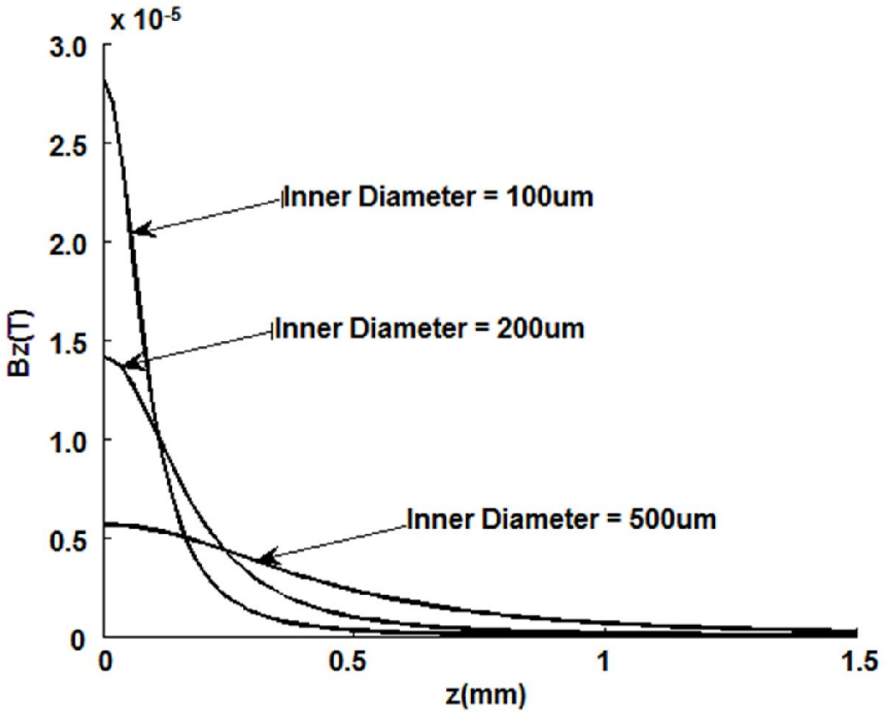

Figure 3-8: Effect of coil inner diameter on magnetic field. Number of turns = 1, Number of layers = 1, I = 5mA. A coil with smaller inner diameter has larger magnetic field in the beginning but the field decreases faster as the distance from the center of the coil increases.

Considering all parameters, the simulation results show that it is possible to generate a magnetic field as small as 50nT with a double layers coil with an outer diameter of 700µm by delivering a current of 70µA to the coil. This amount of current is delivered using micro-power generation techniques presented in some previous works such as in [17]. It is possible to fabricate such coil in CMOS 0.13µm technology. Figure 3-9 shows the magnetic field generated by the mentioned coil in the *x*-*z* plane. Each square grid is equal to a pixel in the MR image (0.3mm). Since the magnetic field at the third pixel from the center of the coil is larger than 50nT, we can state that at least 3 pixels around the coil are affected by a current induced magnetic field larger than 50nT. As a result the magnetic field produced by the coil is clearly visible in the MR image.

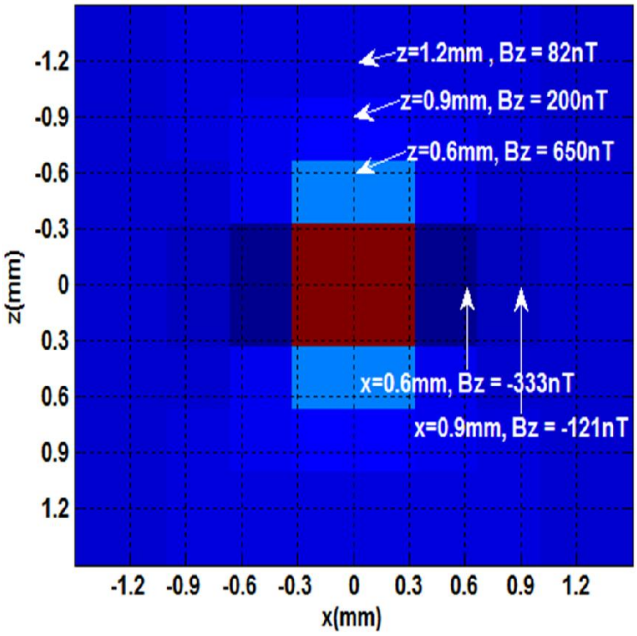

Figure 3-9: Current-induced magnetic field generated by a double layers coil in coronal plane. Each square grid is equal to a pixel in MR image. The amount of magnetic field at the third pixel from the center of the coil is higher than 50nT and thus is visible in the MR image. Coil specifications: Inner diameter = 200µm, Gap size = 5µm, Track width= 5 µm. Number of turns = 30 in each layer.

3.3 RQ3.2: Binary communication system

As depicted in Eq.(3-5), the amount of phase dispersion in the MR signal is related to the direction of the magnetic field as well as its magnitude. This phenomenon is the basis of our proposed communication method.

3.3.1 Experiment setup

An experiment was carried out with the coil used in Section 3.1.1. The imaging parameters are shown in Table 3-1.

The coil was placed in coronal plane so the *x*-component of its magnetic field, B_x, becomes parallel (or anti-parallel) to the B_0. Then, a MR image was acquired while applying 5mA current to the coil. Next, another image with the same imaging parameters was taken while the applied current was alternated to the opposite direction.

To investigate the effect of rotation, the coil was rotated into different positions and images were taken for each current direction. Two types of rotations were considered: in-plane rotation where there is a 2D rotation in the same plane and through-plane rotation where the coil was rotated from the coronal plane to the axial or sagittal planes; and therefore; its B_z and B_y move parallel to the B_0 respectively. The simulation was performed for several in-plane and through-plane rotations and confirmed by experiment.

3.3.2 Results

3.3.2.1 Detection of current direction with MRI

The simulated magnetic field and the MR images of the coil placed in coronal plane while applying DC current in two opposite directions is shown in Figure 3-10.

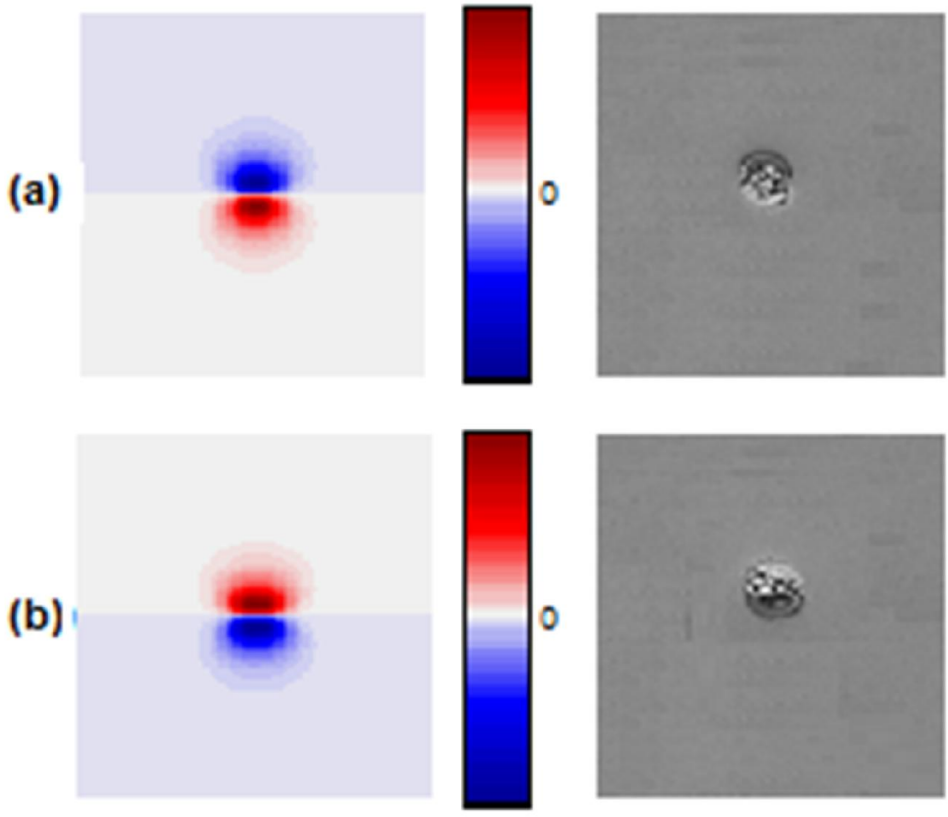

Figure 3-10: Binary communication system. Axial MR image was taken from the coil in the coronal plane. (a) Simulated magnetic field and MR image while applying 5mA current. (b) Applying the current in the opposite direction.

As shown in Figure 3-10, the effect of alternating the current's direction can be detected in the images and hence the proposed communication method is valid and demonstrable.

3.3.2.2 Rotation effect

3.3.2.2.1 Through-plane rotation

First, the coil was rotated from the coronal to axial plane. The simulated magnetic field of the coil and the MR images is shown in Figure 3-11. Then it was rotated to the sagittal plane. When there is a through plane rotation, there is a change in the shape of the artifact within the MR images.

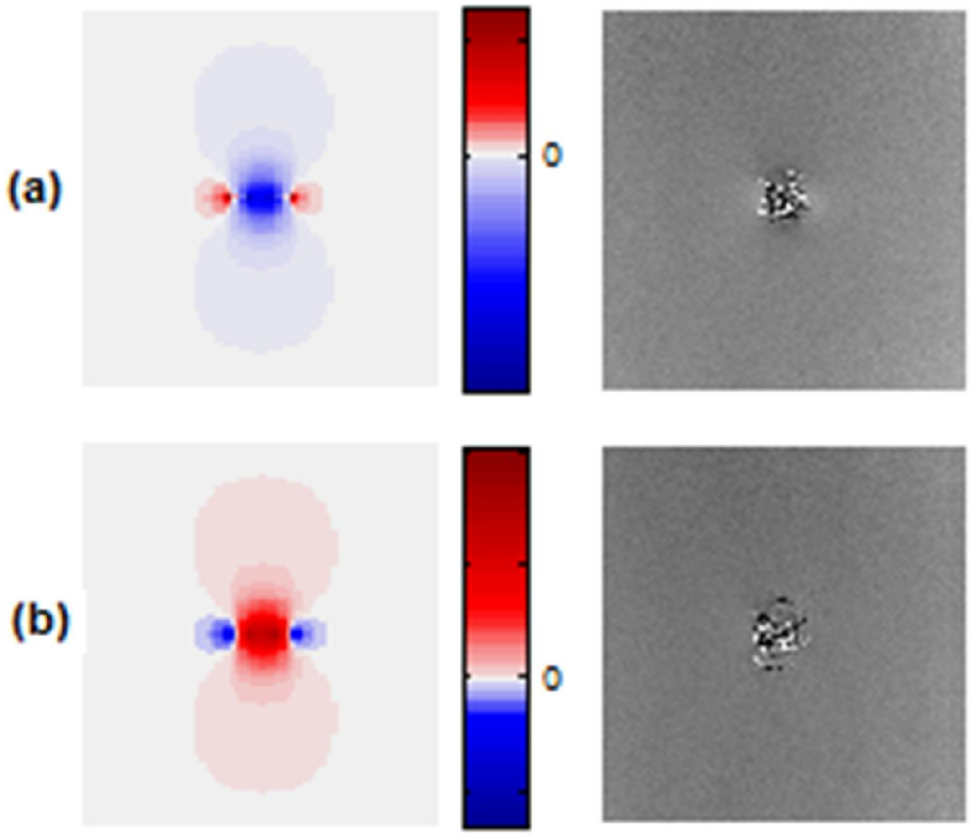

Figure 3-11: Through plane Rotation. Coronal images were taken from a coil in axial plane. (a) Simulated magnetic field and MR image while 5mA current was applied. (b) Applying the current in the opposite direction.

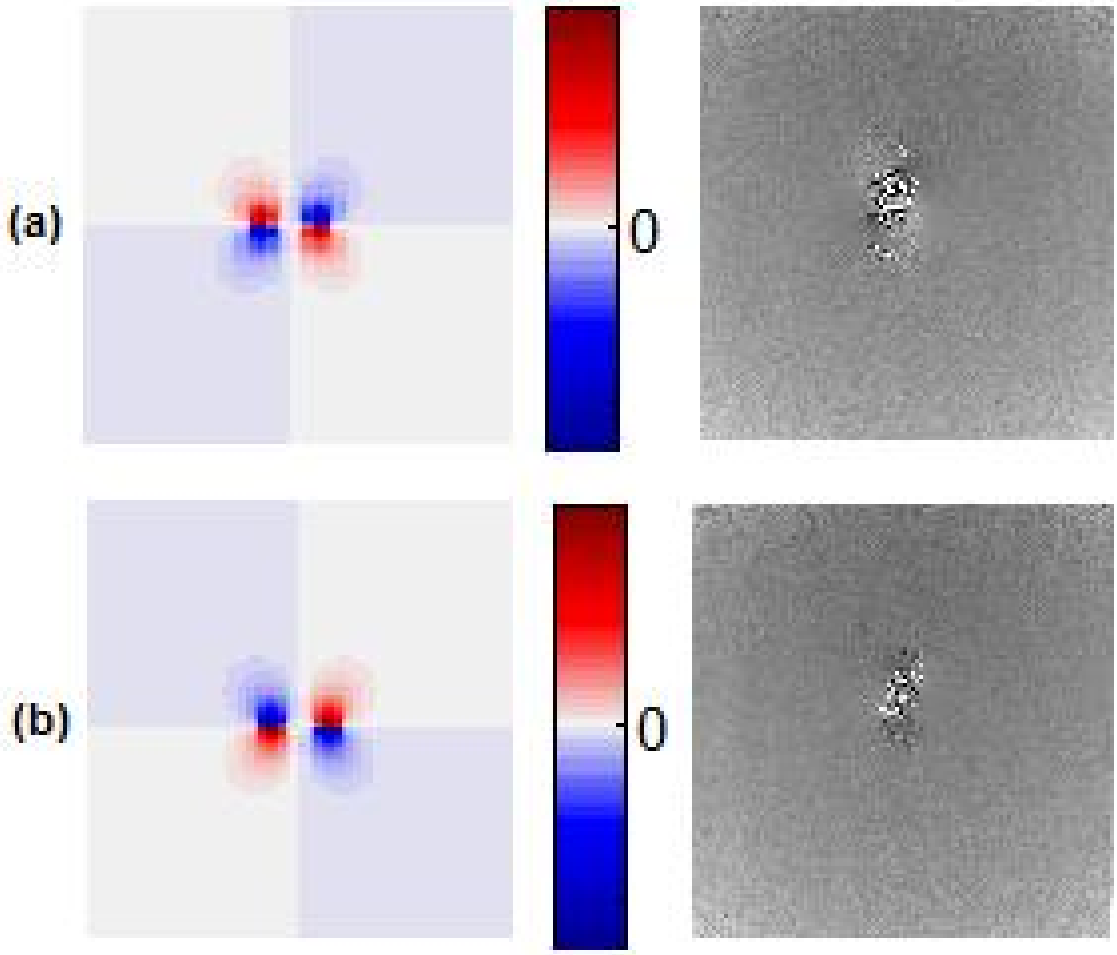

Figure 3-12: Through plane Rotation. Coronal images were taken from a coil in sagittal plane. (a) Simulated magnetic field and MR image while 5mA current was applied. (b) Applying the current in the opposite direction.

3.3.2.2.2 In-plane rotation

Figure 3-13 shows the in-plane the effect of rotating a coil in coronal plane on MR images.

As shown in Figure 3-13, an arbitrary rotation of the coil more than 180^{o} in the same plane causes the change in the result. For instance, it is not possible to distinguish between situations where the coil rotates 180^{o} with the situation where there is no rotation but the current has an opposite direction. Hence, to interpret the MR images, initial knowledge about the orientation of the microrobot is essential.

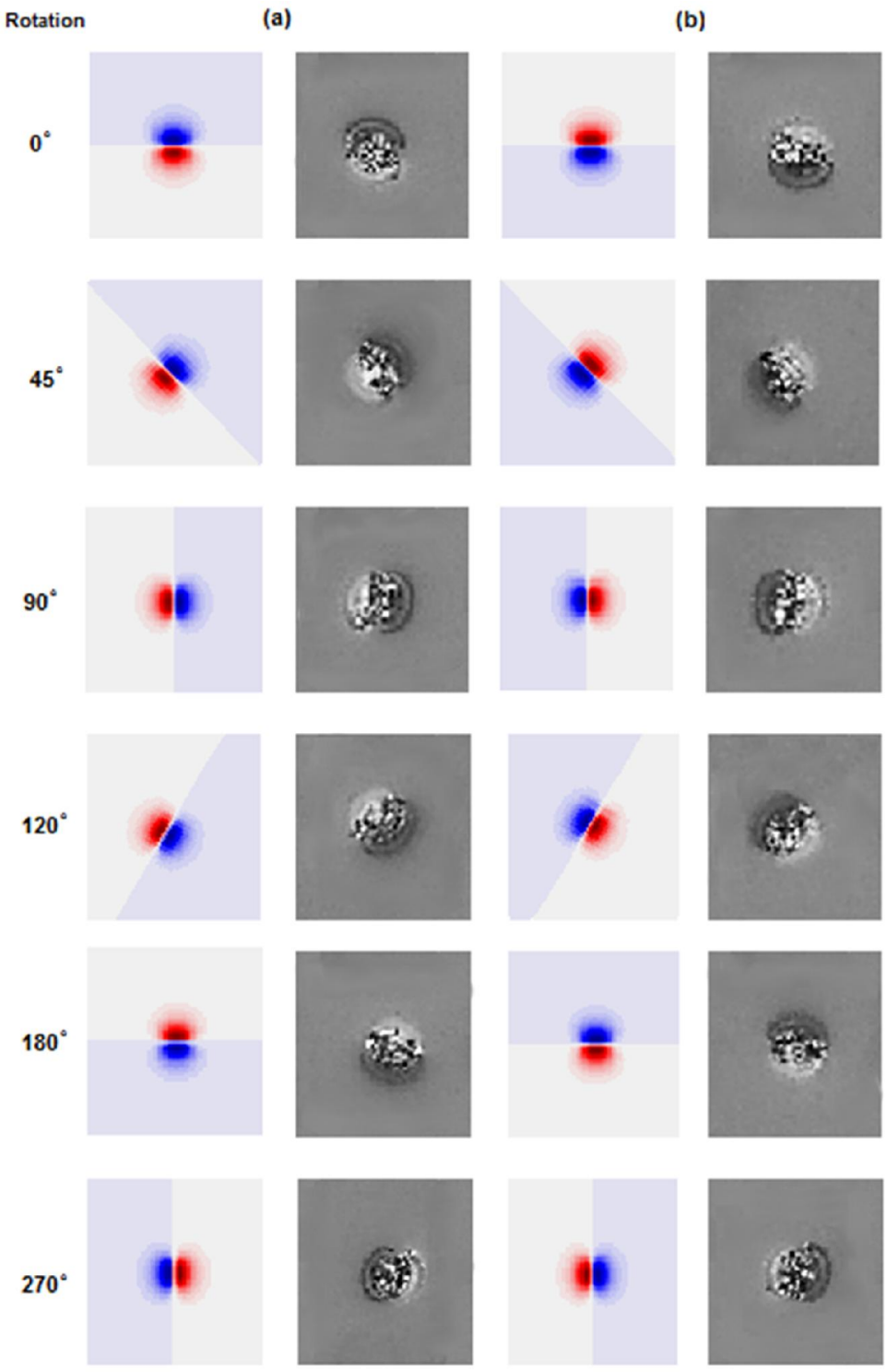

Figure 3-13: Effect of rotation in the current direction based communication system. (a) Simulated magnetic field and coronal MR image of the coil in axial plane while applying 5mA current. (b) Alternating the current direction. It is not possible to distinguish between a.0^{o} and b.180^{o} or a.90^{o} and b.270^{o}.

3.4 Conclusion

In this chapter, a technique was described to exploit MRI scanner as a sensitive receiver to communicate with the microrobots. We proposed a binary communication scheme in the form of a directional alteration in the current circulating in a miniature coil that could be embedded in the microrobot. The direction of the current could be regulated from a predetermined sensory threshold input implemented on the microrobot. The direction of the current provides information about the level of sensory input from a microrobot and it is determined using MR phase encoding images. The results showed that the MRI scanner is able to detect the direction of the current from image of the local magnetic field surrounding the microrobot and it is sensitive enough to detect a magnetic field generated from a miniature coil with appropriate size to be embedded on a microrobot. However, the shape of the artifact in MR images is dependent to not just the current direction but also on the orientation of the microrobots. Hence; knowledge of the microrobot's orientation relative to its initial orientation is essential to interpret the MR images.

CHAPTER 4 FREQUENCY BASED COMMUNICATION WITH EPI IMAGING

In Chapter 3, we proposed a binary communication scheme based on detecting the direction of the current passing through a miniature coil that is embedded in the microrobot using MR phase-encoding images. However, in addition to the current direction, the orientation of the microrobot also affects the shape of the artifact in MR images. Therefore, information about the microrobot's orientation relative to its initial position is required prior to interpreting the MR images.

In this chapter, we demonstrated how we addressed this problem by overcoming the aforementioned limit through the development of a new communication method based on the detection of variations in the electrical current's frequency using the same principle that is presented in [87, 88] for direct mapping of neuronal activity. We showed that the frequency is independent of the rotation of the transmitting coil; hence, it can be interpreted without any initial knowledge of the microrobot's orientation. We also showed that MRI is sensitive enough to detect changes in the magnetic field of a miniaturized transmitting coil embedded into a microrobot.

The remainder of this chapter is organized as follows: Section 4.1 describes the theoretical background behind this method. Section 4.2 explains methodology, simulation framework, and experiment setup to test the proposed communication system. Results are presented and discussed in Section 4.3, followed by the conclusion in Section 4.4.

4.1 Theoretical background

The presence of any field inhomogeneity impacts the formation of MRI images and results in image artifacts known as susceptibility artifacts [89, 90]. The susceptibility effect is the source of two types of artifacts in MR images [91, 92]: geometrical distortion and intensity distortion.

The geometrical distortion corresponds to a misregistration of spin positions due to field variations during frequency encoding. Thus, the misregistered signals appear in a wrong location because of the change in the Larmor frequency of the affected spins.

$$\omega(\vec{r}) = \gamma(B_0 + \Delta B_m(\vec{r})) \tag{4-1}$$

where $\Delta B_m(\vec{r})$ is the parallel or anti-parallel component of the background magnetic field to the main magnetic field B_0 of the MRI scanner.

The position error due to the misregistration is calculated as:

$$x' = x + \frac{\Delta B_m(x)}{G_x} \tag{4-2}$$

Where G_x is the readout gradient.

The intensity distortion is only limited to GRE sequences due to the lack of 180° refocusing pulse. Because of the presence of a background gradient (e.g., magnetic field generated by microrobot), an additional position dependent phase term is added to the echo signal, which leads to a signal loss.

The measure signal at the echo time in the presence of background field of the microrobot can be written as [86]:

$$s(\vec{r}, TE) = \int_v \rho(\vec{r}) e^{-i2\pi\gamma G_x \vec{r} TE - i2\pi\gamma \Delta B_m(\vec{r},t) TE} dv \tag{4-3}$$

while ρ is the proton density, G_x is the readout gradient and $\vec{r}$ is the position vector. The term $-2\pi\gamma\Delta B_m TE$ shows the additional phase dispersion at the the echo time (TE).

As shown in Eq.(4-3), an alternative magnetic field generated by a transmitting coil (ΔB_m) leads to an alternative MR signal variation over time, the frequency of which can be detected by applying a Fourier transform after sampling the signal over time. Single-shot Echo-Planar Imaging (EPI) [93] is a very fast imaging method that can acquire a complete image in a fraction of a second [94]. As a result, the alternative signal can be sampled using real-time EPI images. The sampling rate is equal to the sequence's repetition time (TR). The Fourier transform of the identical pixels on different images acquired over time reveals the frequency of the alternative magnetic field of the coil.

Note that for the single-shot EPI, we define the TR as the total acquisition time for one complete image; Hence, the time between two consecutive images is equal to TR.

Considering the Nyquist criteria, the maximum frequency detectable by this method (f_{max}) is limited by the minimum allowable TR in the sequence:

$$f_{\max} = \frac{1}{2TR_{\min}} \tag{4-4}$$

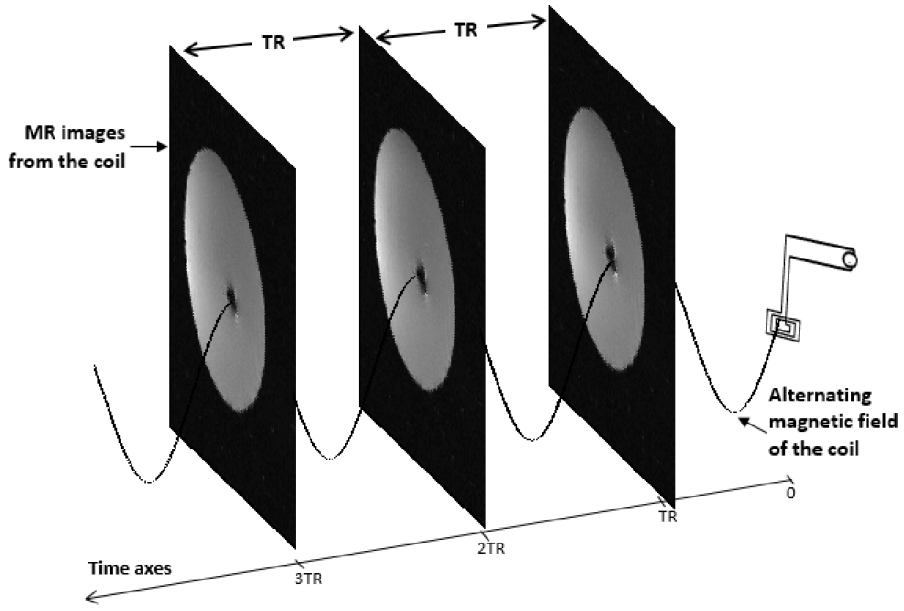

Figure 4-1: The current induced alternative magnetic field of the coil was sampled by taking successive single-shot EPI images from the same slice.

4.2 Material and method

4.2.1 Simulation framework

EPI-GRE sequence was developed in C language and added to SIMRI program [95] to simulate MR images.

The current magnetic field of the planar coil is simulated using MATLAB and added to the SIMRI as field inhomogeneity.

The simulator overview is shown in Figure 4-2

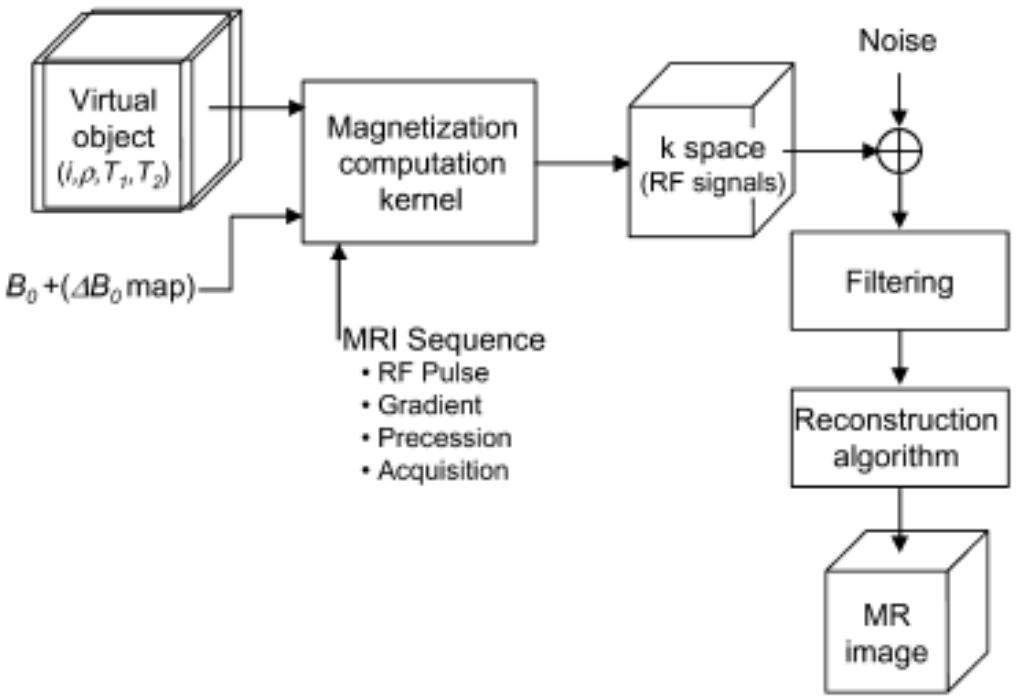

Figure 4-2 SIMRI overview [95]

The virtual object is defined by set of physical parameters that is needed to calculate magnetization vector [95]. These values are spin density (ρ), spin-lattice relaxation time (T_1) and spin-spin relaxation time (T_2);

The magnetization vector is calculated by solving the Bloch Equation [96]

$$\frac{d\vec{M}}{dt} = \gamma(M \times B) - \begin{pmatrix} M_x / T_2 \\ M_y / T_2 \\ (M_z - M_0)/T_1 \end{pmatrix} \tag{4-5}$$

where $\vec{M} = (M_x, M_y, M_z)^T$ is the magnetization vector and M_0 is the spin magnetization in equilibrium which is dependent on proton density and T_1, T_2 relaxation constants. The local magnetic field is defined as:

$$\vec{B}(\vec{r},t) = B_0\vec{z} + \Delta B_m(\vec{r})\vec{z} + (\vec{G}(t)\vec{r})\vec{z} + \vec{B}_1(t) \tag{4-6}$$

Where $\Delta B_m(\vec{r})$ is the local field inhomogeneities, $\vec{G}(t)$ is the applied field gradient, $\vec{B}_1(t)$ is the RF excitation pulse and $\vec{r} = (x, y, z)^T$ is the spatial coordinate [95].

Considering the effect of applying a RF excitation pulse, applying the gradients and spin magnetization relaxation, the magnetization vector evolution can be iteratively computed by [95]:

$$\vec{M}(\vec{r}, t+\Delta t) = Rot_z(\theta_g) Rot_z(\theta_i) R_{relax} R_{RF} \vec{M}(\vec{r}, t) \tag{4-7}$$

where $Rot_z(\theta)$ is a rotation matrix about the *z*-axis associated to the angle θ by:

$$Rot_z(\theta) = \begin{pmatrix} \cos\theta & \sin\theta & 0 \\ -\sin\theta & \cos\theta & 0 \\ 0 & 0 & 1 \end{pmatrix} \tag{4-8}$$

Where θ_g is linked to the applied gradient $\vec{G}(t)$ by:

$$\theta_g = \gamma \vec{r} \int_t^{t+\Delta t} \vec{G}(\tau) d\tau \tag{4-9}$$

Where θ_i is linked to the field inhomogeneities by:

$$\theta_i = \gamma \Delta B_m(\vec{r}) \Delta t \tag{4-10}$$

Where R_{relax} describes the relaxation effects by:

$$R_{relax} = \begin{pmatrix} e^{\frac{\Delta t}{T_2(\vec{r})}} & 0 & 0 \\ 0 & e^{\frac{\Delta t}{T_2(\vec{r})}} & 0 \\ 0 & 0 & 1 - e^{\frac{\Delta t}{T_1(\vec{r})}} \end{pmatrix} \tag{4-11}$$

and where R_{RF} represents the rotating effect of a RF pulse of phase angle ϕ leading to a flip angle α in a time Δt. Considering only one component on resonance, in the absence of any gradient R_{RF} is given by rotation about *z* and *x*-axis [97]:

$$R_{RF} = Rot_z(\phi)Rot_x(\alpha)Rot_z(-\phi) \tag{4-12}$$

In the presence of the magnetic field other than B_0 , R_{RF} is given by Eq.(4-13) [95]:

$$R_{RF} = Rot_z(\phi)Rot_y(\beta)Rot_x(\alpha')Rot_y(-\beta)Rot_z(-\phi) \tag{4-13}$$

with effective flip angle α' as :

$$\alpha' = \Delta t\sqrt{(\Delta\omega)^2 + (\frac{\alpha}{\tau})^2} \tag{4-14}$$

and

$$\beta = \tan^{-1}\left(\frac{\Delta\omega}{\alpha/\Delta t}\right) \tag{4-15}$$

where $\Delta\omega(\vec{r},t)$ is the local value of frequency offset and is calculated by:

$$\Delta\omega(\vec{r},t) = \gamma(B_0 - \vec{B}(\vec{r},t))\vec{z} \tag{4-16}$$

The k-space is filled by calculating one dimensional discrete complex RF signal (*s[t]*) from the magnetization using:

$$s[t] = \sum_{\vec{r}} \vec{M}(\vec{r},t)\vec{x} + j\sum_{\vec{r}} \vec{M}(\vec{r},t)\vec{y} \tag{4-17}$$

The noise is then added to the k space data before applying the reconstruction algorithm including inverse Fourier transform to obtain the final MR image [95].

4.2.2 Experiment setup

A three turn double layer planar coil as the microrobot's transmitting coil was designed in EagleCAD (CadSoft Computer, USA) and converted to the LMD format using LPKF CircuitCAM software. This file was then provided to the LPFK ProtoMat 95s/II milling machine (LPKF Laser & Electronics AG, Germany) as an input to build the coil from copper PCB. The

square planar structure was selected due to the ease of miniaturization and embedding in the microrobot using CMOS technology. The specifications of the coil were: outer diameter = 3mm, inner diameter = 1.4mm, track width = 200µm, gap size (space between adjacent conductors) = 200µm (Figure 4-3b). EPO-TEK® 301-2 epoxy resin [84] (Epoxy Technology Inc., USA) was then applied to both sides of the coil to make it water resistant.

A commercial signal generator (Agilent 33220A, Agilent Technologies, USA) was used to generate electrical currents with various frequencies in the coil during the imaging sequence.

During imaging, the signal generator was placed in the control room and connected with wires to the coil inside MRI through the penetration panel. To acquire MR data, the coil was suspended inside a solution made of gelatin (Figure 4-3c).

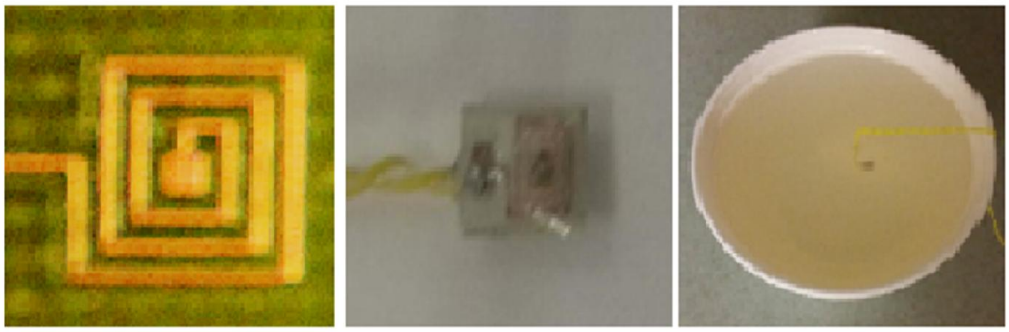

Figure 4-3: (a) The planar coil on PCB (b) Applying water resistant epoxy on the surfaces (c) Suspending the coil in gelatin for imaging purpose.

4.2.3 MRI experiment

To detect changes in the magnetic field at different frequencies, a susceptibility-sensitive sequence with a high temporal resolution was required. Gradients echo (GRE) sequences are known to be sensitive to the susceptibility artifact due to the lack of the 180^{o} RF pulse [98, 99].

A single-shot GRE echo planar (EPI-GRE) sequence with a temporal resolution of 220ms was applied to acquire the images. In a single shot sequence, one image was acquired during one repetition time. So the acquisition time is determined by the duration of TR. On the other hand, the maximum detectable frequency is limited by the acquisition time. As such, the TR was set to the

minimum value allowed according to the sequence parameters. According to the parameters of the imaging sequence and the Nyquist criteria, the maximum detectable frequency was f_{max}=2.27Hz.

The imaging parameter is shown in Table 4-1. Two arbitrary frequencies lower than 2.27Hz were chosen (0.5Hz, 1Hz) to show two states of binary communication. The amplitude of the electrical current was fixed, and the frequency was set to 1Hz in the first set, and then changed to 0.5Hz in the second set of the experiment. In each set of experiments, fifty images were obtained from the same slice. Afterward, a frequency map was built by applying the Fourier transform on each pixel for all the 50 slices prior to the detection of the peak frequency.

Table 4-1: Sequence Parameters.

System	Siemens Skyra 3T
Sequence Name	GRE_EPI(ep2d_fid)
Repetition Time (*TR*)	220ms
Echo Time (TE)	105ms
Image matrix	128×128
FOV	120mm×120mm
Slice Thickness	5mm
Flip angle	90^o
Measurement	50

In the next step, the minimum magnetic field detectable by this method was calculated by mapping the simulated magnetic field on the experiment results.

To examine the effect of the microrobot's rotation on the proposed communication method, the coil was initially placed on the axial plane, and MR images were acquired while a current was applied. Then, the coil was rotated 90^o and MR images were taken while a current with the same frequency and amplitude was applied. Finally, the same procedure was repeated while the coil was positioned in the sagittal and in the arbitrary planes.

4.3 Results

4.3.1 Frequency detection

Figure 4-4 shows the simulated and experimental results when the coil was placed in the axial plane and an alternative electrical current with maximum amplitude of 1mA and frequency of 1Hz was applied.

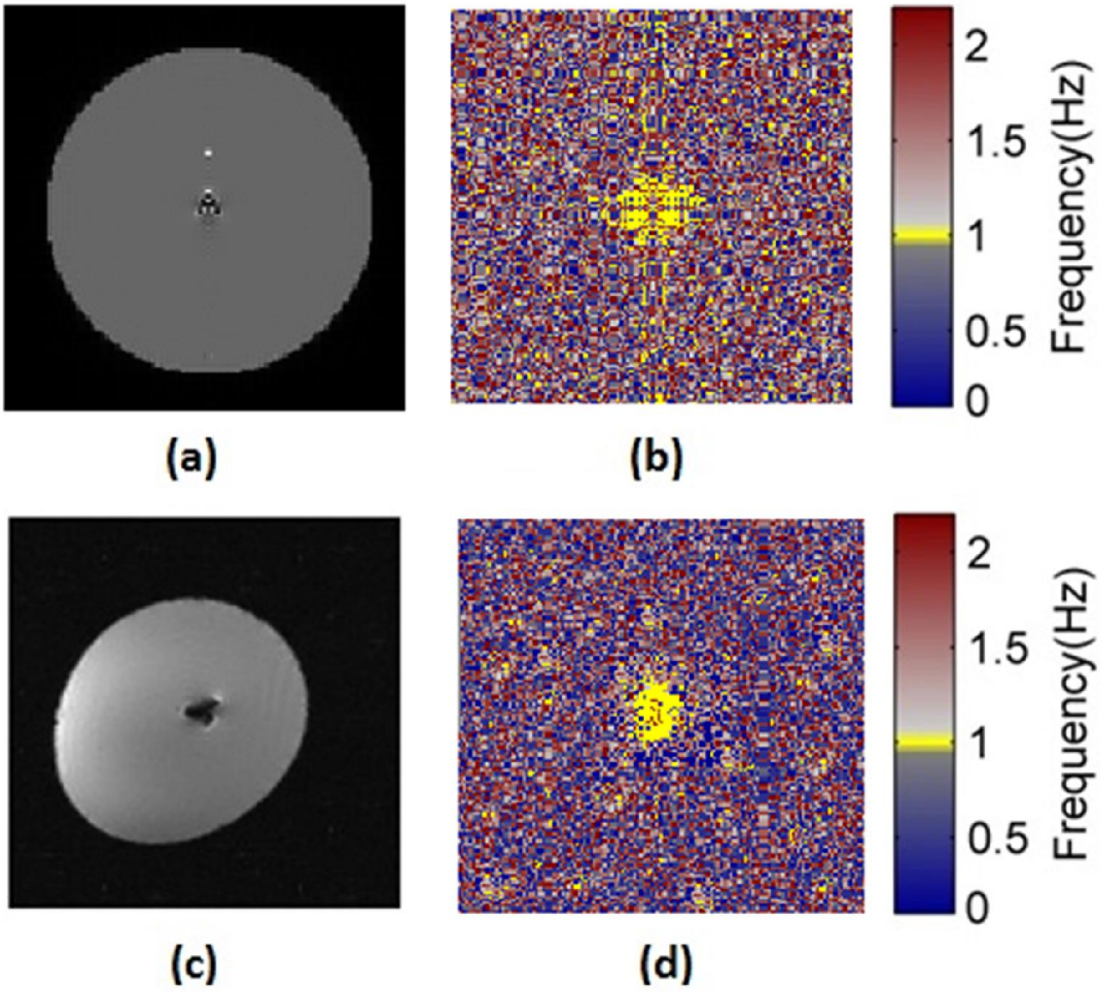

Figure 4-4: Detecting frequency using MRI. 1mA, 1Hz AC current was applied to the coil in axial plane. (a) Simulated MRI image (b) Simulated frequency map (c) Coronal single-shot EPI image of the coil (d) Experimental frequency map. The yellow pixels have a frequency of 1Hz which is equal to the applied current's frequency.

Figure 4-5 shows the results when the frequency was set to 0.5Hz. In these tests, a coronal image was taken as a plane perpendicular to the coil's surface. As shown in Figure 4-4 and Figure 4-5, the frequencies of applied current were successfully determined using MR images in both experiments. In the frequency maps, it is possible to identify a group of adjacent pixels with the same frequency. This frequency is equal to the frequency of the current applied to the coil. We refer to this group of adjacent pixels as the region of interest (ROI) in the rest of this chapter.

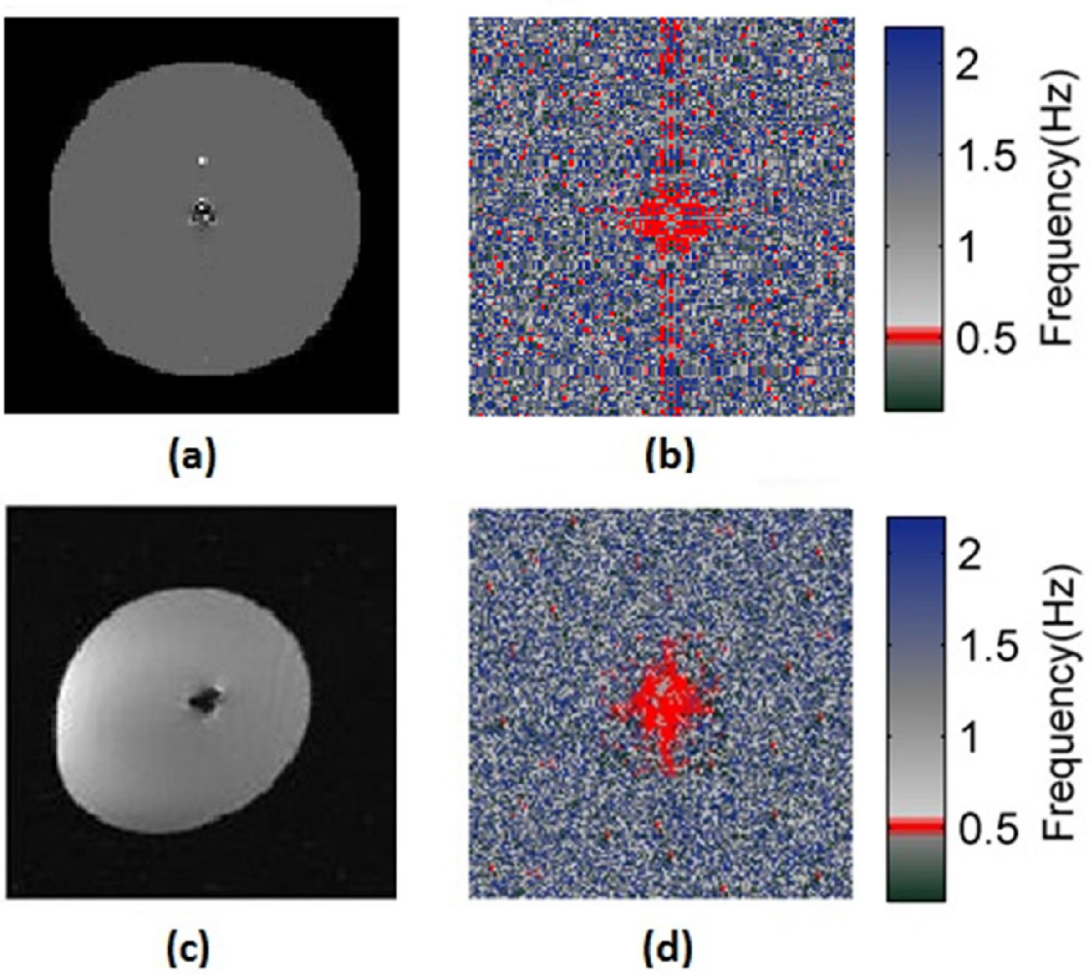

Figure 4-5: Detecting frequency using MRI. 1mA, 0.5Hz AC current was applied to the coil in axial plane. (a) Simulated magnetic field (b) Simulated frequency map (c) Coronal single-shot EPI image of the coil (d) Experimental frequency map. The red pixels have a frequency of 0.5Hz which is equal to the applied current's frequency.

Any arbitrary frequency under f_{max} was detectable with this method. Figure 4-6 shows the frequency maps of two sets of experiments with two different frequencies.

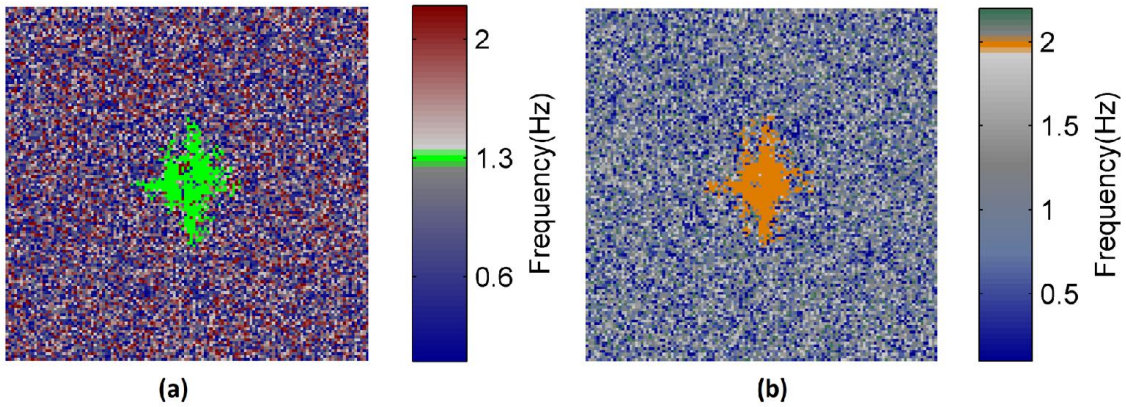

Figure 4-6: Detecting arbitrary frequencies using MRI. Frequency map resulting from an experiment set with 1mA and (a) 1.3Hz (b) 2Hz AC current.

4.3.2 Possibility of miniaturization

To investigate whether the MRI is sensitive enough to detect changes in the magnetic field of a miniature coil embedded in the microrobot, the minimum magnetic field detected in the above experiment was first calculated. Subsequently, the possibility of generating such a magnetic field using a miniature coil was shown. To calculate the minimum magnetic field, the magnetic field of the coil was simulated and mapped (as a contour) on the frequency maps acquired from MR images (Figure 4-7). The amount of magnetic field on the contour line at the edge of the ROI indicated the minimum magnetic field. As shown in Figure 4-7, a change in the magnetic field as small as 350pT is detectable using our proposed method.

We observed that, where the source of the frequency was noise, the number of adjacent pixels with the same frequency did not exceed five pixels. In addition, the areas indicative of the real frequencies included a minimum of 30 pixels. Therefore, in our first attempt to distinguish the real frequency from noise, only an area containing a minimum of 30 pixels was considered a ROI. Figure 4-8 shows the simulated magnetic field generated from a 70µA current passing through a double layer coil with an outer diameter of 350 µm in a plane perpendicular to its surface. Figure 4-8.b shows the simulated frequency map after considering the 350pT threshold. As shown in Figure 4-8.b, the ROI has more than 30 pixels, and as a result, the frequency of the

magnetic field produced by the microrobot with a miniaturized transmitter coil will be detectable by our proposed method.

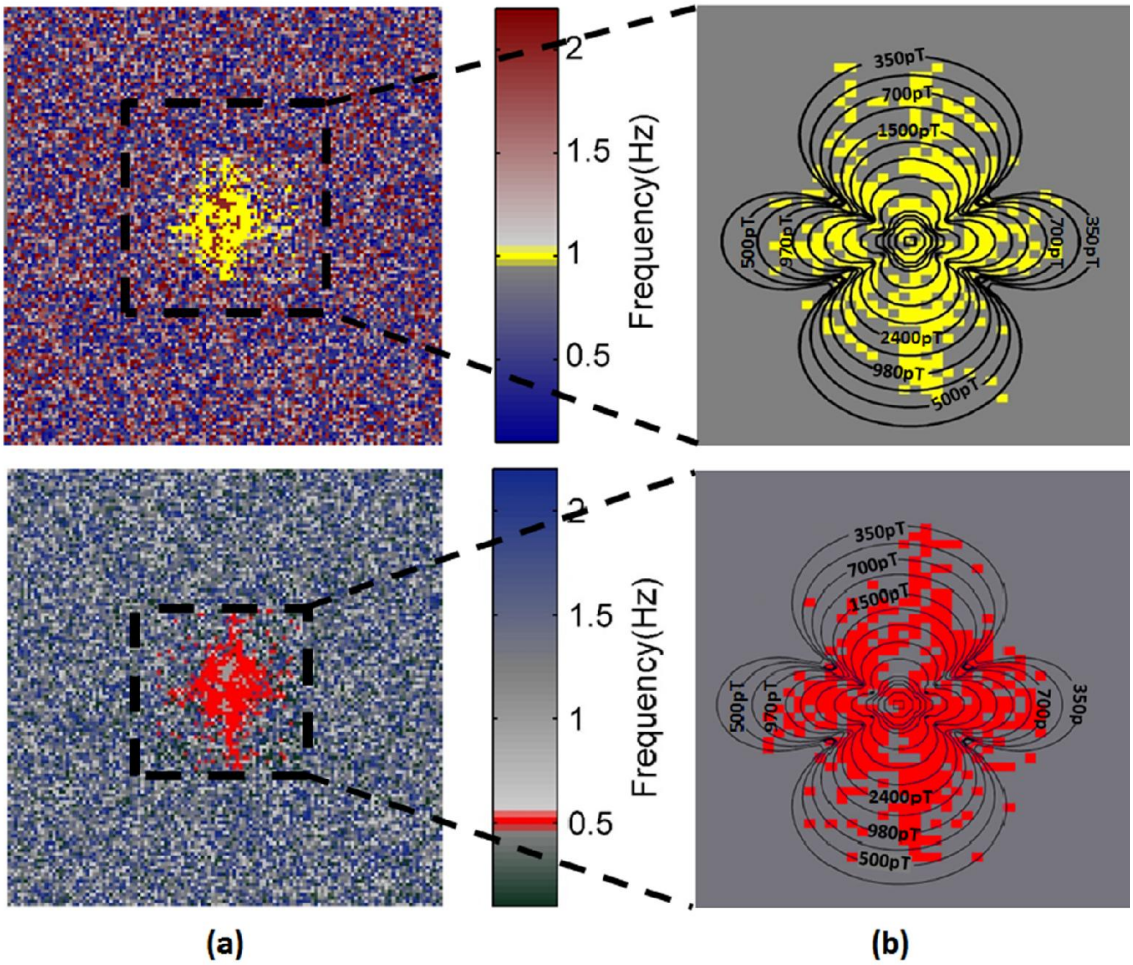

Figure 4-7: Detecting the minimum magnetic field by mapping the simulated magnetic field on the experiment field map. (a) Field map. The frequency in the ROI is 1Hz in the first and 0.5Hz in second row respectively. (b) For better visualization, a mask was applied to remove other frequencies on the field map. The area inside the dashed square is magnified. The change in the magnetic field as small as 350pT can be detected with our proposed method.

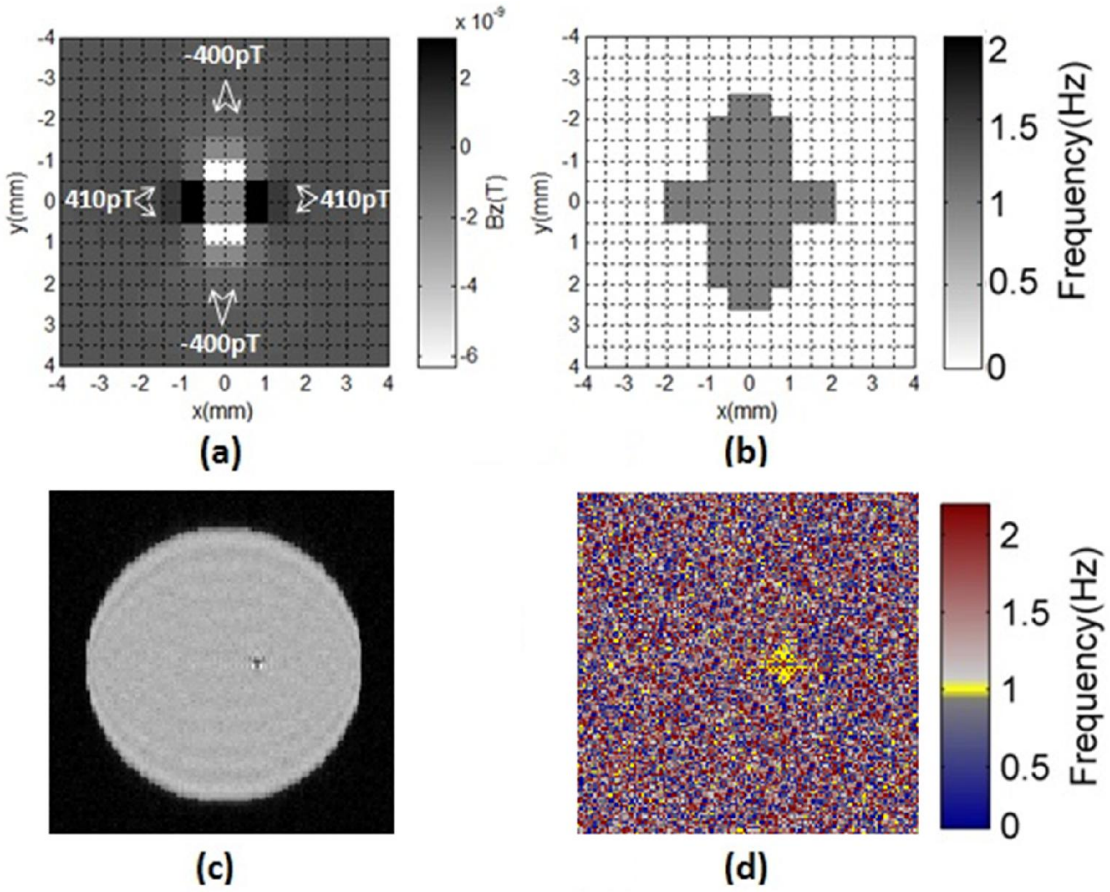

Figure 4-8: (a) Simulated magnetic field of a coil with an outer diameter of 350µm by applying 70µA current with f=1Hz. (b) Frequency map constructed from simulated magnetic field shows the frequency equal to the frequency of applied current. More than 30 pixels are affected by the magnetic field higher than 350pT. (c) Simulated MR image (d) Frequency map constructed from simulated MR image.

The second approach to distinguish the real frequency from noise is by means of standard deviation (SD). The experiment set was repeated several times and the frequency map was built for each set (Figure 4-9b). Then the SD of each pixel in the frequency maps was calculated. The pixels with the zero SD are the ones affected from coil's magnetic field because the frequency of other pixels affected by random noise varies at each set of experiment and as a result the SD of these pixels is non-zero (Figure 4-9c). Finally, the pixels in which the SD is non-zero are masked in frequency map. As shown in Figure 4-9d, the frequency of unmasked pixel is equal to the frequency of the microrobot. Comparing to the first approach, it is possible to detect frequencies of smaller coils with this method since only a few pixels is enough for detection. For instance, as

shown in Figure 4-9 it is possible to detect a frequency of a micro-coil with outer diameter of 156μm.

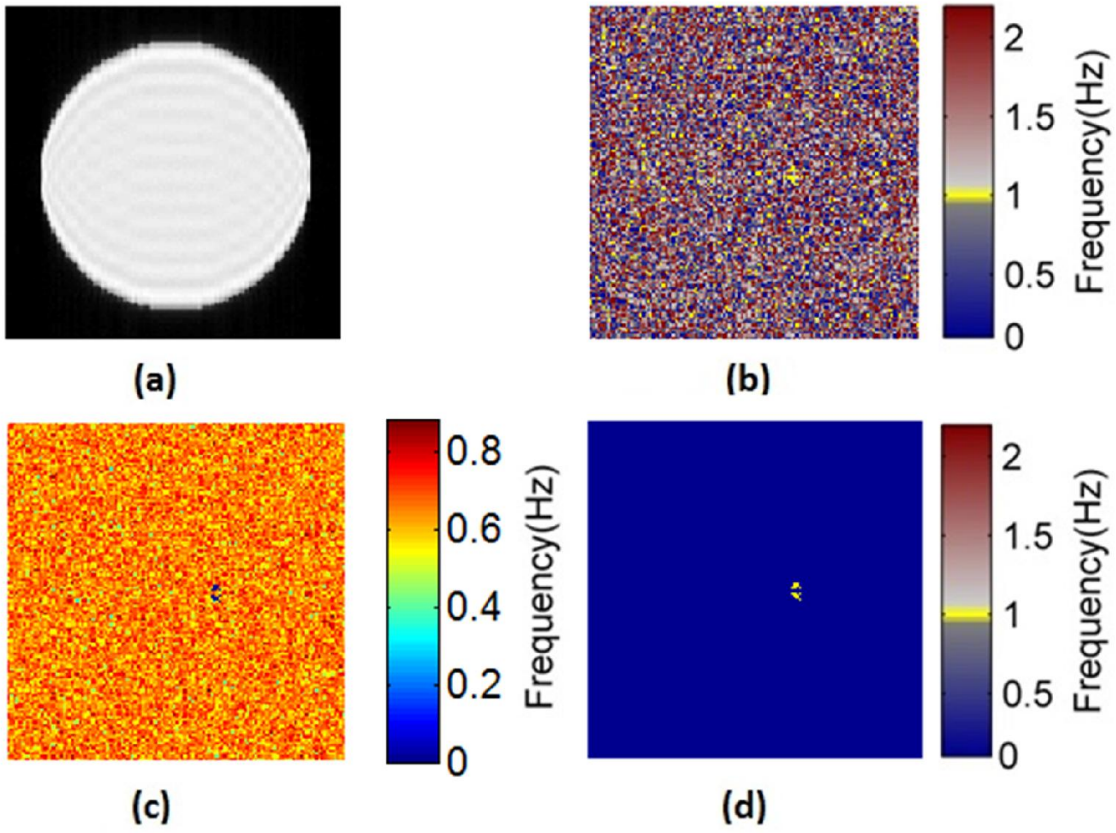

Figure 4-9: Localizing the micro-coil using standard deviation map. (a) Simulated MR image (b) Frequency Map (c) Standard deviation map of frequency change in each pixel after 20 repetitions. (d) Masking the frequency map using the standard deviation map. Frequencies with non-zero SD are masked. The specifications of the coil were: outer diameter = 156μm, inner diameter = 56μm, track width = 5μm, gap size = 5μm, number of turn = 5, current = 70μA

4.3.3 Rotation and displacement

As stated in Eq.(4-3), only a magnetic field parallel to B_0 affects MR signals. Hence, only the part of coil's magnetic field which is parallel to B_0 determines the magnetic field affecting the MR images. For instance, when the coil is in the axial plane, its B_z is parallel to the B_0 and appears in the MR image. Rotating the coil to the coronal plane (90^o rotation around the x-axis in Figure 4-3a) causes B_y to become parallel to B_0, and affects the MR images (Figure 4-10).

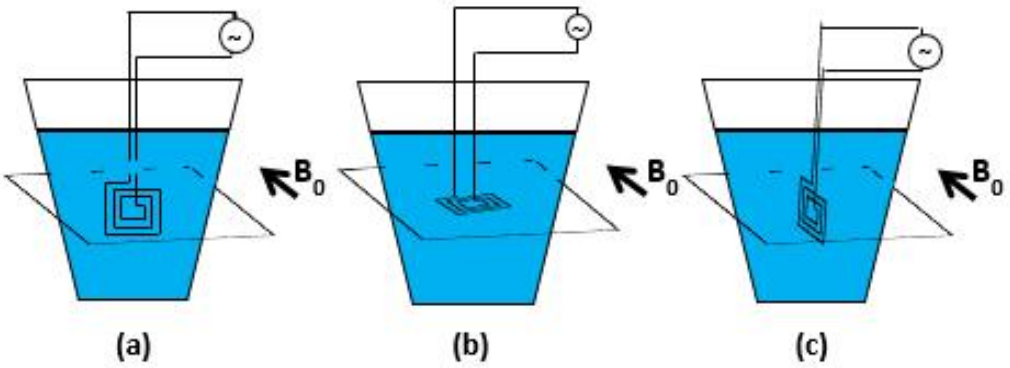

Figure 4-10: Coil in (a) Axial (b) Coronal (c) Sagittal plane.

Eqs. (3-2) and (3-3) show the relationship between the three magnetic field components and the current passing through the coil. Let us assume that an alternative current with amplitude A and frequency f, $I(t)=Asin(2\pi ft)$, will pass through the coil. As stated in Eqs. (3-2) and (3-3), the current has the same amplitude and frequency in all three components of magnetic field. Moreover, it is a scalar value, and thus independent of the coil's orientation and position. This implies that the frequency can be detected without initial information on the position of the microrobot. The detection of the frequency is also independent of any rotational movement. Figure 4-11 shows the frequency maps of the coil in axial, coronal, sagittal and an arbitrary plane while a 1mA current with two different frequencies passes through the coil. As shown in Figure 4-11, the frequency was correctly determined in all four configurations.

4.3.4 Effect of imaging parameters

There are several parameters available when setting up the imaging protocol. The parameters affect our proposed communication method through its effect on the susceptibility artifact and as a result the minimum detectable magnetic field. Therefore, the goal is to achieve highest signal to noise ratio (SNR) in the minimum scan time while having the largest susceptibility artifact.

4.3.4.1 Matrix size

Increasing the matrix size increases the resolution at the cost of SNR. Moreover, increasing the samples in frequency encoding direction lowers the susceptibility. On the other hand, in the phase-encoding direction, it increases the echo train length which leads to a larger artifact.

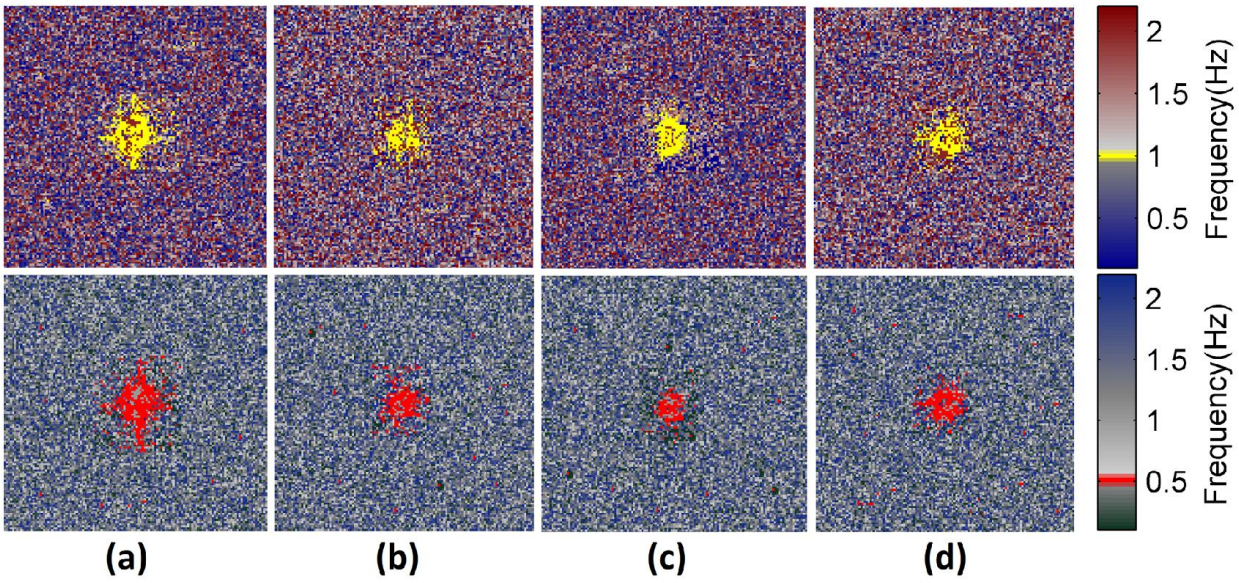

Figure 4-11: The effect of the rotation on the communication method. MR images were taken from the coil with current of I=1mA and a frequency of f = 1Hz, and a frequency map was built when the coil was placed in (a) axial, (b) sagittal, (c) coronal, and (d) arbitrary plane. The coil was in the middle of FOV, and the MR images were taken in a plane orthogonal to the coil's surface in all experiments. In the first row, an electrical current with the frequency of f=1Hz was applied to the coil, while in the second row, the frequency was set to f=0.5Hz.

Figure 4-12 shows the effect of halving the matrix size on frequency maps. The overall effect of the matrix size is negligible.

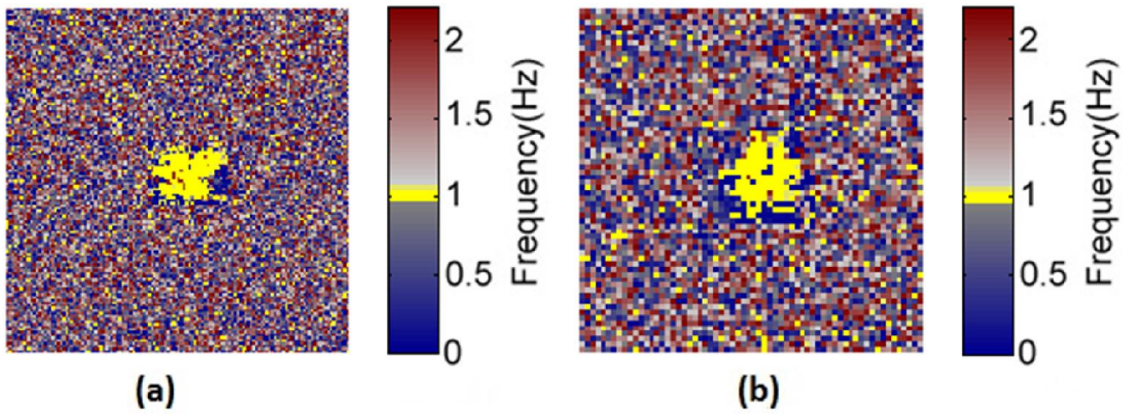

Figure 4-12: Effect of matrix size on the communication method. Frequency map was acquired from (a) 128×128 and (b) 64×64 images.

4.3.4.2 Time of Echo (*TE*)

As stated in Eq.(4-3), increasing *TE* increases the phase dispersion and results in a larger artifact. Figure 4-13 shows MR images and their frequency maps for two experiments with TE=50ms and TE =105ms.

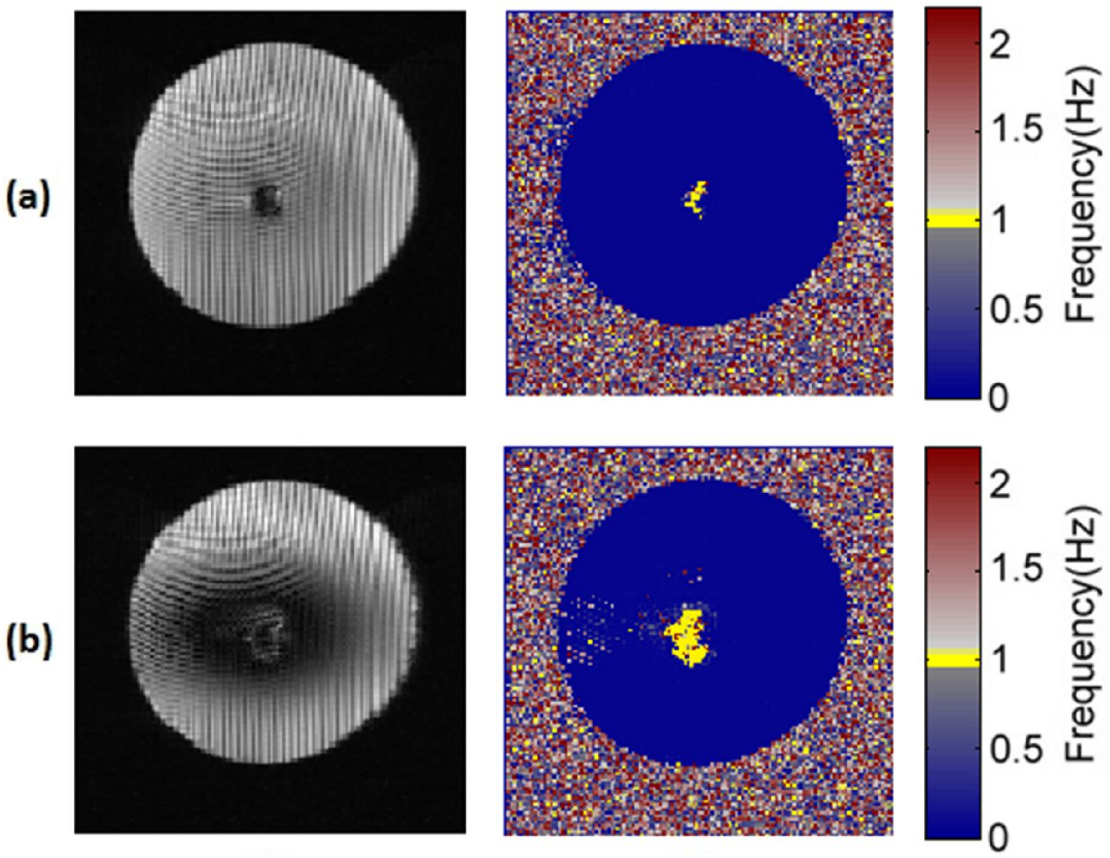

Figure 4-13: Effect of TE. Frequency map was acquired from MR images acquired with (a) TE=50ms and (b) TE=105ms

4.3.4.3 Repetition Time (TR)

In case of scan time and maximum detectable frequency, a smaller TR is desirable. However as mentioned in previous section it is desirable to set TE to its maximum value to increase the size of the artifact. Decreasing TR will limit the maximum TE allowable in the sequence.

4.3.4.4 Receiver Bandwidth (*rBW*)

The receiver bandwidth defines the range of frequencies that are sampled in the echo signal by the analog-digital-converter (ADC) during the application of the frequency gradient. It is calculated by:

$$rBW = \frac{1}{N_x . \Delta t} \tag{4-18}$$

where N_x is the number of samples in the frequency encoding direction and Δt is the ADC dwell time [100]. Note that Eq.(4-18) is the bandwidth per pixel, which is the number that appears on the Siemens scanner sequence parameter card. Total bandwidth across the entire image (which is used in GE scanners [101]) is defined as the reciprocal of the dwell time.

The *rBW* has an important role in determining the echo spacing (ESP) in EPI sequence [102]. Increasing the *rBW* shortens the *ESP* which leads to a smaller susceptibility artifact. However, the *SNR* decreases, since there is more noise being sampled relative to the received signal.

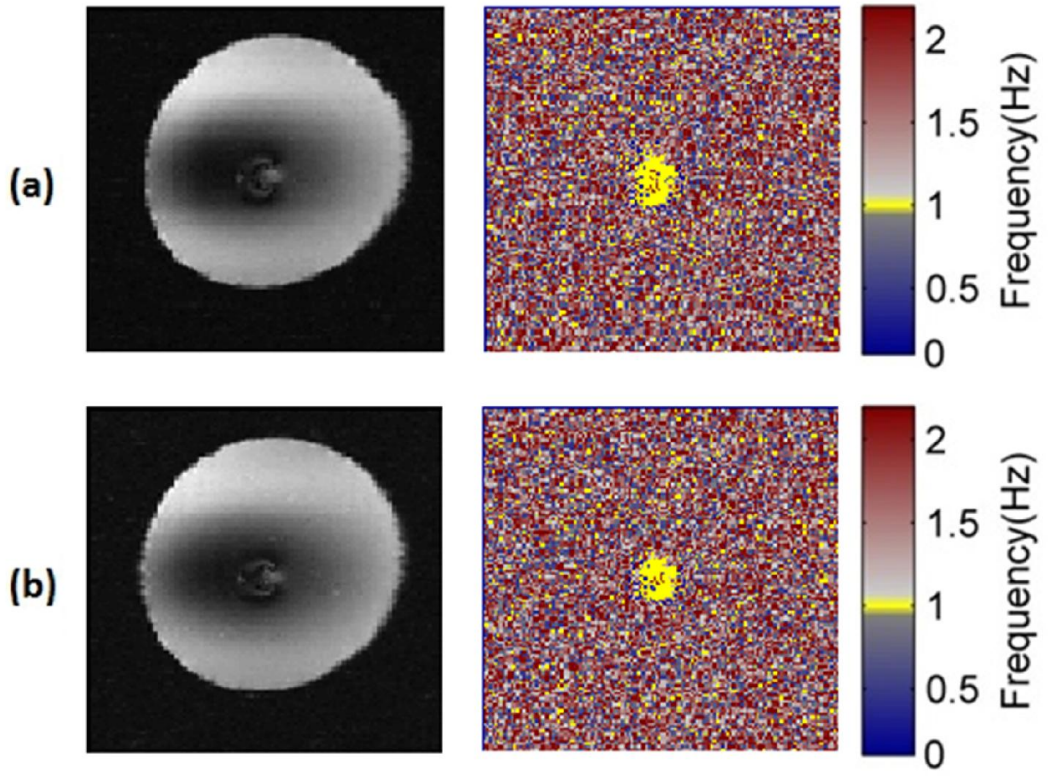

Figure 4-14: Effect of receiver bandwidth. Frequency map was acquired from MR images acquired with (a) rBW=1174Hz/px and (b) rBW=751Hz/px

4.3.4.5 Image acquisition and reconstruction method

The maximum frequency to be detected using this technique is limited by the minimum TR (Eq.(4-4)). Therefore, it is desirable to decrease the TR to expand the range of detectable frequencies.

In single-shot EPI imaging all phase encoding lines are acquired after a single RF excitation by employing series trains of bipolar readout gradients. Each line is phase-encoded separately by phase-encoding blips on the phase-encoding axis [94] (Figure 4-15). Reduction of the acquisition time in EPI sequences has been carried out by decreasing the echo train time by applying fast gradient. Echo-planar imaging employs gradient coils capable of a maximum amplitude of 20mT/m, a minimum rise time of 0.1ms, a slew rate of 200T/m per second, and a duty cycle of 50%–60% [94]. However, the switching rate is limited for safety consideration because fast-switching gradients induce a time-varying electric field that may cause peripheral nerve stimulation (PNS) at sufficiently high amplitudes [103-105].

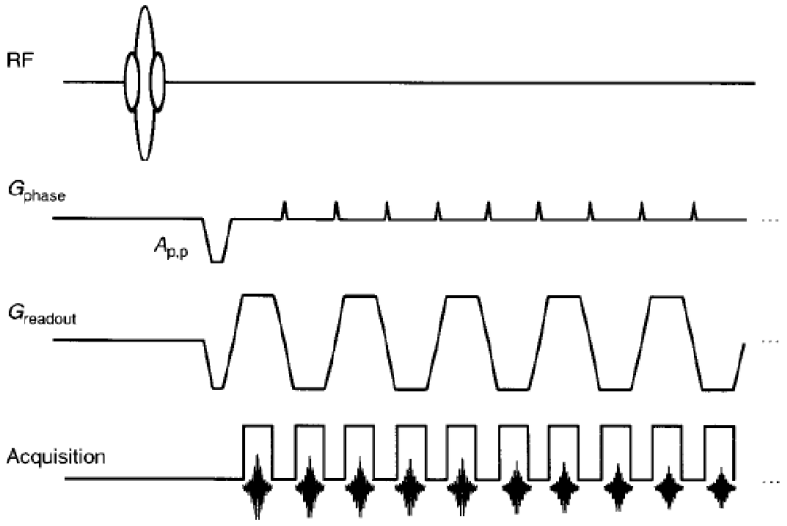

Figure 4-15: Echo-planar sequence (figure adapted from [38]).

Parallel imaging methods (pMRI) offer a decrease in acquisition time while maintaining the same resolution and signal to noise ratio (SNR). pMRI works by using the spatial sensitivity information of a multiple receiver surface-coil array to construct an image with only a fraction of phase-encoding steps [106]. The effect of the coil sensitivity is considered as an encoding effect similar to gradient encoding. Reduction in the phase encoding steps results in a reduction in the

field of view (FOV). This leads to aliasing effect which is irreversible if only one receiver coil is used. This problem is solved by a multiple-coil acquisition approach. Several pMRI reconstruction techniques and strategies have been proposed in the literature [107-111]. The techniques can roughly be classified in two main groups. In the first group the partial k space acquired from each coil is transformed to images and the final reconstruction happens in image space by combining the individual images using the coil sensitivity maps. PILS [109] and SENSE [112] are two examples in this group. In the second category, the reconstruction procedure happens in the k-space by calculating the missing k-space using the sensitivity information. (e.g. SMASH [107], GRAPPA [110]).

However, these techniques have a negative effect on our proposed communication method since they reduce the echo train length of the single-shot EPI sequence which leads to a reduction of the susceptibility artifact. Figure 4-16 shows the MR image and frequency maps of two sets of experiments acquired using GRAPPA technique and conventional full k-space acquisition.

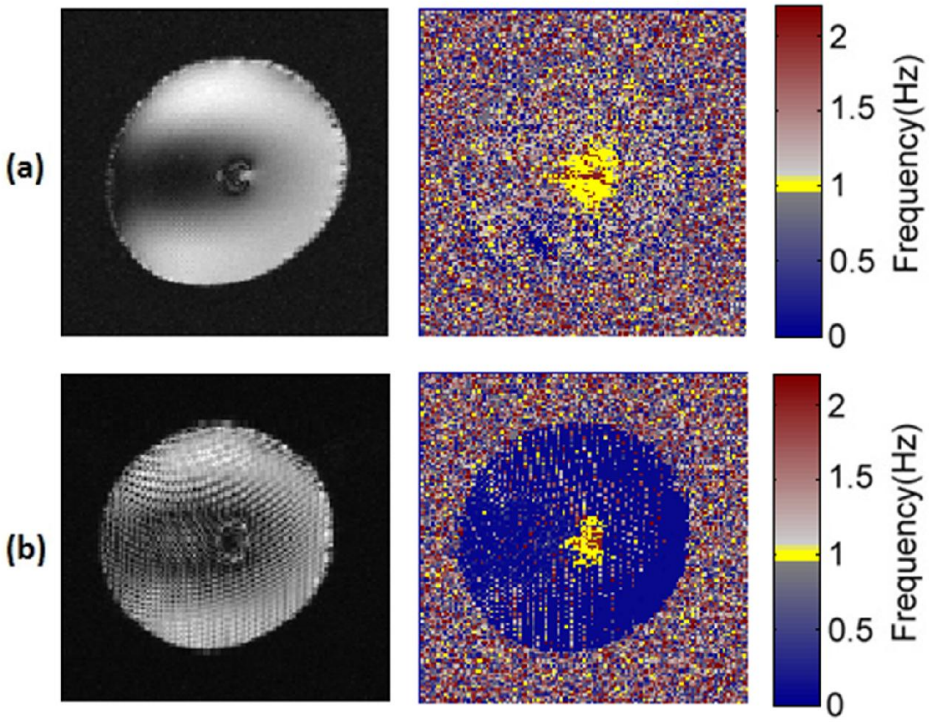

Figure 4-16 : Coronal single-shot EPI image and frequency maps of the coil for (a) conventional full k-space and (b) GRAPPA reconstruction. A 1mA, 1Hz AC current was applied to the coil in the axial plane. The yellow pixels have a frequency of 1Hz. The size of the coil's artifact is smaller in the GRRAPA image due to the reduction of the susceptibility artifact.

4.3.4.6 Parameters trade-offs

Table 4-2 summarizes the effect of the imaging parameters on our method. As shown in Table 4-2, there is a trade-off between parameters. For instance, Eq.(4-19) shows the relationship between the total acquisition time, rBW and matrix size.

$$TR = N_y(T_s + \Delta T) = N_x N_y \Delta t + N_y \Delta T \tag{4-19}$$

where $\Delta T \equiv 2\tau_{rt}$ is defined as the time needed to go from a peak to opposite peak in read gradient between echoes [113]. N_x is the total line in the read direction, N_y is total line in the phase direction and Δt is the sampling rate along read direction (ADC dwell time) [113] and it is related to rBW through Eq.(4-18).

Table 4-2: Parameters and their associated trade-offs

To optimize the communication method	Adjusted parameter	Consequence
Maximize the size of susceptibility artifact	↑ TE	↑ minimum TR ↓ SNR
	↓ receive bandwidth	↑ minimum TR ↑ SNR
Maximize SNR	↓ matrix size	↓ TR ↓ spatial resolution
	↓ TE	↓ susceptibility artifact
	↓ receive bandwidth	↑ minimum TR ↑ susceptibility artifact
Minimize TR	↓ matrix size	↑ SNR ↓ spatial resolution
	↑ receive bandwidth	↓ susceptibility artifact ↓ SNR

4.3.5 Localization and tracking

Due to the geometrical distortion in EPI images, this sequence cannot be used for exact positioning. Other sequences -such as gradient-echo- must be applied to locate and track the microrobot prior to the communication using the proposed EPI-based method. However, as we showed in Chapter 3, the minimum visible magnetic field in MR images is 50nT. Hence; as the magnetic field of the microrobot is smaller than this threshold, the microrobot is not visible in the MR images (Figure 4-9a) and only the frequency of its magnetic field is detectable.

Ferromagnetic materials have a high susceptibility. A magnetic field generated by a magnetic sphere (Figure 4-17) with constant susceptibility in a uniform magnetic field is calculated by [114]:

$$\vec{B}(\vec{r}) = B_0\hat{z} + \frac{\mu_0}{4\pi}\left(3\frac{(\vec{m}.\vec{r})\hat{r}}{r^5} - \frac{\vec{m}}{r^3}\right) \tag{4-20}$$

when $\hat{r}$ is the r-directional unit vector, $\hat{z}$ is the unit vector in z-direction, and $\vec{m}$ is the magnetic dipole moment calculated by:

$$\vec{m} = \frac{4}{3}\pi a^3 \vec{M}_{sat}\hat{z} \tag{4-21}$$

where a is the radius of the sphere and $\widehat{M}_{sat}$ corresponds to the saturation magnetization.

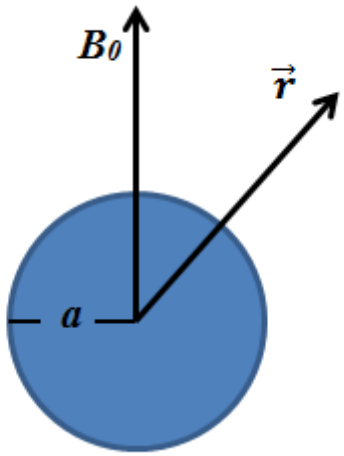

Figure 4-17: Schematic of a magnetic sphere with radius a in an external magnetic field B_0

Adding a ferromagnetic particle as a core to the transmitter coil raises the total magnetic field of the microrobot above the threshold of 50nT and therefore it becomes visible in the MR images (Figure 4-18).

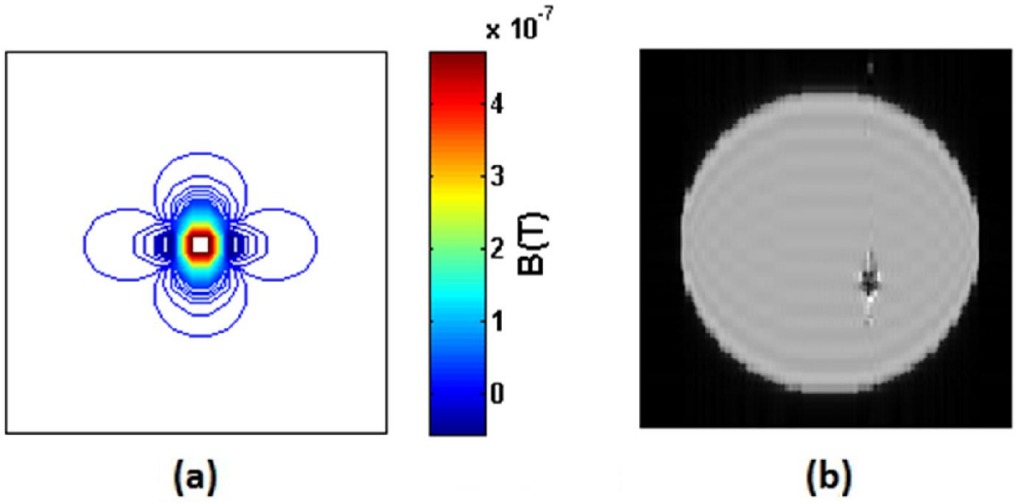

Figure 4-18: (a) simulated magnetic field of a 15μm ferromagnetic particle in 3T (b) simulated EPI-GRE MR image of the particle.

The magnetic core doesn't affect our communication method since its magnetic field is constant (Figure 4-19).

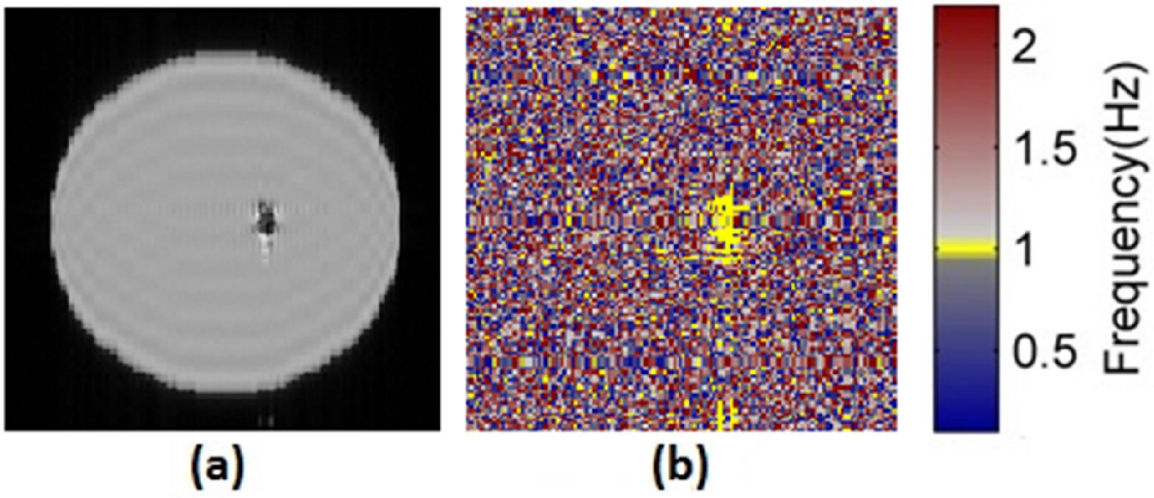

Figure 4-19: Micro-coil with ferromagnetic core (a) MR image (b) frequency map. The specifications of the coil were: outer diameter = 350μm, current = 70μA, ferromagnetic core's diameter = 15μm

4.3.6 Accuracy and frequency resolution

The frequency resolution of this method limits the accuracy of frequency measurement.

The frequency resolution, Δf, is defined as:

$$\Delta f = \frac{f_{\max}}{N} \tag{4-22}$$

where f_{max} is the maximum frequency defined by Eq.(4-4) and N is the number of images acquired in each set of experiments. For instance, using the sequence parameters in Table 4-1, the frequency resolution of the experiment is 45mHz. As shown in Figure 4-20, four frequencies with 50mHz steps can be successfully detected.

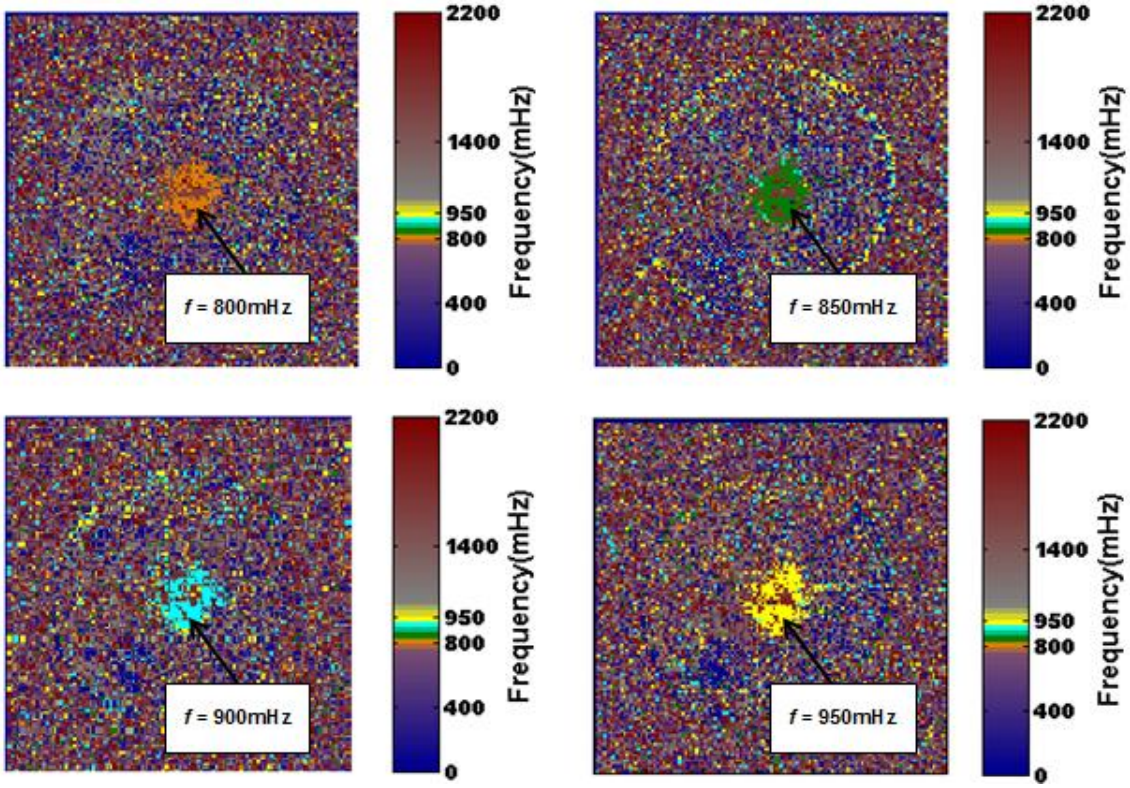

Figure 4-20 : Detecting four consecutive frequencies with 50mHz step.

4.3.7 Communication with several microrobots

Any arbitrary frequencies under the f_{max} are detectable with our proposed method. Hence; the communication can be expanded to communicate with more than one microrobot, or to obtain the

states of more than one sensor in a microrobot. For instance, Figure 4-21 the simulated MR images taken from two coils placed in arbitrary positions with different frequencies. As shown in Figure 4-21 two frequencies are detected separately and hence this method can be used to communicate with two or more than two microrobots at once.

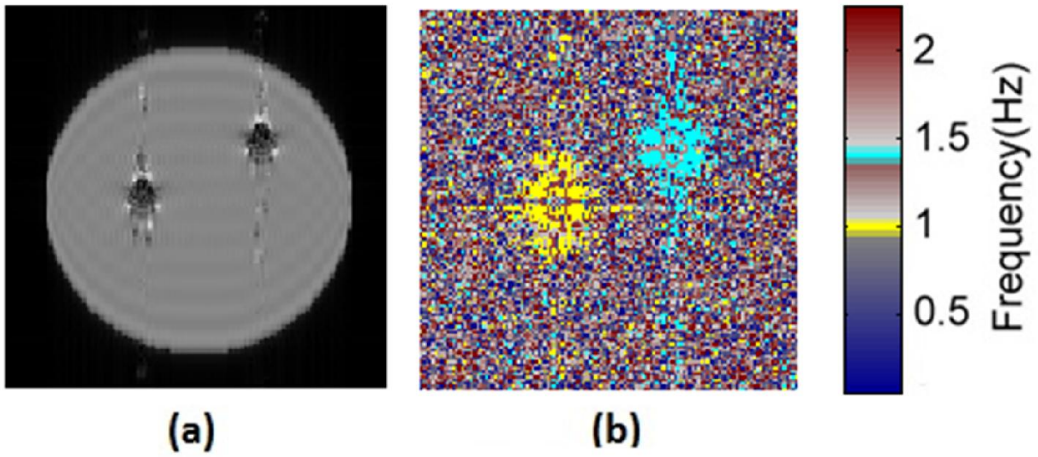

Figure 4-21: Communicating with several microrobots. (a) Simulated MR image of two coils in arbitrary positions with different frequencies (1Hz and 1.4Hz). (b) Two frequencies are successfully detected in the frequency map. The specifications of the coils were: outer diameter = 3mm, inner diameter = 1.4mm, track width = 200µm, gap size= 200µm, current = 1mA

Figure 4-22 shows the communication with two and five microrobot that were placed in arbitrary positions.

In cases where the magnetic fields of the coils overlap with each other, two peaks will appear in the frequency spectrum of each pixel. However only one of them appears in the frequency map as the algorithm selects the frequency of the absolute maximum in the spectrum. To distinguish between each coil, partial frequency maps were built for a specific frequency range (Figure 4-23).

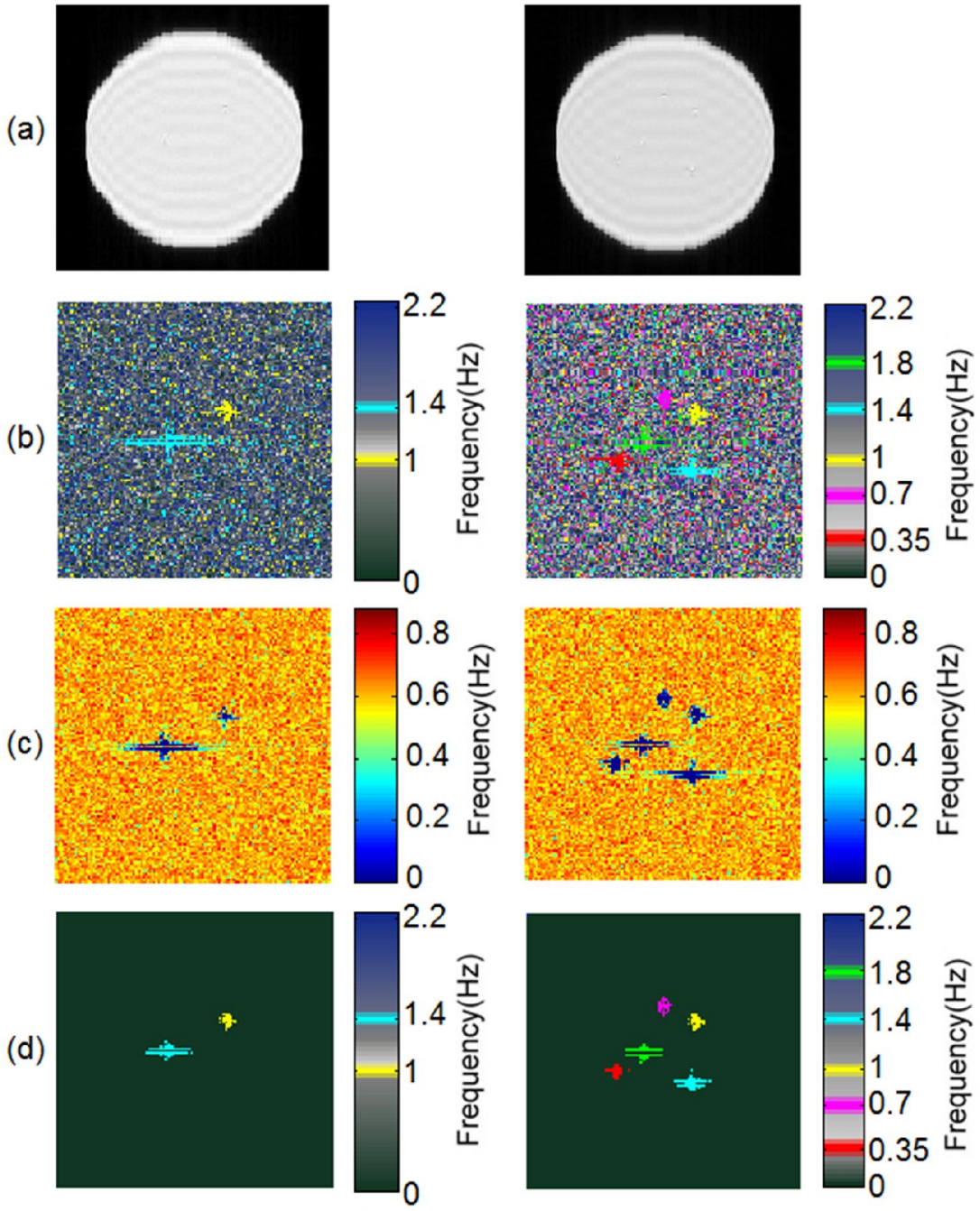

Figure 4-22: Communication with two (left column) and five (right column) microrobots in arbitrary positions with different frequencies. (a) Simulated MR images (b) Frequency maps (c) Standard deviation maps (d) Masked frequency maps. The specifications of the coils were: outer diameter = 350μm, current = 70μA, Frequencies= (a)1 and 1.30Hz (b) 0.3, 0.75, 1,1.4 and 1.8Hz

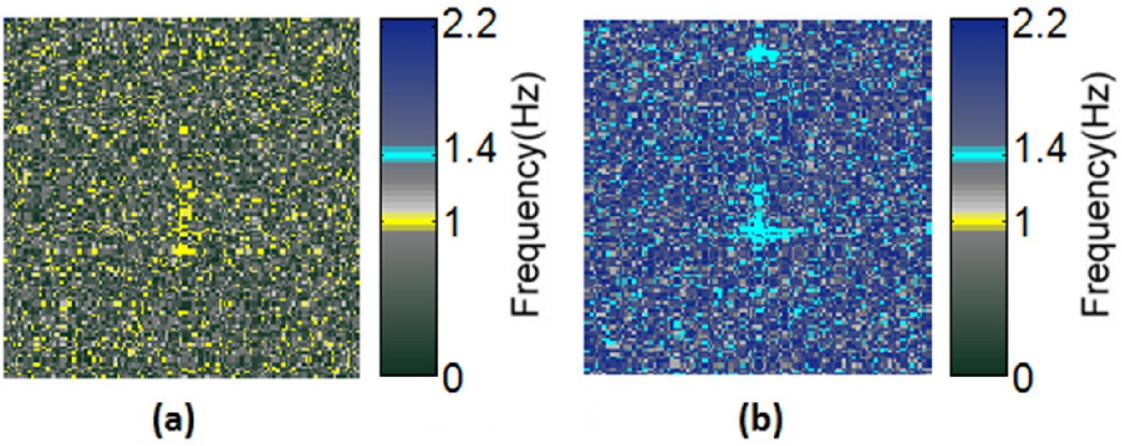

Figure 4-23: Communicating with two microrobots with overlap. The first microrobot uses frequencies between 0 and 1.2Hz while the second microrobot communicates with frequencies between 1.2Hz and 2.25Hz. Simulated partial frequency maps were made based on these ranges. The specifications of the coils were: outer diameter = 350μm, current = 70μA, frequency (a) 1Hz (b) 1.4Hz.

This method might also be used for measuring a parameter instead of binary communication. For example, each pH level can be mapped onto a specific frequency. The accuracy the of measurement is limited by the maximum detectable frequency and frequency resolution

4.4 Conclusion

In this chapter, the basis for a new approach in communication for an untethered intelligent medical microrobot was introduced and demonstrated. In the proposed method, the frequency of the current circulating through a miniature planar coil embedded in the microrobot was designed to change relatively to the sensory input level. The AC current produces AC magnetic field inhomogeneity, which is detectable in MR images independent of the microrobot's orientation. The minimum magnetic field detectable by this method is decreased to 350pT compared to 50nT in Chapter 3. This allows us to achieve a higher level of miniaturization where the power source, and consequently, the generated magnetic field would be very limited. Moreover, the ability to detect several frequencies makes it possible to use the binary communication method for more than one sensor on the microrobot, or to use several microrobots by associating each sensor or microrobot to two specific frequencies which differ from the others.

CHAPTER 5 FREQUENCY BASED COMMUNICATION USING T1ρ IMAGING

In Chapter 4, we proposed a communication method based on detecting the frequency of the magnetic field generated by the microrobot using EPI imaging. We showed that the maximum detectable frequency by this method is limited by the minimum TR. Reduction of the TR in EPI sequences can be carried out by employing the fast switching gradient and parallel imaging methods. However, the switching gradient rate is limited because of safety considerations, and we showed that using parallel imaging technique such as GRAPPA decreases the sensitivity of our method. Moreover, decreasing TR leads to a decrease in TE which has negative impact on the communication.

In this chapter, we investigated the feasibility of using T1ρ imaging technique to detect higher range of frequencies. We showed that it is possible to detect the frequency of the microrobot's magnetic field using a spin-lock module independent of microrobot position and orientation.

The rest of this chapter is organized as follows: Section 5.1 covers a theoretical background underlying T1ρ imaging technique (spin-lock). Section 5.2 describes the methodology and simulation framework to test the proposed communication system. Results are presented in Section 5.3, followed by the discussion and conclusion in Sections 5.4 and 5.5 respectively.

5.1 Theoretical background

To understand the spin-lock, we need to explain the rotating frame of reference. As explained earlier, the external magnetic field causes a rotation of the magnetic moment about the field. In case of a static external field (B_0), the rotation is a constant precession about B_0. Suppose that we look at the magnetization in a reference frame rotating clockwise at the Larmor frequency around the z-axis of the laboratory reference frame and the static field is pointing in the positive z-direction. The spin axis does not move at all from this point of view. This reference frame is called the rotating reference frame and is useful to simplify the mathematical framework governing the NMR phenomenon [92]. In this frame: The effect of the B_0 has disappeared; The RF field (B_1) appears static since it is rotating with the same frequency; and Magnetization has begun a new precession around B_1. Since B_0 no longer exists in this frame of reference, the only magnetic field acting on M is the now stationary B_1 field. Therefore, M will precess around B_1

with frequency $\omega_1 = \gamma B_1$. Figure 5-1 shows a comparison of magnetization behavior in the laboratory and rotating reference frames.

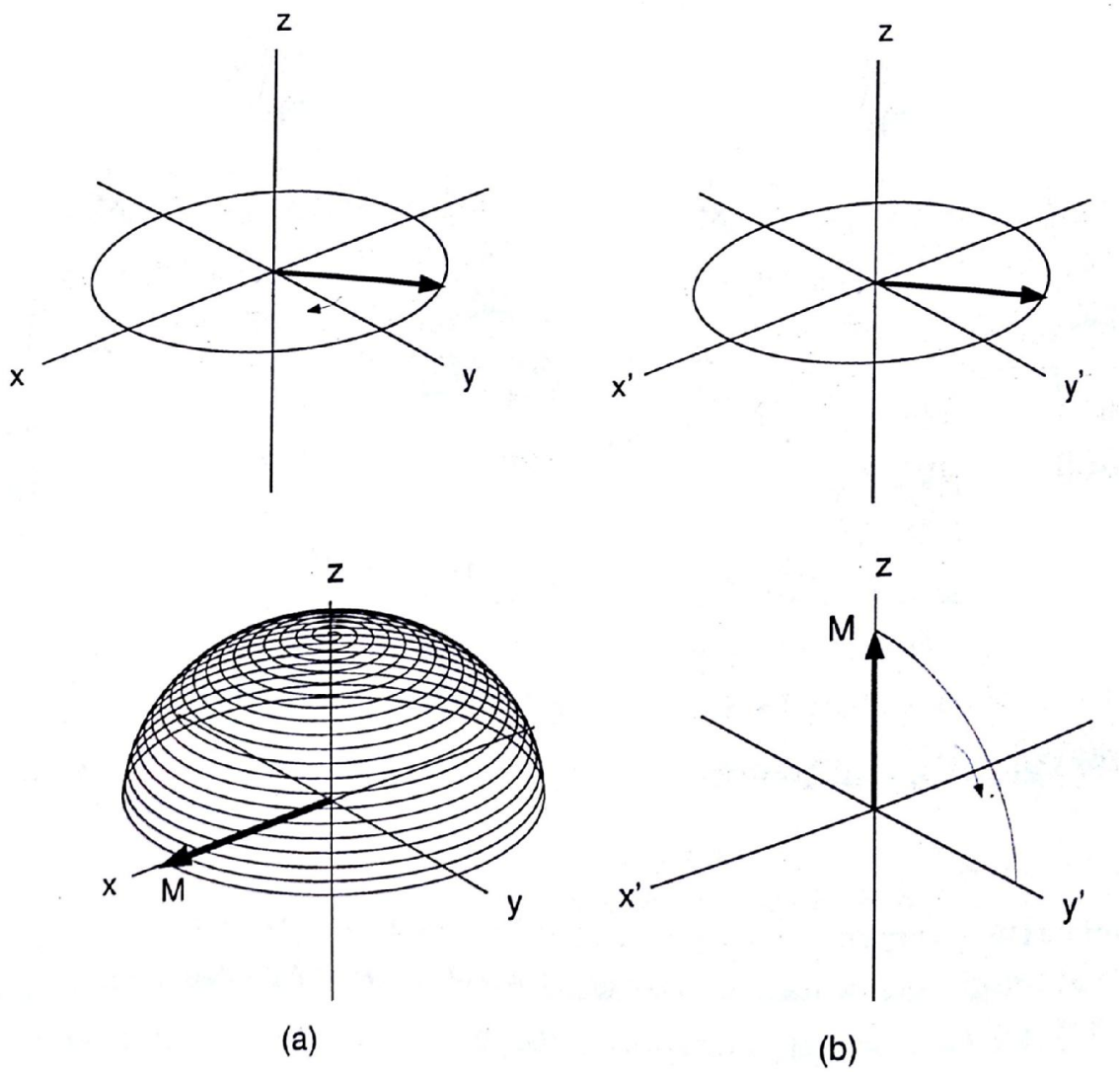

Figure 5-1: Comparison of magnetization behavior in (a) laboratory and (b) rotating reference frames [115].

Now assume that a RF excitation pulse is applied and the magnetization is aligned to *y*-axis. If all of the spins precess at Larmor frequency, the magnetization remains aligned to *y*-axis. However, slight variation in the Larmor frequency arises from different sources which lead to T_2 decay. In the rotating reference frame, this will appear as spin spreading away from *y* in both the positive and negative directions, and the net magnetization will shrink along the *y*-axis. Applying a continuous RF pulse called spin-lock pulse at resonance with the Larmor frequency along the *y*-

axis, it will appear as a static magnetic field along the *y*-axis in the rotating reference frame. Similar to the Larmor precession about the static magnetic field, all the magnetization will be pulled into precession around the spin-lock field with the frequency equal to $\omega_{sl}=\gamma B_{sl}$, and the spins undergo a new relaxation which is characterized by $T_{1\rho}$ relaxation constant. In this situation, the oscillating magnetic field generated by the microrobot (ΔB_m) can act as the RF pulse and tip the magnetization away from the *y*-axis if its frequency is at resonance with spin-lock frequency. The magnetization behavior during the spin-lock $M_{sl} = [M_x, M_y, M_z]^T$ can be expressed by the Bloch equation. Considering a doubly rotating reference frame (it rotates along *y*-axis in the rotating reference frame with spin-lock frequency ω_{sl}) and renaming the axis *x* to *y*, *y* to *z*, and *z* to *x* we have [116]:

$$\begin{aligned}
\frac{dM_x}{dt} &= -\frac{M_x}{T_2^*} + (\omega_{sl} - \omega_{ac})M_y \\
\frac{dM_y}{dt} &= (-\omega_{sl} - \omega_{ac})M_x - \frac{M_y}{T_2^*} + \omega_m M_z \\
\frac{dM_z}{dt} &= -\omega_m M_y - \frac{M_z - M_0}{T_{1\rho}}
\end{aligned} \tag{5-1}$$

where $\omega_m=\gamma\Delta B_m$. ΔB_m and ω_{ac} are the amplitude and the frequency of the oscillating magnetic field.

The spin-lock module combined with application of microrobot's oscillating magnetic field and an imaging sequence and its effect on magnetization is shown in Figure 5-2. First, the magnetization is flipped into the transverse plane along the *y*-axis by applying a 90° RF pulse along the *x*-axis. Then the magnetization is locked along the y-axis by applying the spin-lock pulse along the same axis. After a time T_{sl} the spin-lock field is switched off and the magnetization is restored to its original direction along the *z*-axis in preparation for the imaging sequence. As shown in Figure 5-2c1, applying ΔB_m perpendicular to the spin-lock field tips away the magnetization from the transverse plane which leads to a decrease in the restored magnetization after applying the second 90° pulse.

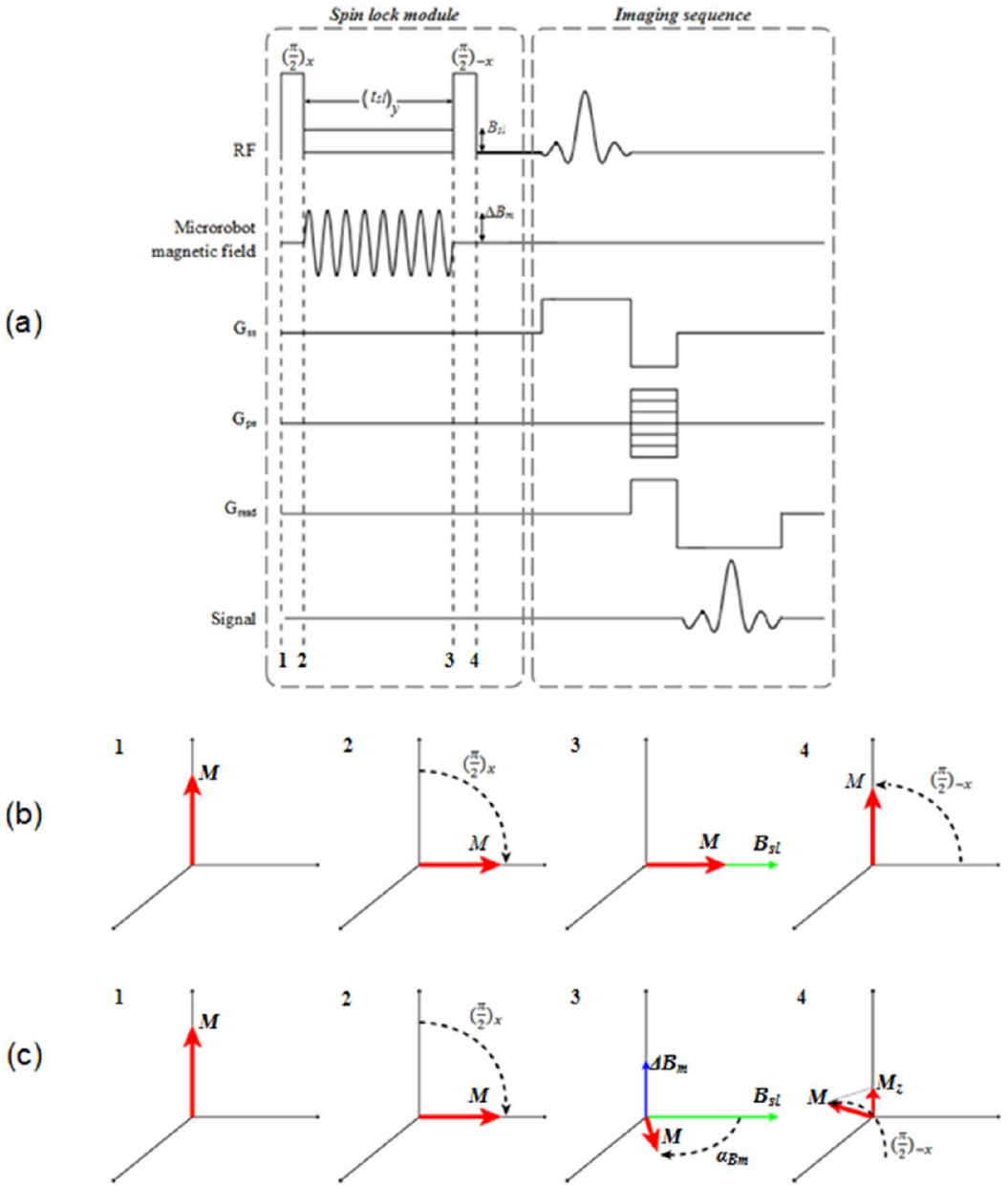

Figure 5-2: A conventional imaging sequence combined with spin-lock module and microrobot magnetic field. (a) Sequence diagram. (b) Magnetization behavior in the absence of the microrobot magnetic field (c) Magnetization behavior in the presence of the microrobot magnetic field. The initial magnetization along with B_0 (1) is flipped into the transverse plane by a 90° pulse (2) and is locked on *y*-axis (3). Finally the magnetization is restored by a second 90° pulse (4) in preparation for the imaging sequence. The presence of the microrobot magnetic field causes the magnetization to tip away from *y*-axis (c.3) and as a result, the restored magnetization is smaller than its initial value (c.4).

5.2 Material and method

5.2.1 Magnetization behavior

The magnetization during spin-lock was calculated from Eq.(5-1) by means of a matrix operation [117]. Then it was transform to rotating reference frame by:

$$M_{rot} = Rot_z(\omega_{ac}t)M_{sl} \tag{5-2}$$

where Rot_z is the rotation matrix around z-axis as defined in Eq.(4-8).

Finally, after renaming the axis x to z, y to x, and z to y the magnetization in laboratory reference frame was calculated from Eq.(5-3):

$$M_{lab} = Rot_z(\omega_1 t)M_{rot} \tag{5-3}$$

where ω_1 is the frequency of the RF excitation pulse and it is equal to the Larmor frequency.

5.2.2 Frequency detection

To detect the frequency of the microrobot magnetic field ΔB_m (ω_{ac}), the magnetization was flipped into the transverse plane using 90^o pulse and then locked by a spin-lock pulse along the y-axis. Then the signal was recorded after the spin-lock period T_{sl}. The experiment was repeated with different spin-lock fields and the magnitude of M_y at the end of the spin-lock period was calculated for each spin-lock frequency.

To show the sensitivity of the method to external AC fields, the experiment was conducted for different arbitrary frequencies. The amplitude of the microrobot field was set to ΔB_m = 200nT and the relaxation constants were T_1 =1100ms, T_2^*=75ms and $T_{1\rho}$=100ms.

Next, the influence of ΔB_m and duration of spin-lock pulse on signal decrease was investigated.

5.3 Results

5.3.1 Magnetization behavior

Figure 5-3 shows the magnetization behavior during the spin-lock module in the absence and presence of the microrobot AC magnetic field. As shown in Figure 5-3a.3, in the absence of the microrobot AC field, the magnetization stays in the transverse plane and was only decreased due to the $T_{1\rho}$ effect. However, it oscillates along z-axis and there is an additional decrease in the final magnetization due the presence of the microrobot AC field.

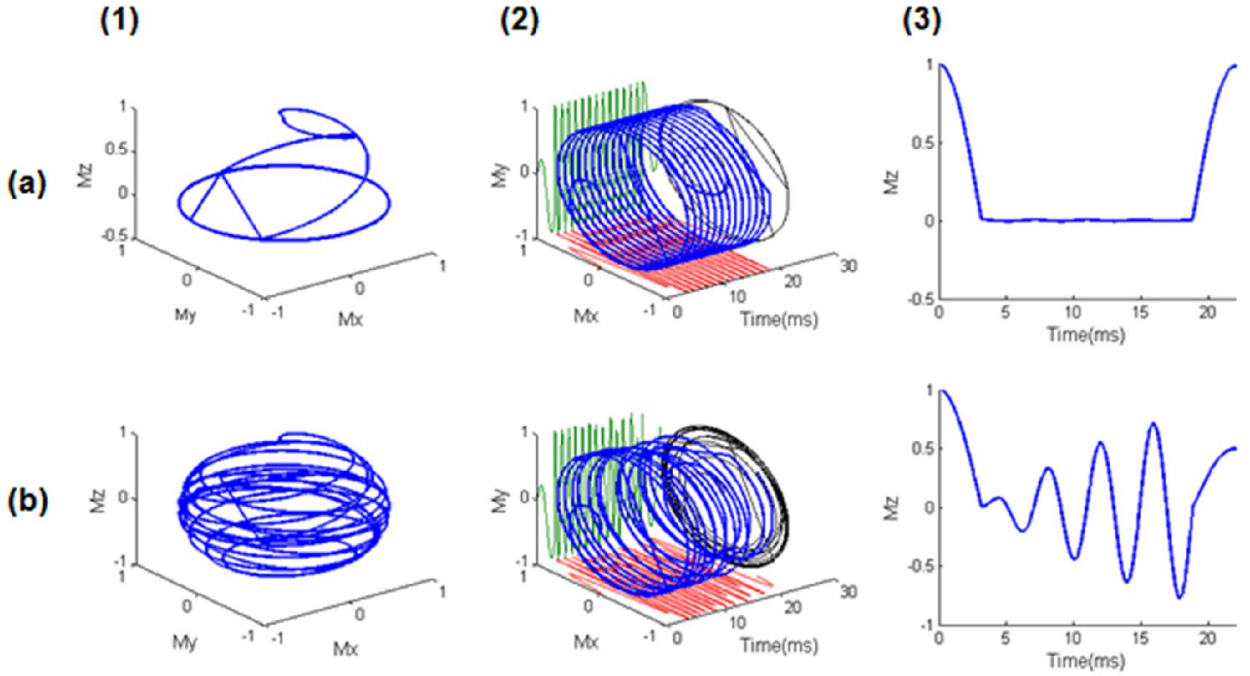

Figure 5-3: Magnetization behavior in laboratory reference frame during the spin-lock module in the absence (a) and in the presence (b) of the microrobot AC field. (1) Magnetization behavior in 3D format. (2) Evolving transverse magnetization during the spin-lock module. (3) Evolving longitudinal magnetization during the spin-lock module. M_z is flipped onto the transverse plane within 1ms by applying the 90^o RF pulse. It will oscillate during spin-lock around the z-axis because of the AC magnetic field. Finally, it turned back to the z-axis by applying the second RF pulse in the last 1ms. There is a decrease in the M_z because of the microrobot AC field.

5.3.2 Frequency detection

Figure 5-4 shows the magnitude of y-magnetization after the spin-lock period for different spin-lock frequencies. It clearly indicates the point of maximum resonance at 200Hz and 320Hz and displays ~20 Hz width at half.

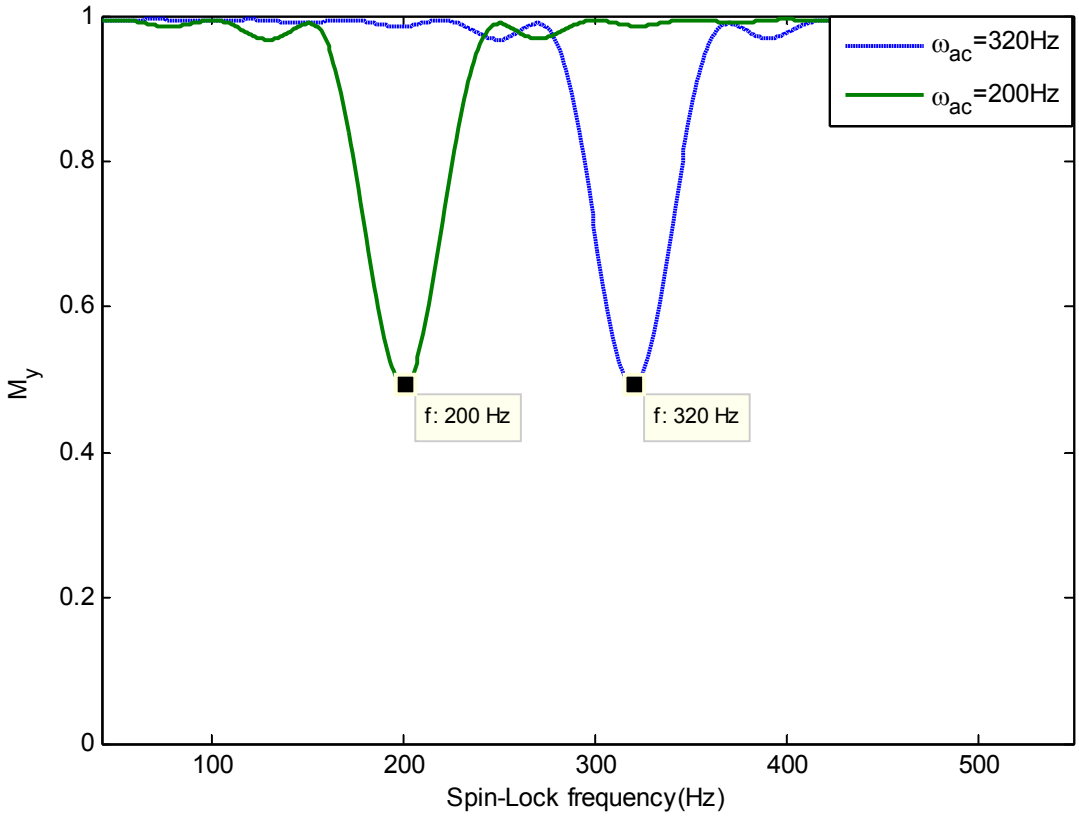

Figure 5-4: Magnetization versus spin-lock frequency. The decrease in the magnetization is maximized when the spin-lock frequency (ω_{sl}) and microrobot AC field (ω_{ac}) are at resonance: 200Hz and 320Hz. The half width at half maximum (HWHM) is approximately 20Hz. The simulation parameters were: T_{sl} = 20ms, $T1\rho$=100ms, T2=100ms, T1=1100ms.

5.3.3 Possibility of miniaturization

Miniaturizing the microrobot affects the communication method through a decrease in the microrobot magnetic field. As mentioned earlier, the magnetic field of the microrobot acts as a RF excitation pulse during the spin-lock and tips the magnetization away from *y*-axis. The flip angle is calculated by:

$$\alpha_m = \gamma \Delta B_m T_{sl} \tag{5-4}$$

Decreasing ΔB_m as a result of microrobot miniaturization leads to a smaller flip angle and hence, to less decrease in the amount of MR signal. Figure 5-5 shows the y-magnetization at the end of the spin-lock period during a sweep of the spin-lock frequency across resonance with ω_{ac} for two amount of ΔB_m.

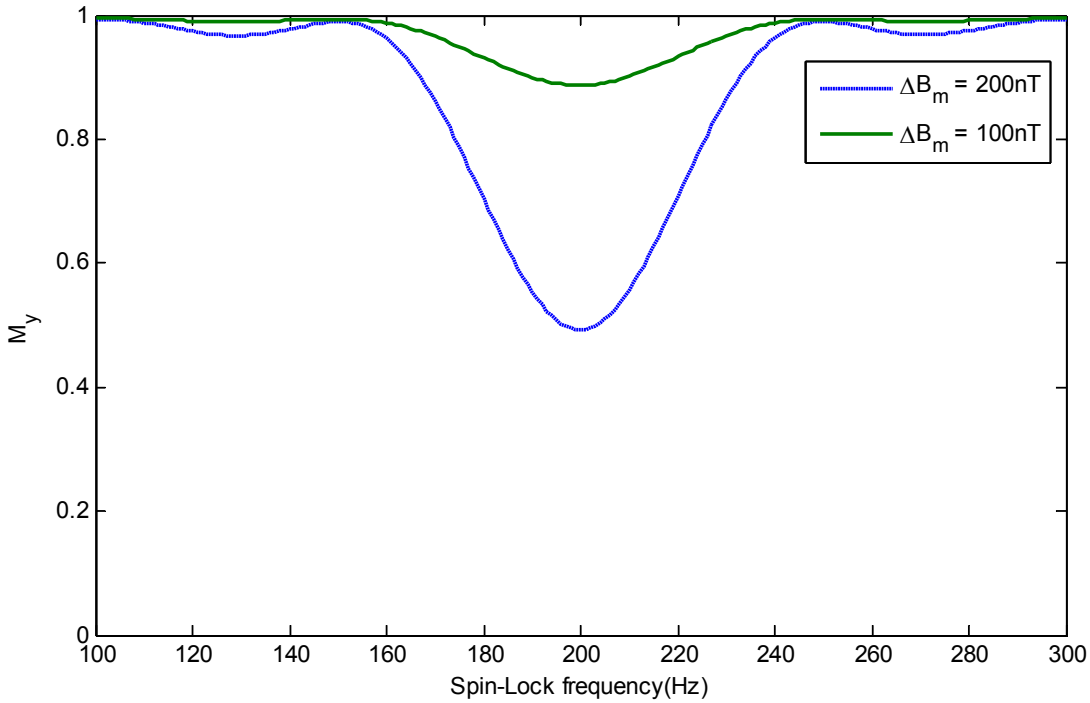

Figure 5-5: Effect of the AC magnetic field. Increasing ΔB_m leads to larger flip angle and greater signal reduction. Simulation parameters were: T_{sl} = 20ms, $T1\rho$=100ms,T2=100ms,T1=1100ms.

Figure 5-6shows the amount of y-magnetization and the flip angle versus different amount of ΔB_m with constant T_{sl}. As shown in Figure 5-6, the magnetization reaches to when the flip angle reaches to 90° or 270°. And it is at its maximum value when α_{sl} = 0° and 360°.

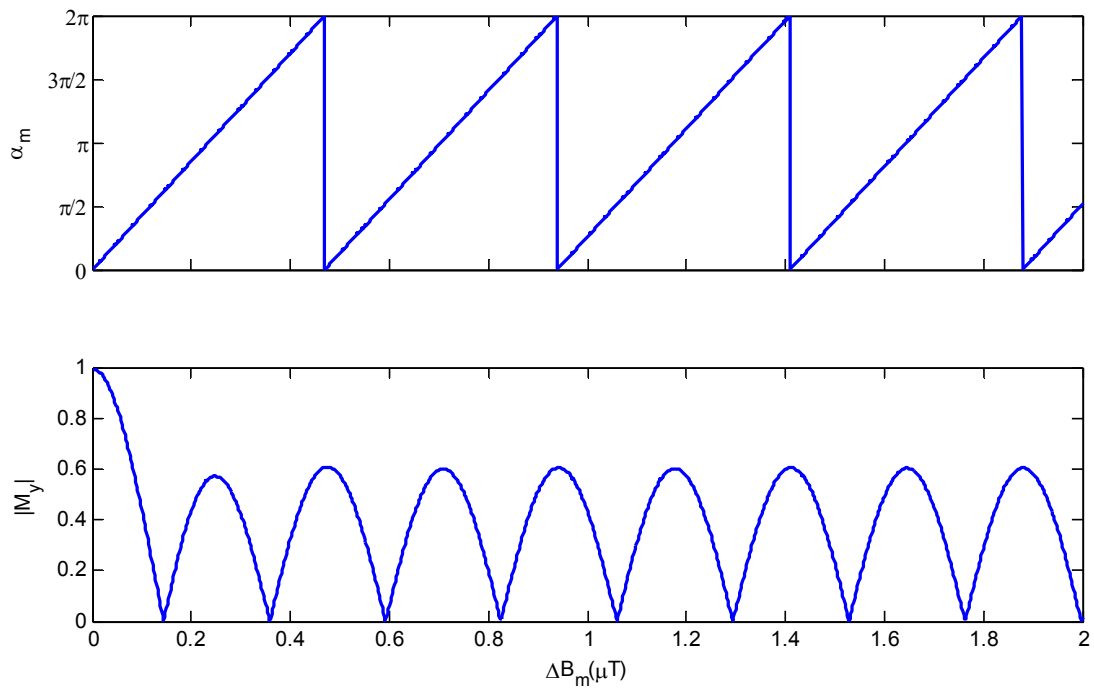

Figure 5-6: Effect of the AC magnetic field. Increasing ΔB_m leads to a larger flip angle. First maximum reduction happens at α_m=90° where there is no magnetization left along the *y*-axis. A greater field causes the magnetization to return to its initial position after a 360° rotation. Simulation parameters were: T_{sl} = 50ms, $T1\rho$=100ms, $T2$=100ms, $T1$=1100ms, ω_{sl} = 100Hz, ω_{ac} = 100Hz.

As stated in Eq.(5-4), the flip angle is also affected by the duration of the spin-lock pulse. Hence; in case of a very small magnetic field, the spinlock time can be increased to acquire the desired flip angle. The spin-lock time is limited by the relaxation times, $T1\rho$ and $T2$. Figure 5-7 shows the effect of T_{sl} on magnetization.

Therefore, to maximize the reduction, the spin-lock duration must be decreased for a specific amount of ΔB_m if the flip angle is larger than 90°.

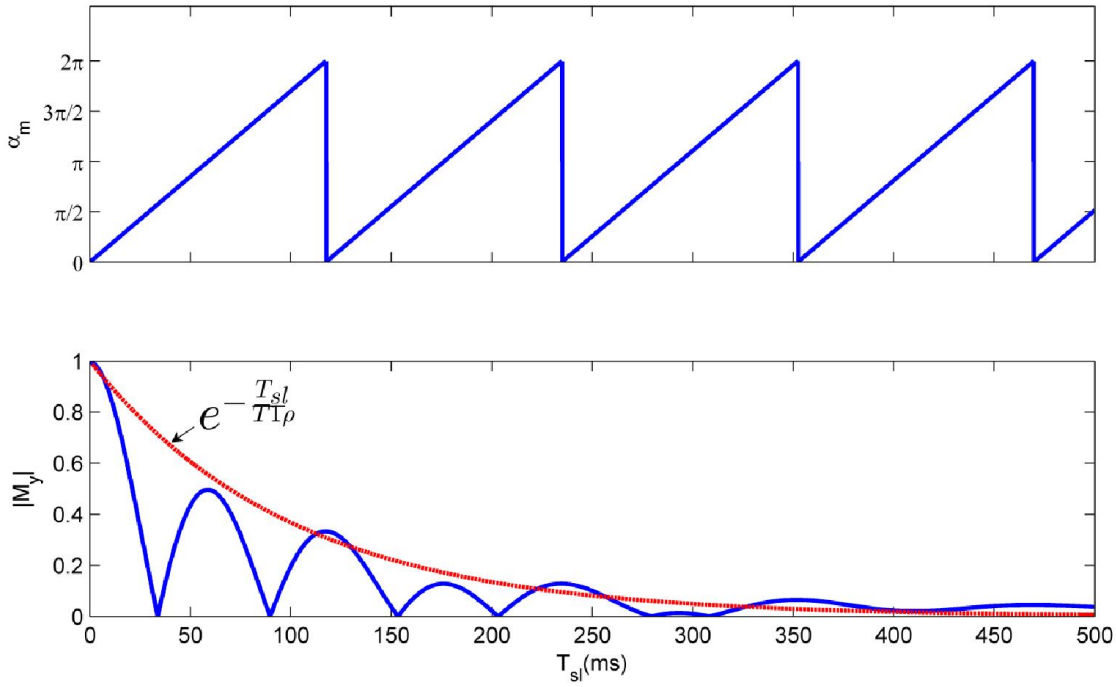

Figure 5-7: Effect of T_{sl} on magnetization. Increasing the T_{sl} leads to larger flip angle and tips the magnetization away from y-axis. The magnetization decays over time because of relaxations. Simulation parameters: ΔB_m = 200nT, $T1\rho$=100ms, $T2$=100ms, $T1$=1100ms, ω_{sl} = 100Hz, ω_{ac} = 100Hz.

5.3.4 Rotation effect

Only the orthogonal component of the microrobot's magnetic field to the spin-lock axis affects the signal. Since the magnetic field of the planar coil are not equal in all the direction, the effective amount of ΔB_m changes by rotating the microrobot. However, as explained in Section 4.3.3, the frequency of the applied electrical current is independent of microrobot's rotation. Therefore, the spin-lock method for communication is independent of the microrobot's rotation and displacement.

Figure 5-8 shows the simulated magnetic field and magnetization after the spin-lock period in the coronal plane for a microcoil placed in the axial plane. Figure 5-9 shows the simulated magnetic field and the magnetization when the coil is rotated to the coronal plane.

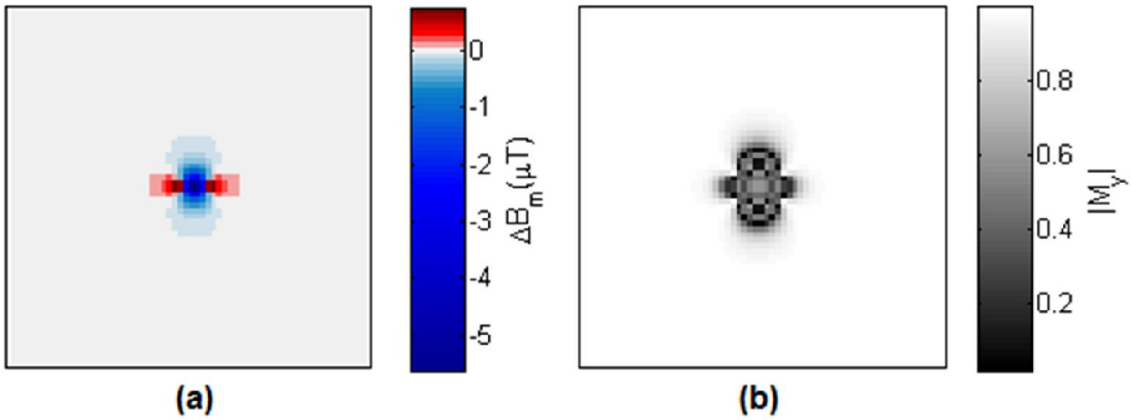

Figure 5-8: Coil in axial plane (a) Simulated magnetic field, of a microcoil with an outer diameter of 350μm by applying 70μA current with ω_{ac} = 100Hz. (b) Coronal image of magnetization at the end of spin-lock period. Simulation parameters: T_{sl} = 50ms, $T1\rho$=100ms, $T2$=100ms, $T1$=1100ms, ω_{sl} = 100Hz.

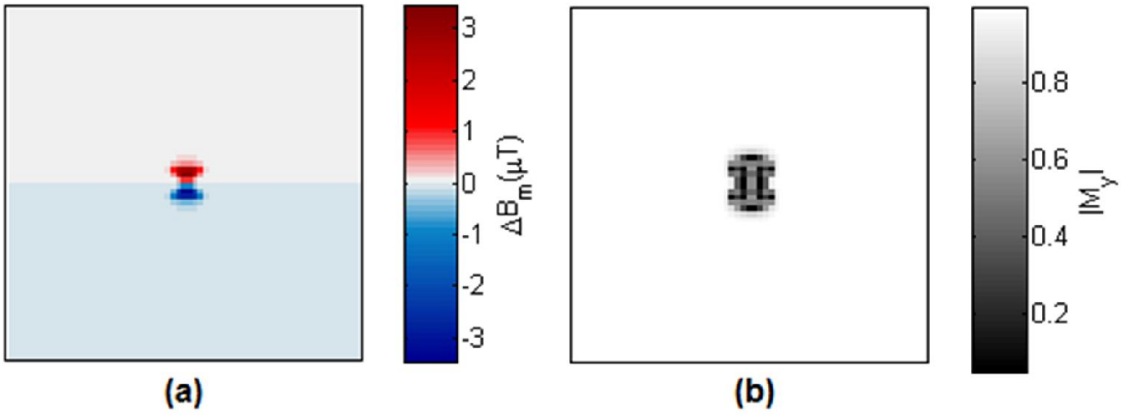

Figure 5-9: Rotating the coil onto coronal plane (a) Simulated magnetic field. (b) Axial image of magnetization at the end of spin-lock period. Simulation parameters: T_{sl} = 50ms, $T_{1\rho}$=100ms, $T2$=100ms, $T1$=1100ms, ω_{sl} = 100Hz.

5.4 Discussion

The resolution of our proposed method to distinguish between two frequencies depends on the resolution of sweeping spin-lock power and hence, on the scanner's RF module. The maximum detectable frequency with this method is restricted by maximum spin-lock power allowed due to the safety limits since long spin-lock pulses could potentially lead to tissue heating [118].

For clinical applications, the signal absorption rate (SAR) related to the RF energy deposition by the spin-lock pulse must meet safety regulations. SAR is normally defined as the absorbed RF power per unit mass per unit time during an imaging experiment, and it is measured in watts per kilogram (W/kg) [119]. For example, based on FDA regulation, the allowable maximum SAR for clinical imaging is 4 W/kg averaged over the whole body for any 15 min period, 3 W/kg averaged over the head for any 10 min period, or 8 W/kg in any gram of tissue in the extremities for any period of 5 min [119]. Since SAR is proportional to the square of the RF pulse flip angle and the square of static field strength B_0 [120], $T1\rho$ imaging is considered as SAR intensive because of the long spin-lock time.

Other factors that can affect the proposed method are inhomogeneity in B_1 field and the main static field. Presence of B_0 and B_1 field inhomogeneities cause poor alignment of the magnetization along the y-axis during the spin-lock module and the complicated magnetization evolution. B_0 shimming, B_1 calibration, and the improved design of the spin-lock RF pulse are helpful to lessen the inhomogeneity effect [119].

5.5 Conclusion

In this chapter, the feasibility of using the spin-lock and T1ρ imaging techniques to communicate with the microrobot at higher frequency ranges than the EPI technique was discussed. The results showed that sweeping the spin-lock power across resonance with the frequency of microrobot magnetic fields displays the resonant point between spin-lock field and the microrobot field and the frequency can be detected independent of microrobot's rotation and orientation. Our method can be expanded to communicate with several microrobots by selectively sweeping the spin-lock power across their frequency range.

CHAPTER 6 CONCLUSION AND RECOMMENDATIONS

This dissertation aimed to develop a new technique for communication with medical microrobots inside the human body. The miniaturization of the microrobot prevents the implementation of an adequate embedded communication system capable of transmitting sensory data. One of the major limitations is that power transmission cannot reach a level sufficient for proper communication.

In Chapter 3, we proposed exploiting the MRI system and its sensitivity to the susceptibility artifact as a communication mean with microrobots to overcome size and power constrains. An electrical current passing through the transmitting coil embedded in the microrobot generates a magnetic field that interferes with the homogeneous static magnetic field of the MRI (B_0) and appears in the MR images as a susceptibility artifact. The direction of the electrical current could be regulated based on a predetermined sensory threshold input, which leads to a change in the form of the magnetic field. We showed that the shape of the artifact in MR images is affected by the form of the magnetic field, and as a result, by the direction of the current in the transmitting coil. However, the shape of the artifact is also dependent on the orientation of the microrobots and thus, knowledge of the microrobot's orientation relative to its initial orientation is essential to interpret the images.

To overcome the above limitation, we proposed a new communication method using single-shot EPI-GRE MR images to detect the variation in the electrical current's frequency instead of its direction in Chapter 4. We showed that the frequency is independent of the rotation and the position of the microrobot. The minimum magnetic field detectable by our proposed method decreased to 350pT compared to 50nT in Chapter 3. This allows us to achieve a higher level of miniaturization where the power source, and consequently, the generated magnetic field, would be limited. Moreover, the ability to detect several frequencies makes it possible to use our binary communication method for more than one sensor on one microrobot, or even to communicate with several microrobots by associating each sensor or microrobot to two specific frequencies which differ from the others. In addition, this method could also be used to measure a parameter by mapping each value onto a specific frequency. However, the maximum detectable frequency by EPI technique is limited by the minimum TR.

To increase the range of frequency, in Chapter 5, we proposed a new communication method using a T1ρ imaging technique. We showed that the sweeping of the spin-lock power across resonance with the frequency of microrobot magnetic fields display the resonant point between the spin-lock field and the microrobot field. And the frequency can be detected independent of the microrobot's orientation and position. Our method can be expanded to communicate with several microrobots by selectively sweeping the spin-lock power across their frequency range. Compared with the EPI method, this technique can detect higher ranges of frequencies; however, its clinical use is restricted because of SAR safety regulations.

6.1 Future work

Our work opens several new research directions. In-vivo realization of the proposed technique necessitates further steps:

- Since only the magnetic fields parallel to B_0 affect the MR images, the amount of effective magnetic field varies by rotating the microrobot. As a result, the current must be strong enough to generate a magnetic field larger than the threshold in all directions. This larger power requirement limits the level of miniaturization. Hence, it is necessary to investigate different topologies for the transmitting coil to generate an equal magnetic field in all directions, making such a communication method completely independent of rotational motions.
- An integrated circuit should be designed and fabricated to be embedded on the microrobot to measure sensory data.
- The localization technique must be investigated for navigating and tracking purposes.

Successful realization of this microrobot could potentially be used in the following medical applications:

- **Catheter Steering**

Catheter steering through the arterial system is a major issue in several medical applications. A surgeon with a high level of endovascular skills needs to manipulate a catheter manually through a complex blood vessel network. Catheters must be placed and steered carefully to avoid major injuries such as the perforation of an artery. Traditionally, several shapeable guide wires and

catheters can slide inside each another to perform catheter steering. A physician can use a linear back and forth movement as well as rotating the catheter around its axis in order to steer it. This method of actuation might cause many complications such as exposing the patient to more radiation, longer procedure time, hematoma, and the puncture of vessels [121]. Some methods use x-ray fluoroscopy to guide the catheter through the arterial system. Fluoroscopy uses ionizing radiations that lead to radiation exposure to the patient and the medical specialist. This phenomenon may lead to serious health effects on each person who attends the procedure if there is overexposure [122]. The idea of using an upgraded Magnetic Resonance Imaging (MRI) system to facilitate the steering of a catheter has been proposed and investigated in many studies [122-125] Using a MRI system not only excludes the ionizing radiation exposure but also enhances the soft tissue contrast in the images [123]. Moreover, fluoroscopy can only describe the lumen of the vessels while MRI can visualize the morphology of the soft tissue surrounding the blood vessels [121, 124]

Different research propose the idea of placing wound coils at the distal end of a catheter to guide the catheter during intravascular procedures using MRI. A catheter with three orthogonal coils on its tip is proposed in [122]. The artifact of the current induced magnetic field of the coils can be detected in MR images. However, the radio frequencies used for imaging and the intermittent current passing through the coils induce ohmic heating of the catheter wiring which can burn the surrounding tissues. To solve this problem, the use of ferromagnetic spheres instead of the coils has been proposed [125]. In this case, one or two optimally distanced ferromagnetic spheres are attached at the distal tip of the catheter. However, due to the generated artifact, it is impossible to visualize the tissues within a few centimeters of the catheter tip in MR images.

The ferromagnetic bead can be replaced by our microrobot that is powered by a photovoltaic cell. When the light source is switched on, the photovoltaic cell powers the microrobot and the microrobot generates a magnetic field that can be detected in MR images. In addition, by switching off the light source, the microrobot will not generate any magnetic field. Therefore, it is possible to visualize the tissues in the absence of the artifact.

The ability to steer the microrobot by a magnetic gradient force, providing a suitable light source, and the penetration of light into the human body are the challenges that must be addressed for this application. Successful accomplishment of this project would lead to the ability to facilitate

real-time control of the catheter. This new approach can be used for drug delivery as well as making this process more precise and fast.

- **Detect Early Stage Tumor Based on its pH Variation**

According to the World Health Organization (WHO), the total number of cancer deaths is projected to rise by 45% between 2007 and 2030, which represents an increase from 7.9 million to 11.5 million deaths [126]. Therefore, it is necessary to develop new tools to more efficiently detect, propose new treatment, and follow up with people affected by cancer.

Our microrobot could potentially be used for the early detection of new cancerous cells located at a specific part of the body. Studies illustrate that when a tumor starts to grow, it changes some of its nearby micro-environmental variables such as pH level. The extracellular pH (pHe) of a tumor is usually lower than the one of normal cells [127, 128]. Hence, a pH level of less than a predetermined threshold would trigger the communication part of the microrobot, and the direction or the frequency of its electrical current will vary depending on the pH level.

Successful accomplishment of the proposed technique will result in:

- Reducing the risk of tumor metastases to other organs of the body by improving early detection
- More efficient treatment by providing more information about the environmental variables of the tumor,
- Reducing the risk of tumor reformation

BIBLIOGRAPHY

[1] B. J. Nelson, I. K. Kaliakatsos, and J. J. Abbott, "Microrobots for minimally invasive medicine," *Annu Rev Biomed Eng,* vol. 12, pp. 55-85, Aug 15 2010.

[2] K. E. Peyer, L. Zhang, and B. J. Nelson, "Bio-inspired magnetic swimming microrobots for biomedical applications," *Nanoscale,* vol. 5, pp. 1259-72, Feb 21 2013.

[3] W. Zhang, S. Guo, and K. Asaka, "Development of an underwater biomimetic microrobot with compact structure and flexible locomotion," *Microsystem Technologies,* vol. 13, pp. 883-890, 2007/05/01 2007.

[4] S. Hosseini, M. Mehrtash, and M. Khamesee, "Design, fabrication and control of a magnetic capsule-robot for the human esophagus," *Microsystem Technologies,* vol. 17, pp. 1145-1152, 2011/06/01 2011.

[5] K. B. Yesin, P. Exner, K. Vollmers, and B. Nelson, "Design and Control of In-Vivo Magnetic Microrobots," in *Medical Image Computing and Computer-Assisted Intervention – MICCAI 2005*. vol. 3749, J. Duncan and G. Gerig, Eds., ed: Springer Berlin Heidelberg, 2005, pp. 819-826.

[6] D. De Lanauze, O. Felfoul, J.-P. Turcot, M. Mohammadi, and S. Martel, "Three-dimensional remote aggregation and steering of magnetotactic bacteria microrobots for drug delivery applications," *The International Journal of Robotics Research,* vol. 33, pp. 359-374, March 1, 2014 2014.

[7] O. Felfoul and S. Martel, "Assessment of navigation control strategy for magnetotactic bacteria in microchannel: toward targeting solid tumors," *Biomedical microdevices,* vol. 15, pp. 1015-1024, 2013.

[8] S. Martel, C. C. Tremblay, S. Ngakeng, and G. Langlois, "Controlled manipulation and actuation of micro-objects with magnetotactic bacteria," *Applied Physics Letters,* vol. 89, p. 233904, 2006.

[9] I. S. Khalil, V. Magdanz, S. Sanchez, O. G. Schmidt, L. Abelmann, and S. Misra, "Magnetic control of potential microrobotic drug delivery systems: nanoparticles, magnetotactic bacteria and self-propelled microjets," in *Engineering in Medicine and Biology Society (EMBC), 2013 35th Annual International Conference of the IEEE*, 2013, pp. 5299-5302.

[10] B. Behkam and M. Sitti, "Bacterial flagella-based propulsion and on/off motion control of microscale objects," *Applied Physics Letters,* vol. 90, p. 023902, 2007.

[11] S. Martel, M. Mohammadi, O. Felfoul, Z. Lu, and P. Pouponneau, "Flagellated magnetotactic bacteria as controlled MRI-trackable propulsion and steering systems for medical nanorobots operating in the human microvasculature," *The International Journal of Robotics Research,* vol. 28, pp. 571-582, 2009.

[12] S. Kim, F. Qiu, S. Kim, A. Ghanbari, C. Moon, L. Zhang*, et al.*, "Fabrication and Characterization of Magnetic Microrobots for Three-Dimensional Cell Culture and Targeted Transportation," *Advanced Materials,* vol. 25, pp. 5863-5868, 2013.

[13] W. Jiang, D. Niu, H. Liu, C. Wang, T. Zhao, L. Yin*, et al.*, "Photoresponsive Soft-Robotic Platform: Biomimetic Fabrication and Remote Actuation," *Advanced Functional Materials,* vol. 24, pp. 7598-7604, 2014.

[14] K. D. Seo, B. K. Kwak, S. Sanchez, and D. S. Kim, "Microfluidic-Assisted Fabrication of Flexible and Location Traceable Organo-Motor," 2015.

[15] A. K. RamRakhyani, S. Mirabbasi, and C. Mu, "Design and Optimization of Resonance-Based Efficient Wireless Power Delivery Systems for Biomedical Implants," *Biomedical Circuits and Systems, IEEE Transactions on,* vol. 5, pp. 48-63, 2011.

[16] M. W. Baker and R. Sarpeshkar, "Feedback analysis and design of RF power links for low-power bionic systems," *Biomedical Circuits and Systems, IEEE Transactions on,* vol. 1, pp. 28-38, 2007.

[17] W. André and S. Martel, "Micro-photovoltaic cells designed for magnetotaxis-based controlled bacterial microrobots," *IEICE Electronics Express,* vol. 5, pp. 101-106, 2008.

[18] S. Martel and W. André, "Embedding a wireless transmitter within the space and power constraints of an electronic untethered microrobot," in *Circuits and Systems and TAISA Conference, 2009. NEWCAS-TAISA'09. Joint IEEE North-East Workshop on*, 2009, pp. 1-4.

[19] M. Ghovanloo and K. Najafi, "A wideband frequency-shift keying wireless link for inductively powered biomedical implants," *Circuits and Systems I: Regular Papers, IEEE Transactions on,* vol. 51, pp. 2374-2383, 2004.

[20] P. D. Bradley, "An ultra low power, high performance Medical Implant Communication System (MICS) transceiver for implantable devices," in *Biomedical Circuits and Systems Conference, 2006. BioCAS 2006. IEEE*, 2006, pp. 158-161.

[21] (2007). *MiniMed ParadigmÂ® real-time insulin pump and continuous glucose monitoring system,* . Available: http://www.minimed.com/professionals/realtime/index.html

[22] T. Buchegger, G. Oßberger, A. Reisenzahn, E. Hochmair, A. Stelzer, and A. Springer, "Ultra-wideband transceivers for cochlear implants," *EURASIP Journal on Applied Signal Processing,* vol. 2005, pp. 3069-3075, 2005.

[23] J. L. Bohorquez, A. P. Chandrakasan, and J. L. Dawson, "A 350 W CMOS MSK transmitter and 400 W OOK super-regenerative receiver for medical implant communications," *Solid-State Circuits, IEEE Journal of,* vol. 44, pp. 1248-1259, 2009.

[24] P. Soontornpipit, C. M. Furse, and Y. C. Chung, "Design of implantable microstrip antenna for communication with medical implants," *Microwave Theory and Techniques, IEEE Transactions on,* vol. 52, pp. 1944-1951, 2004.

[25] W. Jung, A. Rillig, R. Birkemeyer, T. Miljak, and U. Meyerfeldt, "Advances in remote monitoring of implantable pacemakers, cardioverter defibrillators and cardiac resynchronization therapy systems," *Journal of interventional cardiac electrophysiology,* vol. 23, pp. 73-85, 2008.

[26] D. Wessels, "Implantable pacemakers and defibrillators: device overview & EMI considerations," in *Electromagnetic Compatibility, 2002. EMC 2002. IEEE International Symposium on*, 2002, pp. 911-915.

[27] G. Iddan, G. Meron, A. Glukhovsky, and P. Swain, "Wireless capsule endoscopy," *Nature,* vol. 405, pp. 417-417, 2000.

[28] A. Moglia, A. Menciassi, M. O. Schurr, and P. Dario, "Wireless capsule endoscopy: from diagnostic devices to multipurpose robotic systems," *Biomedical microdevices,* vol. 9, pp. 235-243, 2007.

[29] K. Wang, G. Yan, P. Jiang, and D. Ye, "A wireless robotic endoscope for gastrointestine," *Robotics, IEEE Transactions on,* vol. 24, pp. 206-210, 2008.

[30] G. Yan, D. Ye, P. Zan, K. Wang, and G. Ma, "Micro-robot for endoscope based on wireless power transfer," in *Mechatronics and Automation, 2007. ICMA 2007. International Conference on*, 2007, pp. 3577-3581.

[31] R. F. Harrington, "Effect of antenna size on gain, bandwidth, and efficiency," *J. Res. Nat. Bur. Stand,* vol. 64, pp. 1-12, 1960.

[32] K. Y. Yazdandoost and R. Kohno, "Wireless communications for body implanted medical device," in *Microwave Conference, 2007. APMC 2007. Asia-Pacific*, 2007, pp. 1-4.

[33] P. Anacleto, P. Mendes, E. Gultepe, and D. Gracias, "Micro antennas for implantable medical devices," in *Bioengineering (ENBENG), 2013 IEEE 3rd Portuguese Meeting in*, 2013, pp. 1-4.

[34] W. s. Lu, W. y. Xu, J. Zhang, D. Liu, D. m. Wang, P. Jia*, et al.*, "Application study of medical robots in vascular intervention," *The International Journal of Medical Robotics and Computer Assisted Surgery,* vol. 7, pp. 361-366, 2011.

[35] E. Gultepe, J. S. Randhawa, S. Kadam, S. Yamanaka, F. M. Selaru, E. J. Shin*, et al.*, "Biopsy with Thermally-Responsive Untethered Microtools," *Advanced Materials,* vol. 25, pp. 514-519, 2013.

[36] Q. Shi, J. Wang, D. Chen, J. Chen, J. Li, and K. Bao, "In Vitro and In Vivo characterization of wireless and passive micro system enabling gastrointestinal pressure monitoring," *Biomedical microdevices,* vol. 16, pp. 859-868, 2014.

[37] E. G. Lim, Z. Wang, S. Nie, T. Tillo, K. L. Man, and N. Zhang, "Moveable wireless capsule endoscopy," in *SoC Design Conference (ISOCC), 2013 International*, 2013, pp. 270-273.

[38] O. Ergeneman, G. Chatzipirpiridis, S. Pané, G. A. Sotiriou, C. Bergeles, and B. J. Nelson, "Wireless microrobotic oxygen sensing for retinal hypoxia monitoring," in *Wireless Mobile Communication and Healthcare*, ed: Springer, 2012, pp. 75-79.

[39] A. M. Otto, M. Brischwein, A. Niendorf, T. Henning, E. Motrescu, and B. Wolf, "Microphysiological testing for chemosensitivity of living tumor cells with multiparametric microsensor chips," *Cancer detection and prevention,* vol. 27, pp. 291-296, 2003.

[40] L. Wang, N. Aydin, A. Astaras, M. Ahmadian, P. A. Hammond, T. Tang*, et al.*, "A sensor system on chip for wireless microsystems," in *Circuits and Systems, 2006. ISCAS 2006. Proceedings. 2006 IEEE International Symposium on*, 2006, pp. 4 pp.-858.

[41] G. Dogangil, O. Ergeneman, J. J. Abbott, S. Pané, H. Hall, S. Muntwyler*, et al.*, "Toward targeted retinal drug delivery with wireless magnetic microrobots," in *Intelligent Robots and Systems, 2008. IROS 2008. IEEE/RSJ International Conference on*, 2008, pp. 1921-1926.

[42] B. C. Becker, S. Yang, R. MacLachlan, and C. N. Riviere, "Towards vision-based control of a handheld micromanipulator for retinal cannulation in an eyeball phantom," in *Biomedical Robotics and Biomechatronics (BioRob), 2012 4th IEEE RAS & EMBS International Conference on*, 2012, pp. 44-49.

[43] B. C. Becker and C. N. Riviere, "Real-time retinal vessel mapping and localization for intraocular surgery," in *Robotics and Automation (ICRA), 2013 IEEE International Conference on*, 2013, pp. 5360-5365.

[44] M. Sendoh, K. Ishiyama, K. I. Arai, M. Jojo, F. Sato, and H. Matsuki, "Fabrication of magnetic micromachine for local hyperthermia," *Magnetics, IEEE Transactions on,* vol. 38, pp. 3359-3361, 2002.

[45] P. M. Devlin, *Brachytherapy: applications and techniques*: Lippincott Williams & Wilkins, 2007.

[46] S. Roundy, P. K. Wright, and K. S. Pister, "Micro-electrostatic vibration-to-electricity converters," in *ASME 2002 International Mechanical Engineering Congress and Exposition*, 2002, pp. 487-496.

[47] E. Cantatore and M. Ouwerkerk, "Energy scavenging and power management in networks of autonomous microsensors," *Microelectronics Journal,* vol. 37, pp. 1584-1590, 2006.

[48] T. Huesgen, P. Woias, and N. Kockmann, "Design and fabrication of MEMS thermoelectric generators with high temperature efficiency," *Sensors and Actuators A: Physical,* vol. 145, pp. 423-429, 2008.

[49] N. Kockmann, T. Huesgen, and P. Woias, "Microstructured in-plane thermoelectric generators with optimized heat path," in *Solid-State Sensors, Actuators and Microsystems Conference, 2007. TRANSDUCERS 2007. International*, 2007, pp. 133-136.

[50] V. Leonov, P. Fiorini, S. Sedky, T. Torfs, and C. Van Hoof, "Thermoelectric MEMS generators as a power supply for a body area network," in *Solid-State Sensors, Actuators and Microsystems, 2005. Digest of Technical Papers. TRANSDUCERS'05. The 13th International Conference on*, 2005, pp. 291-294.

[51] J. Varona, M. Tecpoyotl-Torres, A. A. Hamoui, J. Ecobedo-Alatorre, and J. Sanchez-Mondragon, "Polysilicon thermal microactuators for heat scavenging and power conversion," *Journal of Micro/Nanolithography, MEMS, and MOEMS,* vol. 8, pp. 023020-023020-8, 2009.

[52] J. Lueke and W. A. Moussa, "MEMS-based power generation techniques for implantable biosensing applications," *Sensors,* vol. 11, pp. 1433-1460, 2011.

[53] N. Mano, F. Mao, and A. Heller, "Characteristics of a miniature compartment-less glucose-O2 biofuel cell and its operation in a living plant," *Journal of the American Chemical Society,* vol. 125, pp. 6588-6594, 2003.

[54] M. Deterre, B. Boutaud, R. Dalmolin, S. Boisseau, J.-J. Chaillout, E. Lefeuvre*, et al.*, "Energy harvesting system for cardiac implant applications," in *Design, Test, Integration and Packaging of MEMS/MOEMS (DTIP), 2011 Symposium on*, 2011, pp. 387-391.

[55] R. A. Bullen, T. Arnot, J. Lakeman, and F. Walsh, "Biofuel cells and their development," *Biosensors and Bioelectronics,* vol. 21, pp. 2015-2045, 2006.

[56] S. Calabrese Barton, J. Gallaway, and P. Atanassov, "Enzymatic biofuel cells for implantable and microscale devices," *Chemical reviews,* vol. 104, pp. 4867-4886, 2004.

[57] R. R. Harrison, "Designing efficient inductive power links for implantable devices," in *Circuits and Systems, 2007. ISCAS 2007. IEEE International Symposium on*, 2007, pp. 2080-2083.

[58] Z. Hamici, R. Itti, and J. Champier, "A high-efficiency biotelemetry system for implanted electronic device," in *Engineering in Medicine and Biology Society, 1995., IEEE 17th Annual Conference*, 1995, pp. 1649-1650.

[59] G. Wang, W. Liu, M. Sivaprakasam, M. Zhou, J. D. Weiland, and M. S. Humayun, "A dual band wireless power and data telemetry for retinal prosthesis," in *Engineering in Medicine and Biology Society, 2006. EMBS'06. 28th Annual International Conference of the IEEE*, 2006, pp. 4392-4395.

[60] M. Catrysse, B. Hermans, and R. Puers, "An inductive power system with integrated bi-directional data-transmission," *Sensors and Actuators A: Physical,* vol. 115, pp. 221-229, 2004.

[61] A. Kumar, S. Mirabbasi, and M. Chiao, "Resonance-based wireless power delivery for implantable devices," in *Biomedical Circuits and Systems Conference, 2009. BioCAS 2009. IEEE*, 2009, pp. 25-28.

[62] T. Sterken, P. Fiorini, G. Altena, C. Van Hoof, and R. Puers, "Harvesting energy from vibrations by a micromachined electret generator," in *14th International conference on Solid-State Sensors, Actuators and Microsystems (Transducers 2007)*, 2007, pp. U68-U69.

[63] A. M. Paracha, P. Basset, D. Galayko, F. Marty, and T. Bourouina, "A silicon MEMS DC/DC converter for autonomous vibration-to-electrical-energy scavenger," *Electron Device Letters, IEEE,* vol. 30, pp. 481-483, 2009.

[64] B. C. Yen and J. H. Lang, "A variable-capacitance vibration-to-electric energy harvester," *Circuits and Systems I: Regular Papers, IEEE Transactions on,* vol. 53, pp. 288-295, 2006.

[65] F. Lu, H. Lee, and S. Lim, "Modeling and analysis of micro piezoelectric power generators for micro-electromechanical-systems applications," *Smart Materials and Structures,* vol. 13, p. 57, 2004.

[66] T. Ishisaka, H. Sato, Y. Akiyama, Y. Furukawa, and K. Morishima, "Bio-actuated power generator using heart muscle cells on a PDMS membrane," in *Solid-State Sensors,*

Actuators and Microsystems Conference, 2007. TRANSDUCERS 2007. International, 2007, pp. 903-906.

[67] P. X. Gao, J. Song, J. Liu, and Z. L. Wang, "Nanowire piezoelectric nanogenerators on plastic substrates as flexible power sources for nanodevices," *Advanced Materials,* vol. 19, pp. 67-72, 2007.

[68] S. Xu, Y. Qin, C. Xu, Y. Wei, R. Yang, and Z. L. Wang, "Self-powered nanowire devices," *Nature nanotechnology,* vol. 5, pp. 366-373, 2010.

[69] S. Fusco, M. S. Sakar, S. Kennedy, C. Peters, R. Bottani, F. Starsich*, et al.*, "An Integrated Microrobotic Platform for On-Demand, Targeted Therapeutic Interventions," *Advanced Materials,* vol. 26, pp. 952-957, 2014.

[70] G. Gillies, R. Ritter, W. Broaddus, M. Grady, M. Howard III, and R. McNeil, "Magnetic manipulation instrumentation for medical physics research," *Review of Scientific Instruments,* vol. 65, pp. 533-562, 1994.

[71] M. Grady, M. Howard III, J. Molloy, R. Ritter, E. Quate, and G. Gillies, "Nonlinear magnetic stereotaxis: Three-dimensional, invivo remote magnetic manipulation of a small object in canine brain," *Medical Physics,* vol. 17, pp. 405-415, 1990.

[72] K. B. Yesin, K. Vollmers, and B. J. Nelson, "Modeling and control of untethered biomicrorobots in a fluidic environment using electromagnetic fields," *The International Journal of Robotics Research,* vol. 25, pp. 527-536, 2006.

[73] D. C. Meeker, E. H. Maslen, R. C. Ritter, and F. M. Creighton, "Optimal realization of arbitrary forces in a magnetic stereotaxis system," *Magnetics, IEEE Transactions on,* vol. 32, pp. 320-328, 1996.

[74] E. B. Steager, M. S. Sakar, C. Magee, M. Kennedy, A. Cowley, and V. Kumar, "Automated biomanipulation of single cells using magnetic microrobots," *The International Journal of Robotics Research,* vol. 32, pp. 346-359, 2013.

[75] J.-B. Mathieu, G. Beaudoin, and S. Martel, "Method of propulsion of a ferromagnetic core in the cardiovascular system through magnetic gradients generated by an MRI system," *Biomedical Engineering, IEEE Transactions on,* vol. 53, pp. 292-299, 2006.

[76] S. Martel, J.-B. Mathieu, O. Felfoul, A. Chanu, E. Aboussouan, S. Tamaz*, et al.*, "Automatic navigation of an untethered device in the artery of a living animal using a conventional clinical magnetic resonance imaging system," *Applied Physics Letters,* vol. 90, p. 114105, 2007.

[77] K. B. Yesin, P. Exner, K. Vollmers, and B. J. Nelson, "Design and control of in-vivo magnetic microrobots," in *Medical Image Computing and Computer-Assisted Intervention–MICCAI 2005*, ed: Springer, 2005, pp. 819-826.

[78] Z. Nagy, O. Ergeneman, J. J. Abbott, M. Hutter, A. M. Hirt, and B. J. Nelson, "Modeling assembled-MEMS microrobots for wireless magnetic control," in *Robotics and Automation, 2008. ICRA 2008. IEEE International Conference on*, 2008, pp. 874-879.

[79] V. S. Kalambur, B. Han, B. E. Hammer, T. W. Shield, and J. C. Bischof, "In vitro characterization of movement, heating and visualization of magnetic nanoparticles for biomedical applications," *Nanotechnology,* vol. 16, p. 1221, 2005.

[80] S. Martel and M. Mohammadi, "Using a swarm of self-propelled natural microrobots in the form of flagellated bacteria to perform complex micro-assembly tasks," in *Robotics and Automation (ICRA), 2010 IEEE International Conference on*, 2010, pp. 500-505.

[81] L. Zhang, J. J. Abbott, L. Dong, K. E. Peyer, B. E. Kratochvil, H. Zhang*, et al.*, "Characterizing the swimming properties of artificial bacterial flagella," *Nano Letters,* vol. 9, pp. 3663-3667, 2009.

[82] G. Kósa, M. Shoham, and M. Zaaroor, "Propulsion method for swimming microrobots," *Robotics, IEEE Transactions on,* vol. 23, pp. 137-150, 2007.

[83] G. Kósa, P. Jakab, F. Jólesz, and N. Hata, "Swimming capsule endoscope using static and RF magnetic field of MRI for propulsion," in *Robotics and Automation, 2008. ICRA 2008. IEEE International Conference on*, 2008, pp. 2922-2927.

[84] Epoxy-Technology-Inc. (17 June). *EPO-TEK 301-2 Datasheet*. Available: www.epotek.com/site/administrator/.../com.../301-2%20Rev%20XII.pdf

[85] A. Beyzavi and N.-T. Nguyen, "Modeling and optimization of planar microcoils," *Journal of Micromechanics and Microengineering,* vol. 18, p. 095018, 2008.

[86] N. Olamaei, F. Cheriet, G. Beaudoin, and S. Martel, "MRI visualization of a single 15 microm navigable imaging agent and future microrobot," *Conf Proc IEEE Eng Med Biol Soc,* vol. 2010, pp. 4355-8, 2010.

[87] J. Bodurka and P. A. Bandettini, "Toward direct mapping of neuronal activity: MRI detection of ultraweak, transient magnetic field changes," *Magnetic Resonance in Medicine,* vol. 47, pp. 1052-1058, 2002.

[88] J. Bodurka, A. Jesmanowicz, J. Hyde, H. Xu, L. Estkowski, and S.-J. Li, "Current-induced magnetic resonance phase imaging," *Journal of Magnetic Resonance,* vol. 137, pp. 265-271, 1999.

[89] S. Balac and G. Caloz, "Mathematical Modeling and Numerical Simulation of Magnetic Susceptibility Artifacts in Magnetic Resonance IMAGING*," *Computer methods in biomechanics and biomedical engineering,* vol. 3, pp. 335-349, 2000.

[90] T. Wortmann, C. Dahmen, C. Geldmann, and S. Fatikow, "Recognition and tracking of magnetic nanobots using MRI," in *Optomechatronic Technologies (ISOT), 2010 International Symposium on*, 2010, pp. 1-6.

[91] T. Wortmann, C. Dahmen, and S. Fatikow, "Study of MRI susceptibility artifacts for nanomedical applications," *Journal of Nanotechnology in Engineering and Medicine,* vol. 1, p. 041002, 2010.

[92] E. M. Haacke, R. W. Brown, M. R. Thompson, and R. Venkatesan, *Magnetic Resonance Imaging: Physical Principles and Sequence Design*: Wiley, 1999.

[93] P. Mansfield, "Multi-planar image formation using NMR spin echoes," *Journal of Physics C: Solid State Physics,* vol. 10, p. L55, 1977.

[94] M. Poustchi-Amin, S. A. Mirowitz, J. J. Brown, R. C. McKinstry, and T. Li, "Principles and applications of echo-planar imaging: a review for the general radiologist," *Radiographics,* vol. 21, pp. 767-79, May-Jun 2001.

[95] H. Benoit-Cattin, G. Collewet, B. Belaroussi, H. Saint-Jalmes, and C. Odet, "The SIMRI project: a versatile and interactive MRI simulator," *Journal of Magnetic Resonance,* vol. 173, pp. 97-115, 2005.

[96] F. Bloch, "Nuclear induction," *Physical review,* vol. 70, p. 460, 1946.

[97] Z.-P. Liang and P. C. Lauterbur, *Principles of magnetic resonance imaging:A Signal Processing Perspective*: SPIE Optical Engineering Press, 2000.

[98] G. B. Chavhan, P. S. Babyn, B. Thomas, M. M. Shroff, and E. M. Haacke, "Principles, Techniques, and Applications of T2*-based MR Imaging and Its Special Applications 1," *Radiographics,* vol. 29, pp. 1433-1449, 2009.

[99] L. Czervionke, D. Daniels, F. Wehrli, L. Mark, L. Hendrix, J. Strandt*, et al.*, "Magnetic susceptibility artifacts in gradient-recalled echo MR imaging," *American journal of neuroradiology,* vol. 9, pp. 1149-1155, 1988.

[100] J. Graessner, "Bandwidth in MRI," *MAGNETOM Flash,* vol. 2, pp. 3-8, 2013.

[101] A. D. Elster. (2014, 9 June). *Receiver Bandwidth*. Available: http://mri-q.com/receiver-bandwidth.html

[102] T. Schrack. (1996) Echo Planar Imaging. *Signa application guide*.

[103] F. M. Vogt, M. E. Ladd, P. Hunold, S. Mateiescu, F. X. Hebrank, A. Zhang*, et al.*, "Increased Time Rate of Change of Gradient Fields: Effect on Peripheral Nerve Stimulation at Clinical MR Imaging 1," *Radiology,* vol. 233, pp. 548-554, 2004.

[104] J. Reilly, "Peripheral nerve stimulation by induced electric currents: exposure to time-varying magnetic fields," *Medical and Biological Engineering and Computing,* vol. 27, pp. 101-110, 1989.

[105] R. Bowtell and R. Bowley, "Analytic calculations of the E-fields induced by time-varying magnetic fields generated by cylindrical gradient coils," *Magnetic Resonance in Medicine,* vol. 44, pp. 782-790, 2000.

[106] M. Blaimer, F. Breuer, M. Mueller, R. M. Heidemann, M. A. Griswold, and P. M. Jakob, "SMASH, SENSE, PILS, GRAPPA: how to choose the optimal method," *Topics in Magnetic Resonance Imaging,* vol. 15, pp. 223-236, 2004.

[107] D. K. Sodickson and W. J. Manning, "Simultaneous acquisition of spatial harmonics (SMASH): fast imaging with radiofrequency coil arrays," *Magnetic Resonance in Medicine,* vol. 38, pp. 591-603, 1997.

[108] D. K. Sodickson, "Tailored SMASH image reconstructions for robust in vivo parallel MR imaging," *Magnetic Resonance in Medicine,* vol. 44, pp. 243-251, 2000.

[109] M. A. Griswold, P. M. Jakob, M. Nittka, J. W. Goldfarb, and A. Haase, "Partially parallel imaging with localized sensitivities (PILS)," *Magnetic Resonance in Medicine,* vol. 44, pp. 602-609, 2000.

[110] M. A. Griswold, P. M. Jakob, R. M. Heidemann, M. Nittka, V. Jellus, J. Wang*, et al.*, "Generalized autocalibrating partially parallel acquisitions (GRAPPA)," *Magnetic Resonance in Medicine,* vol. 47, pp. 1202-1210, 2002.

[111] W. E. Kyriakos, L. P. Panych, D. F. Kacher, C. F. Westin, S. M. Bao, R. V. Mulkern*, et al.*, "Sensitivity profiles from an array of coils for encoding and reconstruction in parallel (SPACE RIP)," *Magnetic Resonance in Medicine,* vol. 44, pp. 301-308, 2000.

[112] K. P. Pruessmann, M. Weiger, M. B. Scheidegger, and P. Boesiger, "SENSE: sensitivity encoding for fast MRI," *Magnetic Resonance in Medicine,* vol. 42, pp. 952-962, 1999.

[113] E. M. Haacke, R. W. Brown, M. R. Thompson, and R. Venkatesan, "Echo Planar Imaging(EPI)," in *Magnetic Resonance Imaging: Physical Principles and Sequence Design*, ed: Wiley, 1999, pp. 524-530.

[114] A. Bozzao, R. Floris, M. Pocek, F. Fasoli, F. Garaci, and G. Simonetti, "[Non-invasive assessment of epiaortic vessels. Comparison of magnetic resonance angiography with gadolinium, spiral computerized tomography angiography, and digital angiography]," *La Radiologia medica,* vol. 101, pp. 48-53, 2000.

[115] D. G. Nishimura, *Principles of magnetic resonance imaging*: Stanford University, 1996.

[116] S. Nagahara and T. Kobayashi, "Bloch simulations towards direct detection of oscillating magnetic fields using MRI with spin-lock sequence," in *Engineering in Medicine and Biology Society (EMBC), 2013 35th Annual International Conference of the IEEE*, 2013, pp. 1061-1064.

[117] K. Murase and N. Tanki, "Numerical solutions to the time-dependent Bloch equations revisited," *Magnetic resonance imaging,* vol. 29, pp. 126-131, 2011.

[118] M. I. Kettunen, A. Sierra, M. J. Narvainen, P. K. Valonen, S. Yla-Herttuala, R. A. Kauppinen*, et al.*, "Low Spin-Lock Field T1 Relaxation in the Rotating Frame as a Sensitive MR Imaging Marker for Gene Therapy Treatment Response in Rat Glioma 1," *Radiology,* vol. 243, pp. 796-803, 2007.

[119] Y. Jing and J. W. Yi-Xiang, "T1rho MR Imaging," in *Medical Imaging*, ed: CRC Press, 2013, pp. 565-592.

[120] C. M. Collins, S. Li, and M. B. Smith, "SAR and B1 field distributions in a heterogeneous human head model within a birdcage coil," *Magnetic Resonance in Medicine,* vol. 40, pp. 847-856, 1998.

[121] M. Bock and F. K. Wacker, "MR-guided intravascular interventions: Techniques and applications," *Journal of Magnetic Resonance Imaging,* vol. 27, pp. 326-338, 2008.

[122] V. Lalande, F. P. Gosselin, and S. Martel, "Catheter steering using a Magnetic Resonance Imaging system," in *Conference proceedings:... Annual International Conference of the IEEE Engineering in Medicine and Biology Society. IEEE Engineering in Medicine and Biology Society. Annual Conference*, 2009, pp. 1874-1877.

[123] S. Nazarian, A. Kolandaivelu, M. M. Zviman, G. R. Meininger, R. Kato, R. C. Susil*, et al.*, "Feasibility of Real-Time Magnetic Resonance Imaging for Catheter Guidance in Electrophysiology Studies," *Circulation,* vol. 118, pp. 223-229, July 15, 2008 2008.

[124] R. Razavi, D. L. Hill, S. F. Keevil, M. E. Miquel, V. Muthurangu, S. Hegde*, et al.*, "Cardiac catheterisation guided by MRI in children and adults with congenital heart disease," *The Lancet,* vol. 362, pp. 1877-1882, 2003.

[125] F. P. Gosselin, V. Lalande, and S. Martel, "Characterization of the deflections of a catheter steered using a magnetic resonance imaging system," *Medical Physics,* vol. 38, pp. 4994-5002, 2011.

[126] World-Health-Organization. (2008, 26 June). *Are the number of cancer cases increasing or decreasing in the world?* Available: http://www.who.int/features/qa/15/en/

[127] E. S. Lee, Z. Gao, and Y. H. Bae, "Recent progress in tumor pH targeting nanotechnology," *Journal of Controlled Release,* vol. 132, pp. 164-170, 2008.

[128] X. Zhang, Y. Lin, and R. J. Gillies, "Tumor pH and its measurement," *Journal of Nuclear Medicine,* vol. 51, pp. 1167-1170, 2010.